VOLUME 39, NUMBER 1, MARCH 2016

HADRONIC JOURNAL

HADRONIC JOURNAL Volume 39, Number 1, March 2016

Founded in 1978 by Prof. R. M. Santilli at Harvard University. Some of the past Editors include Professors S. L. Adler, A. 0. Barut, L. C. Biedenharn, N. N. Bogoliubov, M. Froissart, J.Lohmus, S. Okubo, Nobel Laureate Ilya Prigogine, M. L. Tomber, J. P.Vigier, J. Wess, Nobel Laureate Chen Ning Yang.

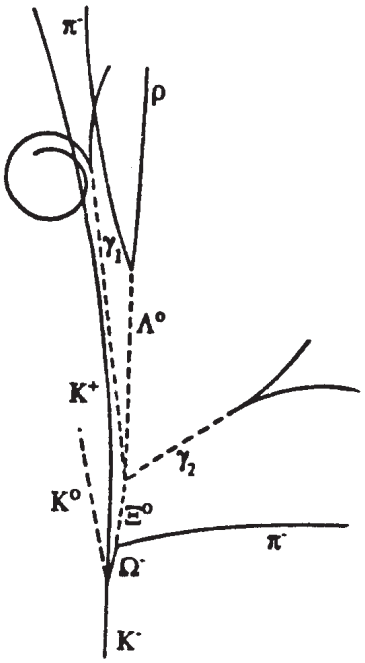

EDITORIAL BOARD

A.O.ANIMALU
A. K. ARINGAZIN
A. A. BHALEKAR
S. J. DHOBLE
J. DUNNING-DAVIES
T. L. GILL
L. P. HORWITZ
S. L. KALLA
S. I. KRUGLOV
M. NISHIOKA
R. F. O'CONNELL
Z. OZIEWICZ
E. RECAMI
M. SALEEM
B. G. SIDHARTH
S. SILVESTROV
H. M. SRIVASTAVA
E. TRELL
R.I. TSONCHEV
QI-REN ZHANG
C.A.WOLF
YI-ZHONG ZHUO

FOUNDER and
Editor In Chief
R. M. SANTILLI

H/P HADRONIC PRESS, INC.

HADRONIC JOURNAL

VOLUME 39, NUMBER 1, MARCH 2016

HIGGS-HIGGS INTERACTION. THE ONE-LOOP AMPLITUDE IN THE STANDARD MODEL, 1

Valeriy V. Dvoeglazov
Universidad de Zacatecas
A.P. 636, Suc. 3 Cruces
Zacatecas 98068 Zac. México

GEODISIC CURVATURES AND NATURAL LIFTS OF SPHERICAL INDICATORS OF TIMELIKE MANNHEIM PAIR CURVES, 41

Süleyman Şenyurt
Faculty of Arts and Sciences
Department of Mathematics, Ordu University
52200, Ordu, Turkey

DO HEAVY GAUGE BOSONS EXIST?, 67

Kenneth Dalton
General Delivery
Bang Saphan Yai 77140
Prachuap Kiri Khan
Thailand

A STUDY OF THE FUNDAMENTAL ORIGIN OF THE DIMENSION OF THE BOHR RADIUS OF THE HYDROGEN ATOM AS DETERMINED BY THE QUANTIZED DYNAMIC ELETRIC FIELD SURROUNDING A VORTEX MODEL OF THE ELECTRON, 71

Ernst L. Wall
Odyssey Systems
19 Crosby Dr.
Bedford, MA 01730 USA

HIGGS-HIGGS INTERACTION. THE ONE-LOOP AMPLITUDE IN THE STANDARD MODEL*

Valeriy V. Dvoeglazov
Universidad de Zacatecas
A.P. 636, Suc. 3 Cruces
Zacatecas 98068 Zac. México
valeri@fisica.uaz.edu.mx

Received October 20, 2015

Abstract

The amplitude of Higgs-Higgs interaction is calculated in the Standard Model in the framework of the Sirlin's renormalization scheme in the unitary gauge. The one-loop corrections for λ, the constant of 4χ interaction are compared with the previous results of L. Durand *et al.* obtained on using the technique of the equivalence theorem, and in the different gauges.

*The talk presented at the *Meeting of the DPF of the APS, May 24-28, 2002, The College W&M, Williamsburg, VA, USA*, May 26, 2002. Originally, it was on the website http://www.dpf2002.org/abstract_display.cfm?abstractid=26, which was promised to be permanently active.

Copyright © 2016 by Hadronic Press, Inc., Palm Harbor, FL 34684, USA

1 Introduction.

The Higgs sector of the electroweak theory attracts much attention because of its connection with the cornerstones of the theory. The search for Higgs scalars is included in most of the experimental programs of the newcoming and acting accelerators [1]. The Higgs particles are suggested to be found in the decays of different particles (Z^0 bosons, heavy quarkoniums etc.) as well as in photon-photon interactions and gluon-gluon fusion. In connection with that, let us mention non-so-long-ago attempts to explain anomalous events seen at SpS as the manifestation of the bound state of two Higgs bosons, i. e. of Higgsonium [2]-[4] or that of the bound state of vector boson [5] in accordance with the Veltman paper, Ref. [6]. Nowadays, even after clarifying the experimental situation with these anomalous events, the interest in Higgsonium has still the rights for existence at least from the viewpoint of preparedness to new unexpected news from the experiment. The previous investigations of the problem of existence of two-Higgs bound states were based on the Born approximation of their interaction amplitude [2]-[4]. In the present paper we present the results of our calculation of the amplitude of Higgs-Higgs interaction up to the fourth order in the framework of the Standard Model (SM) of Weinberg, Salam and Glashow with one Higgs doublet. This problem is also of present interest since there is some relations with the idea that gauge vector bosons could originate from a strong interacting scalar sector of the electroweak theory [7]. The amplitude obtained in this paper could also be useful for the consideration of the problem of the unitarity limit (e. g., [8]). Moreover, information on the behaviour of the Higgs coupling constants at mass scale M would be also of interest.

These are the reasons why we start a more complete study of the problem of Higgs-Higgs interaction. To reduce the volume of the article we shall use the standard notation used in [9], dimensional regularization and the renormalization scheme on the mass shell, which is analogous to that suggested in [9, 10]. We also choose the unitary gauge ($\xi \to \infty$, to avoid ghosts) and the parameters recommended by the Trieste conference [11], namely $(e_0, M_{W_0}, M_{Z_0}, M_{H_0}, m_{f_0})$.

The Higgs sector of the Lagrangian of the SM with one Higgs field has

the following form, e. g. [12]:[1]

$$\mathcal{L} = -\frac{1}{2}(\partial_\mu \chi)^2 - \frac{1}{2}M_\chi^2 \chi^2 - \frac{e}{2M_W(1-R)^{1/2}} \sum_f m_f \bar{f} f \chi -$$
$$- \frac{eM_W}{(1-R)^{1/2}} W_\mu^+ W_\mu^- \chi - \frac{eM_Z}{2R^{1/2}(1-R)^{1/2}} Z_\mu^2 \chi - \frac{e^2}{4(1-R)} W_\mu^+ W_\mu^- \chi^2 -$$
$$- \frac{e^2}{8R(1-R)} Z_\mu^2 \chi^2 - \frac{eM_\chi^2}{4M_W(1-R)^{1/2}} \chi^3 - \frac{e^2 M_\chi^2}{32 M_W^2 (1-R)} \chi^4 , \qquad (1.1)$$

where e is the electron charge, M_χ is the Higgs mass, M_W and M_Z are the masses of the vector bosons, m_f are the fermion masses, $R = M_W^2/M_Z^2$.

The paper is organized as follows. In Section 2 we present the expressions for the self-energy and vertex parts (see also calculations in details in [13]). The results of the calculation of the total Higgs-Higgs amplitude will be presented in Section 3. The Appendix contains the definitions of some integrals met in calculations. Their connections with the integrals calculated in [14, 15] is given.

[1] It is possible to add the pseudoscalar fermionic interaction, $\sim (1 + b_i \gamma_5)$.

Table I. Coupling constants in the case of the Standard Model.

f^W	$-\frac{1}{2\sqrt{2}}g$	f^{WWZA}	$ig^2\sqrt{R(1-R)}$
f^Z	$-\frac{1}{4}\frac{gM_Z}{M_W}$	$f^{W\chi}$	$-igM_W$
f^A	eQ_i	$f^{Z\chi}$	$-i\frac{gM_Z^2}{M_W}$
f^{WWZ}	$-\frac{gM_W}{M_Z}$	$f^{2W2\chi}$	$-i\frac{g^2}{2}$
f^{WWA}	e	$f^{2Z2\chi}$	$-i\frac{g^2M_Z^2}{2M_W^2}$
f^{2W2Z}	$-i\frac{g^2M_W^2}{M_Z^2}$	f^{χ}	$-i\frac{gm_i}{2M_W}$
f^{4W}	ig^2	$f^{3\chi}$	$-i\frac{3gM_\chi^2}{2M_W}$
f^{2W2A}	$-ie^2$	$f^{4\chi}$	$-i\frac{3g^2M_\chi^2}{4M_W^2}$

The Kobayashi-Maskawa K_{ij} matrix, $g = e/\sin\theta_W$ are used in the full Lagrangian of the SM, $2P = -\frac{1}{\epsilon}+\gamma+ln(M_W^2/4\pi\mu^2)$ are used in the dimensional regularization, γ is the Euler constant.

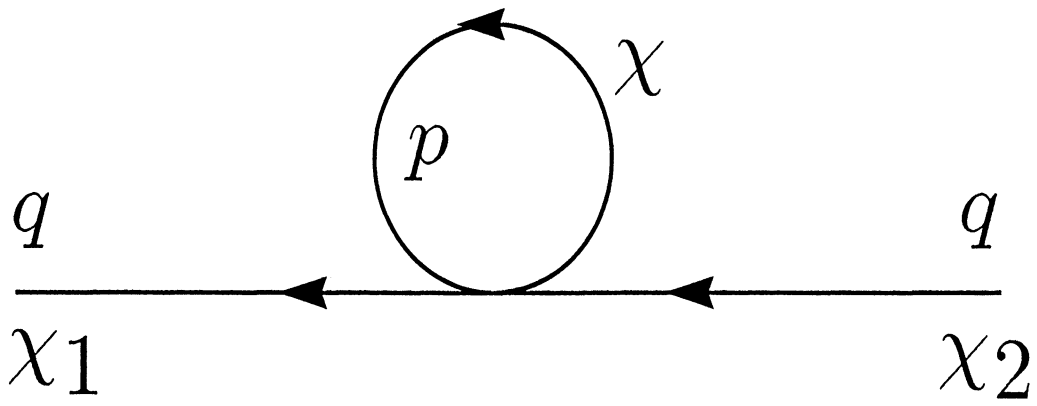

Figure 1:

2 Self-energy, vertex and box diagrams for the scalar boson.

2.1 Self-energy diagrams.

Here they are:

$$\Pi = \frac{if^{4\chi}}{16\pi^2} M_\chi^2 \left[2P - 1 + \log \frac{M_\chi^2}{M_W^2} \right]. \tag{2.2}$$

$$\Pi = \frac{if^{2V2\chi}}{16\pi^2} M_V^2 \left[6P - 1 + 3\log \frac{M_V^2}{M_W^2} \right]. \tag{2.3}$$

$$\Pi(q^2) = \frac{if_1^{3\chi} f_2^{3\chi}}{16\pi^2} \left[-2P - I_0(q^2, M_\chi^2, M_{\chi'}^2) \right]. \tag{2.4}$$

$$\Pi(q^2) = \frac{if_1^\chi f_2^\chi}{4\pi^2} \left\{ \left[(1 - b_1 b_2) \left(q^2 + 2m_1^2 + 2m_2^2 \right) + (1 + b_1 b_2) 2m_1 m_2 \right] P + \right.$$
$$+ \left. \left[\frac{1}{2}(1 - b_1 b_2) \left(q^2 + m_1^2 + m_2^2 \right) + (1 + b_1 b_2) m_1 m_2 \right] I_0(q^2, m_1^2, m_2^2) + \right. \tag{2.5}$$

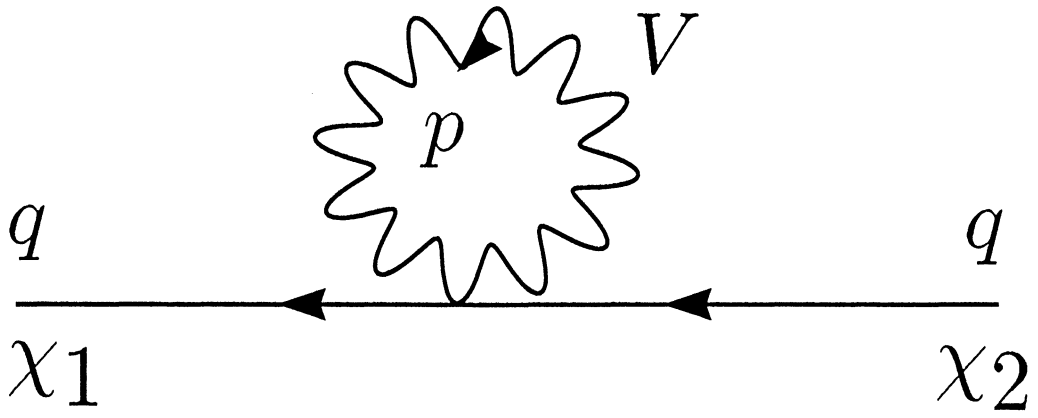

Figure 2:

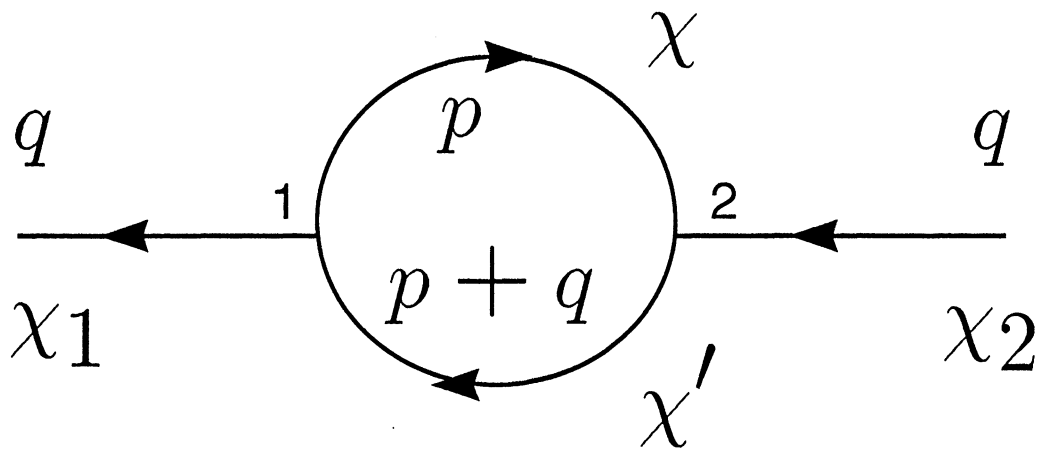

Figure 3:

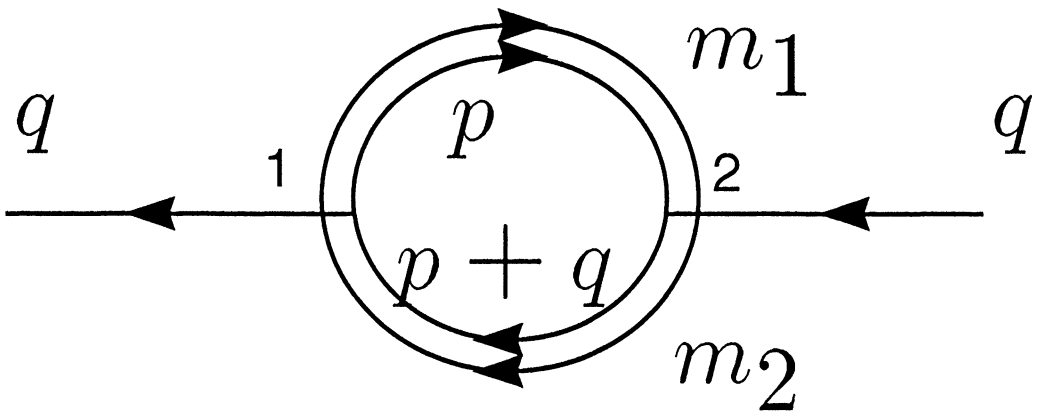

Figure 4:

$$+ \quad \frac{1}{2}(1-b_1b_2)\left(m_1^2\log\frac{m_1^2}{M_W^2}+m_2^2\log\frac{m_2^2}{M_W^2}+\frac{q^2}{2}\right)+\frac{1}{2}(1+b_1b_2)m_1m_2\Bigg\}.$$

$$\Pi(q^2)=\frac{if_1^{V\chi}f_2^{V\chi}}{16\pi^2}\left\{\left[-\frac{q^4}{2M_V^4}-3\frac{q^2}{M_V^2}-6\right]P- \tag{2.6}$$

$$- \quad \left(\frac{q^4}{4M_V^4}+\frac{q^2}{M_V^2}+3\right)I_0(q^2,M_V^2,M_V^2)-\frac{q^2}{2M_V^2}\log\frac{M_V^2}{M_W^2}+\frac{q^2}{2M_V^2}-2\Bigg\}.$$

In the framework of the SM with one Higgs doublet only we obtain

$$\Pi^\chi(q^2)=\frac{ig^2}{16\pi^2}M_\chi^2\left\{\left[-\frac{3}{4}\frac{q^4}{M_W^2M_\chi^2}-3\frac{q^2}{M_\chi^2}-\frac{3}{2R}\frac{q^2}{M_\chi^2}+\frac{q^2}{M_W^2M_\chi^2}Tr\,m_i^2-\right.\right.$$

$$- \quad 3r_W-9r_W^{-1}-\frac{9}{2R}r_Z^{-1}+\frac{6}{M_W^2M_\chi^2}Tr\,m_i^4\Bigg]P+tadpoles+\frac{3q^4}{4M_W^2M_\chi^2}+$$

$$+ \quad \left(\frac{5}{2}+\frac{5}{4R}\right)\frac{q^2}{M_\chi^2}+\frac{21}{8}r_W+\frac{9}{2}r_W^{-1}+\frac{9}{4R}r_Z^{-1}-\frac{3}{2}r_W\log r_W+\left(\frac{q^4}{8M_W^4}+\right.$$

$$+ \quad \left.\left.\frac{3}{4R}\frac{q^2}{M_W^2}+\frac{9}{4R^2}\right)r_W^{-1}\log R-\frac{3q^2}{4M_W^2M_\chi^2}Tr\,m_i^2+\right.$$

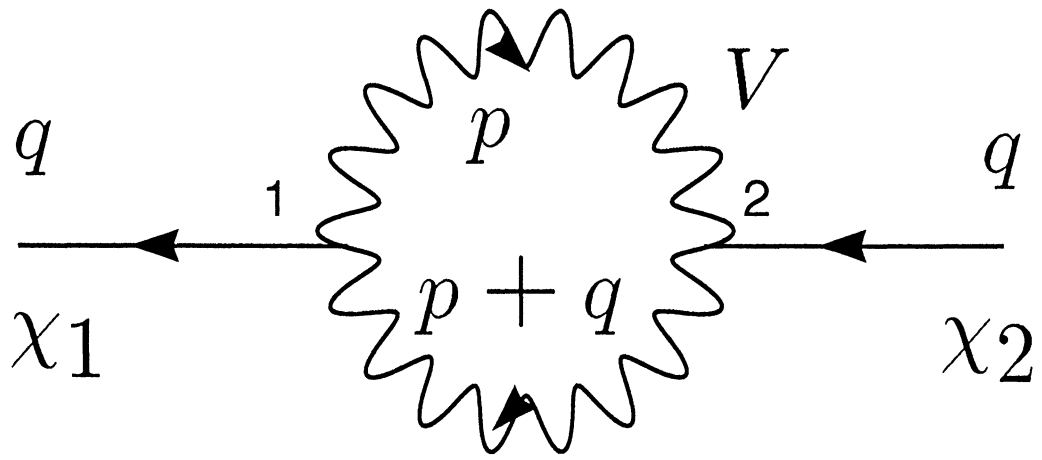

Figure 5:

$$
\begin{aligned}
&+ \quad \frac{q^2}{2M_W^2 M_\chi^2} Tr\, m_i^2 \log \frac{m_i^2}{M_W^2} - \frac{7}{2M_W^2 M_\chi^2} Tr\, m_i^4 + \frac{3}{M_W^2 M_\chi^2} Tr\, m_i^4 \log \frac{m_i^2}{M_W^2} - \\
&- \quad \left(\frac{q^2}{8M_W^2} + \frac{1}{2} + \frac{3M_W^2}{2q^2} \right) \frac{1}{M_\chi^2} L(q^2, M_W^2, M_W^2) - \\
&- \quad \left(\frac{q^2}{16M_Z^2} + \frac{1}{4} + \frac{3M_Z^2}{4q^2} \right) \frac{1}{R} \frac{1}{M_\chi^2} L(q^2, M_Z^2, M_Z^2) - \\
&- \quad \frac{9}{16} r_W \frac{1}{q^2} L(q^2, M_\chi^2, M_\chi^2) - \frac{1}{4M_W^2 M_\chi^2} Tr\, m_i^2 L(q^2, m_i^2, m_i^2) + \\
&+ \quad \frac{1}{M_W^2 M_\chi^2} \frac{1}{q^2} Tr\, m_i^4 L(q^2, m_i^2, m_i^2) \Bigg\} .
\end{aligned}
\tag{2.7}
$$

The corresponding counterterms are

$$
\begin{aligned}
\frac{\delta M_\chi^2}{M_\chi^2} = Z_{M_\chi} - Z_\chi = \frac{ig^2}{16\pi^2} \Bigg\{ \Bigg[& 3 + \frac{3}{2R} - \frac{15}{4} r_W - 9 r_W^{-1} - \frac{9}{2R} r_Z^{-1} - \frac{1}{M_W^2} Tr\, m_i^2 + \\
&+ \quad \frac{6}{M_W^2 M_\chi^2} Tr\, m_i^4 \Bigg] P + \frac{\Pi^\chi(tadpoles)}{M_\chi^2} - \frac{5}{2} - \frac{5}{4R} + \frac{27}{8} r_W + \frac{9}{2} r_W^{-1} + \frac{9}{4R} r_Z^{-1} - \\
&- \quad \frac{3}{2} r_W \log r_W + \left(\frac{1}{8} r_W - \frac{3}{4R} + \frac{9}{4R} r_Z^{-1} \right) \log R + \frac{3}{4M_W^2} Tr\, m_i^2 -
\end{aligned}
$$

$$
\begin{aligned}
&- \frac{1}{2M_W^2} Tr\, m_i^2 \log \frac{m_i^2}{M_W^2} - \frac{7}{2M_W^2 M_\chi^2} Tr\, m_i^4 + \frac{3}{M_W^2 M_\chi^2} Tr\, m_i^4 \log \frac{m_i^2}{M_W^2} + \\
&+ \left(\frac{r_W}{8} - \frac{1}{2} + \frac{3}{2} r_W^{-1}\right) \frac{1}{M_\chi^2} L(-M_\chi^2, M_W^2, M_W^2) + \\
&+ \left(\frac{r_Z}{16} - \frac{1}{4} + \frac{3}{4} r_Z^{-1}\right) \frac{1}{R} \frac{1}{M_\chi^2} L(-M_\chi^2, M_Z^2, M_Z^2) + \\
&+ \frac{9}{16 M_W^2} L(-M_\chi^2, M_\chi^2, M_\chi^2) + \\
&+ \frac{1}{4 M_W^2 M_\chi^2} Tr\, m_i^2 L(-M_\chi^2, m_i^2, m_i^2) - \frac{1}{M_W^2 M_\chi^4} Tr\, m_i^4 L(-M_\chi^2, m_i^2, m_i^2) \Bigg\}
\end{aligned} \tag{2.8}
$$

and

$$
\begin{aligned}
Z_\chi - 1 = \frac{ig^2}{16\pi^2} \Bigg\{ &\left[-3 - \frac{3}{2R} + \frac{3}{2} r_W + \frac{1}{M_W^2} Tr\, m_i^2\right] P + \frac{3}{2} + \frac{3}{4R} + 3 r_W^{-1} + \\
&+ \frac{3}{2R} r_Z^{-1} + \left(\frac{3}{4R} - \frac{1}{4} r_W\right) \log R - \frac{1}{4M_W^2} Tr\, m_i^2 + \frac{1}{2M_W^2} Tr\, m_i^2 \log \frac{m_i^2}{M_W^2} - \\
&- \frac{2}{M_W^2 M_\chi^2} Tr\, m_i^4 + \left(\frac{1}{4} - \frac{1}{4} r_W - \frac{3}{r_W(r_W - 4)}\right) \frac{1}{M_\chi^2} L(-M_\chi^2, M_W^2, M_W^2) + \\
&+ \left(\frac{1}{8} - \frac{1}{8} r_Z - \frac{3}{2 r_Z (r_Z - 4)}\right) \frac{1}{R} \frac{1}{M_\chi^2} L(-M_\chi^2, M_Z^2, M_Z^2) + \\
&+ \frac{3}{8} \frac{1}{M_W^2} L(-M_\chi^2, M_\chi^2, M_\chi^2) - \\
&- \frac{1}{4 M_W^2 M_\chi^2} Tr\, m_i^2 L(-M_\chi^2, m_i^2, m_i^2) - \frac{1}{2 M_W^2 M_\chi^4} Tr\, m_i^4 L(-M_\chi^2, m_i^2, m_i^2) \Bigg\}
\end{aligned} \tag{2.9}
$$

Consequently,

$$
\begin{aligned}
&\Pi^{ren}(q^2) = \Pi^\chi(q^2) - \delta M_\chi^2 - (Z_\chi - 1)(q^2 + M_\chi^2) = \frac{ig^2}{16\pi^2} M_\chi^2 \times \\
&\times \Bigg\{ \left[-\frac{3}{4} \frac{q^4}{M_W^2 M_\chi^2} - \frac{3}{4} r_W - \frac{3}{2} \frac{q^2}{M_W^2}\right] P + \frac{3q^4}{4 M_W^2 M_\chi^2} + \frac{q^4}{8 M_W^2 M_\chi^2} \log R + \\
&+ \frac{q^2}{M_\chi^2} \left(1 + \frac{1}{2R} - 3 r_W^{-1} - \frac{3}{2R} r_Z^{-1}\right) + \frac{q^2}{4 M_W^2} \log R + \frac{1}{8} r_W \log R +
\end{aligned}
$$

$$
\begin{aligned}
&+ \quad 1+\frac{1}{2R}-\frac{3}{4}r_W-3r_W^{-1}-\frac{3}{2R}r_Z^{-1}-\left(\frac{q^2}{M_\chi^2}+1\right)\frac{1}{2M_W^2}Tr\, m_i^2+\\
&+ \quad \left(\frac{q^2}{M_\chi^2}+1\right)\frac{2}{M_W^2M_\chi^2}Tr\, m_i^4-\left(\frac{q^2}{8M_W^2}+\frac{1}{2}+\frac{3M_W^2}{2q^2}\right)\times\\
&\times \quad \frac{1}{M_\chi^2}L(q^2,M_W^2,M_W^2)-\left(\frac{q^2}{16M_Z^2}+\frac{1}{4}+\frac{3M_Z^2}{4q^2}\right)\frac{1}{R}\frac{1}{M_\chi^2}L(q^2,M_Z^2,M_Z^2)-\\
&- \quad \frac{9}{16q^2}r_W L(q^2,M_\chi^2,M_\chi^2)+\frac{1}{4M_W^2M_\chi^2}Tr\, m_i^2 L(q^2,m_i^2,m_i^2)+\\
&+ \quad \frac{1}{M_W^2M_\chi^2}\frac{1}{q^2}Tr\, m_i^4 L(q^2,m_i^2,m_i^2)+\left(-\frac{q^2}{4M_\chi^2}+\frac{q^2}{4M_W^2}-\frac{3q^2}{M_\chi^2r_W(r_W-4)}+\right.\\
&+ \quad \left.\frac{1}{4}+\frac{1}{8}r_W-\frac{3}{2}r_W^{-1}+\frac{3}{r_W(r_W-4)}\right)\frac{1}{M_\chi^2}L(-M_\chi^2,M_W^2,M_W^2)+\\
&+ \quad \left(-\frac{q^2}{8M_\chi^2}+\frac{q^2}{8M_Z^2}+\frac{3q^2}{M_\chi^2r_Z(r_Z-4)}+\frac{1}{8}+\frac{1}{16}r_Z-\frac{3}{4}r_Z^{-1}+\right.\\
&+ \quad \left.\frac{3}{2r_Z(r_Z-4)}\right)\frac{1}{R}\frac{1}{M_\chi^2}L(-M_\chi^2,M_Z^2,M_Z^2)-\\
&- \quad \left(\frac{3q^2}{8M_W^2}+\frac{15}{16}r_W\right)\frac{1}{M_\chi^2}L(-M_\chi^2,M_\chi^2,M_\chi^2)+\\
&+ \quad \frac{q^2}{4M_W^2M_\chi^4}Tr\, m_i^2 L(-M_\chi^2,m_i^2,m_i^2)+\frac{1}{2M_W^2M_\chi^4}\left(3+\frac{q^2}{M_\chi^2}\right)\times\\
&\times \quad Tr\, m_i^4 L(-M_\chi^2,m_i^2,m_i^2)\Big\} \qquad (2.10)
\end{aligned}
$$

In this Section and in what follows $r_W = M_\chi^2/M_W^2$, $r_Z = M_\chi^2/M_Z^2$, $b_{1,2}$ are constants defined by the strength of the Higgs -fermion pseudoscalar interaction. [2] The form of the integral $I_0(q^2, M_1^2, M_2^2)$ is given in *Appendix A*.

[2] In the Standard Model they are equal to zero.

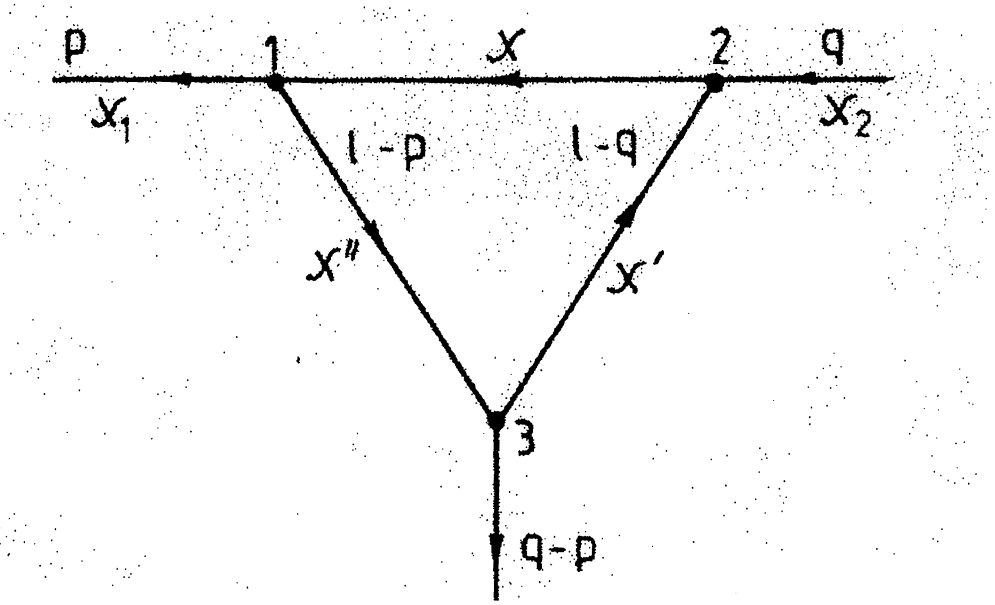

Figure 6:

2.2 Vertex diagrams.

The technique of the calculation of the diagrams shown below is very much alike to that suggested in paper [15].

$$\Gamma(p^2,q^2,(p-q)^2)=\frac{if_1^{3\chi}f_2^{3\chi}f_3^{3\chi}}{16\pi^2}I_1(q^2,(p-q)^2,p^2,M_\chi^2,M_{\chi'}^2,M_{\chi''}^2). \quad (2.11)$$

and a similar diagram with the opposite lepton current direction give

$$\begin{aligned}\Gamma(p^2,q^2,(p-q)^2)=&\frac{if_1^{\chi}f_2^{\chi}f_3^{\chi}}{4\pi^2}\{[-2m_1B_1-2m_2B_2-2m_3B_3]\,P-\\
-&\frac{m_1B_1+m_2B_2+m_3B_3}{2}-\frac{m_1B_1+m_2B_2}{2}I_0(q^2,m_1^2,m_2^2)-\\
-&\frac{m_1B_1+m_3B_3}{2}I_0(p^2,m_1^2,m_3^2)-\frac{m_2B_2+m_3B_3}{2}I_0((p-q)^2,m_2^2,m_3^2)-\\
-&\frac{1}{2}\left[\left(m_1(p-q)^2+m_1m_2^2+m_1m_3^2\right)B_1+\right.\\
+&\left(m_2p^2+m_2m_1^2+m_2m_3^2\right)B_2+\left(m_3q^2+m_3m_1^2+m_3m_2^2\right)B_3+\\
+&\left.2m_1m_2m_3B_4\right]I_1(q^2,(p-q)^2,p^2,m_1^2,m_2^2,m_3^2)\Big\}.\end{aligned}$$

where

$$\begin{aligned}B_1&=1+b_1b_2-b_1b_3-b_2b_3,\\
B_2&=1-b_1b_2-b_1b_3+b_2b_3,\\
B_3&=1-b_1b_2+b_1b_3-b_2b_3,\\
B_4&=1+b_1b_2+b_1b_3+b_2b_3. \quad (2.12)\end{aligned}$$

and a similar diagram with the opposite loop current direction

$$\begin{aligned}\Gamma(p^2,q^2,(p-q)^2)=&\frac{if_1^{V\chi}f_2^{V\chi}f_3^{V\chi}}{16\pi^2}\left\{\left[-\frac{3}{4}\frac{p^2+q^2+(p-q)^2}{M_V^4}-\right.\right.\\
-&\left.\left.\frac{1}{8}\frac{(p^2+q^2+(p-q)^2)^2}{M_V^6}\right]P+\frac{p^2+q^2+(p-q)^2}{4M_V^4}\left(1-\log\frac{M_V^2}{M_W^2}\right)-\right.\\
-&\left.\left[\frac{1}{4M_V^4}\left(\frac{p^2+q^2-(p-q)^2}{2}+p^2-q^2\right)+\frac{p^2(p^2+q^2+(p-q)^2)}{16M_V^6}\right]\times\right.\end{aligned}$$

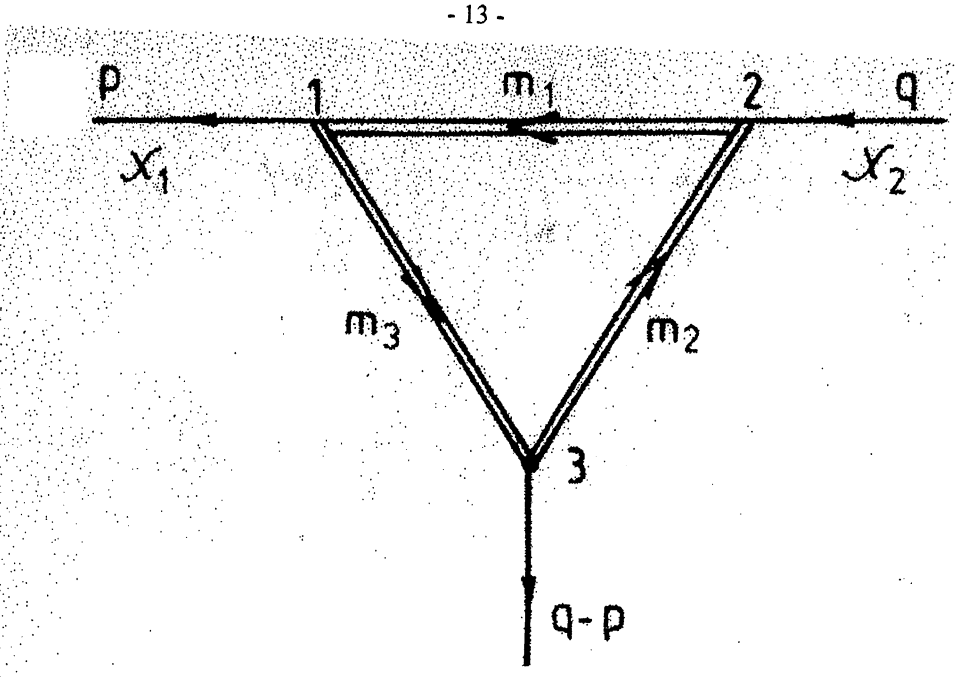

Figure 7:

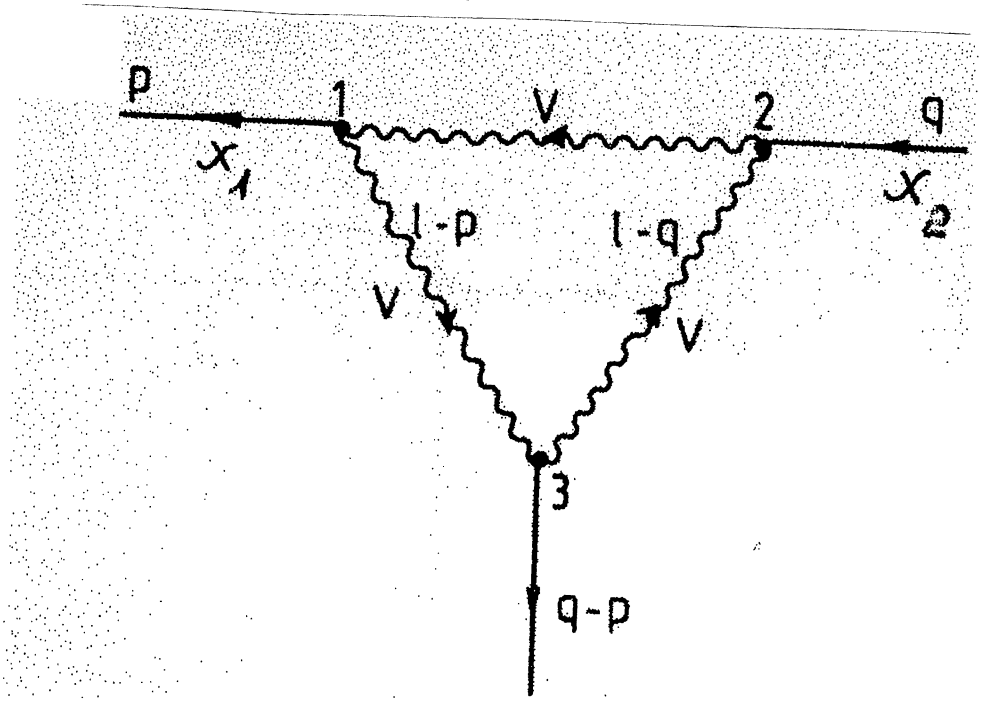

Figure 8:

$$\times \quad I_0(p^2, M_V^2, M_V^2) - \left[\frac{1}{4M_V^4}\left(\frac{p^2+q^2-(p-q)^2}{2} + q^2 - p^2\right) + \right.$$
$$+ \quad \left.\frac{q^2(p^2+q^2+(p-q)^2)}{16M_V^6}\right] I_0(q^2, M_V^2, M_V^2) + \left[\frac{1}{4M_V^4}\left(\frac{p^2+q^2-(p-q)^2}{2} - \right.\right.$$
$$- \quad \left.\left.(p-q)^2\right) - \frac{(p-q)^2(p^2+q^2+(p-q)^2)}{16M_V^6}\right] I_0((p-q)^2, M_V^2, M_V^2) +$$
$$+ \quad \left[3 + \frac{p^2+q^2+(p-q)^2}{2M_V^2} + \right.$$
$$+ \quad \frac{p^4+q^4-p^2q^2+(p-q)^4-p^2(p-q)^2-q^2(p-q)^2}{4M_V^4} -$$
$$- \quad \left.\frac{p^2q^2(p-q)^2}{8M_V^6}\right] I_1(q^2, (p-q)^2, p^2, M_V^2, M_V^2, M_V^2)\Bigg\}. \qquad (2.13)$$

The form of the integral I_1 is also given in *Appendix A*.

The diagrams can be easily derived from the self-energy diagrams (see preceding Subsection). As a sum, we get

$$\Gamma(p^2, q^2, (p-q)^2) = \frac{ig^3}{16\pi^2}\frac{M_\chi^2}{M_W}\left\{\left[\frac{3}{4}\frac{p^2q^2+p^2(p-q)^2+q^2(p-q)^2}{M_W^2M_\chi^2} - \frac{27}{8}r_W - \right.\right.$$
$$- \quad \left.\left.9r_W^{-1} - \frac{9}{2R}r_Z^{-1} + \frac{6}{M_W^2M_\chi^2}Tr\, m_i^6\right] P + \Gamma^{3\chi}(tadpoles) - \frac{p^2+q^2+(p-q)^2}{4M_\chi^2} + \right.$$
$$+ \quad \frac{p^2+q^2+(p-q)^2}{8M_\chi^2}\frac{1}{R} - \frac{3}{4}\frac{p^2q^2+p^2(p-q)^2+q^2(p-q)^2}{M_W^2M_\chi^2} -$$
$$- \quad \frac{p^2q^2+p^2(p-q)^2+q^2(p-q)^2}{8M_W^2M_\chi^2}\log R + \frac{27}{8}r_W - \frac{27}{16}r_W\log r_W + 6r_W^{-1} +$$
$$+ \quad 3\frac{1}{R}r_Z^{-1} + +\frac{9}{4}r_Z^{-1}\frac{1}{R}\log R - \frac{9}{2M_W^2M_\chi^2}Tr\, m_i^4 + \frac{3}{M_W^2M_\chi^2}Tr\ m_i^4\log\frac{m_i^2}{M_W^2} -$$
$$+ \quad \left[-\frac{3}{2}r_W^{-1} - \frac{q^2+(p-q)^2-p^2}{4M_\chi^2} + \frac{p^2(q^2+(p-q)^2)}{8M_W^2M_\chi^2}\right] \times$$
$$\times \quad \frac{1}{2p^2}L(p^2, M_W^2, M_W^2) + \left[-\frac{3}{2}r_W^{-1} - \frac{p^2+(p-q)^2-q^2}{4M_\chi^2} + \frac{q^2(p^2+(p-q)^2)}{8M_W^2M_\chi^2}\right] \times$$

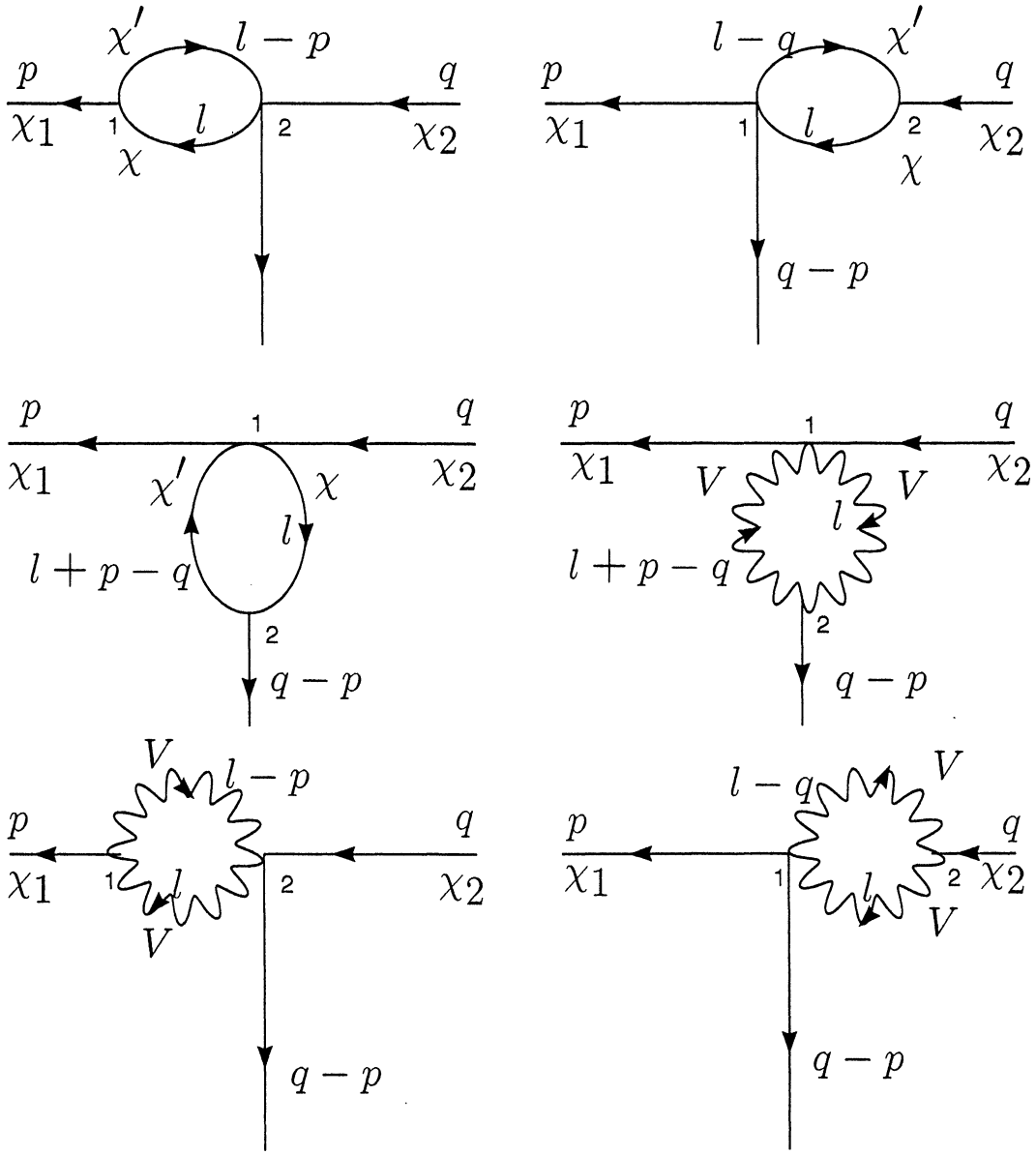
χ'
$l-p$
p
q
$\chi 1$
1
l
2
$\chi 2$
χ
$l-q$
χ'
p
q
$\chi 1$
1
l
2
$\chi 2$
χ
$q-p$
p
1
q
$\chi 1$
χ'
χ
$\chi 2$
l
$l+p-q$
2
$q-p$
p
1
q
$\chi 1$
V
V
$\chi 2$
l
$l+p-q$
2
$q-p$
V
$l-p$
p
q
$\chi 1$
1
l
2
$\chi 2$
V
$q-p$
$l-q$
V
p
q
$\chi 1$
1
l
2
$\chi 2$
V
$q-p$

Figure 9:

$$
\begin{aligned}
\times\ & \frac{1}{2q^2}L(q^2,M_W^2,M_W^2)+\left[-\frac{3}{2}r_W^{-1}-\frac{p^2+q^2-(p-q)^2-p^2}{4M_\chi^2}+\right.\\
+\ & \left.\frac{(p-q)^2(p^2+q^2)}{8M_W^2M_\chi^2}\right]\frac{1}{(p-q)^2}L((p-q)^2,M_W^2,M_W^2)+\\
+\ & \left[-\frac{3}{4R}r_Z^{-1}-\frac{q^2+(p-q)^2-p^2}{8M_\chi^2}\frac{1}{R}+\frac{p^2(q^2+(p-q)^2)}{16M_W^2M_\chi^2}\right]\frac{1}{2p^2}L(p^2,M_Z^2,M_Z^2)+\\
+\ & \left[-\frac{3}{4R}r_Z^{-1}-\frac{p^2+(p-q)^2-q^2}{8M_\chi^2}\frac{1}{R}+\frac{q^2(p^2+(p-q)^2)}{16M_W^2M_\chi^2}\right]\frac{1}{2q^2}L(q^2,M_Z^2,M_Z^2)+\\
+\ & \left[-\frac{3}{4R}r_Z^{-1}-\frac{p^2+q^2-(p-q)^2-p^2}{8M_\chi^2}\frac{1}{R}+\right.\\
+\ & \left.\frac{(p-q)^2(p^2+q^2)}{16M_W^2M_\chi^2}\right]\frac{1}{2(p-q)^2}L((p-q)^2,M_Z^2,M_Z^2)-\\
-\ & \frac{9}{16}r_W\left[\frac{1}{2p^2}L(p^2,M_\chi^2,M_\chi^2)+\frac{1}{2q^2}L(q^2,M_\chi^2,M_\chi^2)+\right.\\
+\ & \left.\frac{1}{2(p-q)^2}L((p-q)^2,M_\chi^2,M_\chi^2)\right]+\\
+\ & \frac{1}{M_W^2M_\chi^2}Tr\,m_i^4\left[\frac{1}{2p^2}L(p^2,M_\chi^2,M_\chi^2)+\frac{1}{2q^2}L(q^2,M_\chi^2,M_\chi^2)+\right.\\
+\ & \left.\frac{1}{(p-q)^2}L((p-q)^2,M_\chi^2,M_\chi^2)\right]-\frac{27}{8}r_WM_\chi^2I_1(q^2,(p-q)^2,p^2,M_\chi^2,M_\chi^2,M_\chi^2)-\\
-\ & \left[6r_W^{-1}M_W^2+(p^2+q^2+(p-q)^2)r_W^{-1}+\right.\\
+\ & \left.\frac{p^4+q^4+(p-q)^4-p^2q^2-p^2(p-q)^2-q^2(p-q)^2}{2M_\chi^2}-\right.\\
-\ & \left.\frac{p^2q^2(p-q)^2}{4M_W^2M_\chi^2}\right]I_1(q^2,(p-q)^2,p^2,M_W^2,M_W^2,M_W^2)-\\
-\ & \left[\frac{3}{R}r_Z^{-1}M_Z^2+\frac{p^2+q^2+(p-q)^2}{2R}r_Z^{-1}+\right.\\
+\ & \left.\frac{p^4+q^4+(p-q)^4-p^2q^2-p^2(p-q)^2-q^2(p-q)^2}{4RM_\chi^2}-\right.
\end{aligned}
$$

$$- \quad \frac{p^2q^2(p-q)^2}{8M_W^2M_\chi^2}\Bigg] I_1(q^2,(p-q)^2,p^2,M_Z^2,M_Z^2,M_Z^2)+$$
$$+ \quad \frac{p^2+q^2+(p-q)^2}{2M_W^2M_\chi^2} Trm_i^4 I_1(q^2,(p-q)^2,p^2,m_i^2,m_i^2,m_i^2)+$$
$$+ \quad \frac{4}{M_W^2M_\chi^2} Trm_i^6 I_1(q^2,(p-q)^2,p^2,m_i^2,m_i^2,m_i^2)\Bigg\}. \qquad (2.14)$$

The appropriate counterterm is

$$\Gamma^{c.t} = -\frac{3gM_\chi^2}{2M_W}\left[\frac{3}{2}(Z_\chi - 1) + \frac{\delta g}{g} + \frac{\delta M_\chi^2}{M_\chi^2} - \frac{\delta M_W^2}{2M_W^2}\right]. \qquad (2.15)$$

As found in [9]

$$\frac{\delta g}{g} = Z_A^{-1/2}\left(1 - \frac{\delta R}{1-R}\right)^{-1/2} - 1 \simeq \frac{1}{2}\left[\frac{\delta R}{1-R} - (Z_A - 1)\right], \qquad (2.16)$$

$$\frac{\delta R}{R} = \frac{Z_{M_W}Z_W^{-1}}{Z_{M_Z}Z_Z^{-1}} - 1 \simeq \frac{\delta M_W^2}{M_W^2} - \frac{\delta M_Z^2}{M_Z^2}, \qquad (2.17)$$

where

$$\frac{\delta M_W^2}{M_W^2} = Z_{M_W} - Z_W = \frac{ig^2}{16\pi^2}\Bigg\{\left[\frac{34}{3} - \frac{3}{2R} - \frac{1}{3}N_f + \frac{1}{M_W^2}Tr\, m_i^2\right] P - 19 + \frac{14}{9}+$$
$$+ \quad \frac{23}{12R} + \frac{1}{12R^2} - \frac{1}{2}r_W + \frac{1}{12}r_W^2 + (-\frac{7}{2} + \frac{7}{12R} + \frac{1}{24R^2})\frac{1}{R}\log R+$$
$$+ \quad (-\frac{3}{4} + \frac{1}{4}r_W - \frac{1}{24}r_W^2)r_W \log r_W + \frac{7}{36}N_f - \frac{1}{12M_W^2}Trm_i^2 - \frac{1}{6M_W^4}Trm_i^4+$$
$$+ \quad \sum_{i,j}^{N_f/2}\Bigg[\frac{m_i^2m_j^2}{3M_W^4} - (\frac{1}{3} - \frac{m_i^2+m_j^2}{2M_W^2} \times \log m_im_jM_W^2 + \frac{(m_i^2-m_j^2)^3}{12M_W^6}\log m_i^2m_j^2-$$
$$- \quad (\frac{1}{6} - \frac{m_i^2+m_j^2}{12M_W^2} - \frac{m_i^2-m_j^2)^2}{12M_W^4})\frac{1}{M_W^2}L(-M_W^2,m_i^2,m_j^2)\Bigg] K_{ij}K_{ij}^+ +$$
$$- \quad (\frac{1}{2} - \frac{r_W}{6} + \frac{r_W^2}{24})\frac{1}{M_W^2}L(-M_W^2,M_W^2,M_\chi^2) + (-\frac{17}{6} - 2R + \frac{2}{3R} + \frac{1}{24R^2})\times$$
$$\times \quad \frac{1}{M_W^2}L(-M_W^2,M_W^2,M_Z^2)\Bigg\}, \qquad (2.18)$$

and

$$\frac{\delta M_Z^2}{M_Z^2} = Z_{M_Z} - Z_Z = \frac{ig^2}{16\pi^2}\left\{\left[-\frac{7}{3} + 14R - \frac{11}{6R} - \right.\right.$$
$$- \left.\frac{1}{3}\left(2 - \frac{1}{3}\right)N_f - \frac{8}{3}\frac{(1-R)^2}{R}Tr\,Q_i^2 + \frac{1}{M_W^2}Tr\,m_i^2\right]P +$$
$$+ \frac{35}{18} - \frac{34}{3}R - 8R^2 +$$
$$- \frac{35}{18R} - \frac{1}{2}r_W + \frac{1}{12}r_W r_Z + \frac{5}{6R}\log R + \left(-\frac{3}{4} + \frac{1}{4}r_Z - \frac{1}{24}r_Z^2\right)r_W \log r_Z +$$
$$+ \left(\frac{7}{36}N_f - \frac{14}{9}Tr\,Q_i^2\right)\left(2 - \frac{1}{R}\right) + \frac{14}{9}RTr\,Q_i^2 +$$
$$+ \frac{1}{M_W^2}Tr\left[\left(-\frac{1}{12} - \frac{8}{3}|Q_i| + \frac{16}{3}Q_i^2\right)m_i^2 + \left(\frac{8}{3}|Q_i| - \frac{32}{3}Q_i^2\right)Rm_i^2 +\right.$$
$$+ \left.\frac{16}{3}Q_i^2R^2m_i^2\right] + \frac{1}{M_W^2}Tr\left[\frac{1}{2}m_i^2 - \frac{1}{3}M_Z^2\left(\frac{1}{2} - 2|Q_i| + 4Q_i^2\right) -\right.$$
$$- \left.\frac{1}{3}M_W^2\left(2|Q_i| - 8Q_i^2\right) - \frac{4M_W^2}{3M_Z^2}Q_i^2\right]\log\frac{m_i^2}{M_W^2} +$$
$$+ \left(\frac{1}{24} + \frac{2}{3}R - \frac{17}{6}R^2 - 2R^3\right)\frac{1}{M_W^2}L(-M_Z^2, M_W^2, M_W^2) +$$
$$+ \left(\frac{1}{2} - \frac{1}{6}r_Z + \frac{1}{24}r_Z^2\right)\frac{1}{M_W^2}L(-M_Z^2, M_Z^2, M_\chi^2) +$$
$$+ Tr\left[\left(\frac{1}{12} - \frac{1}{3}|Q_i| + \frac{2}{3}Q_i^2\right) + \left(\frac{1}{3}|Q_i| - \frac{4}{3}Q_i^2\right)R + \frac{2}{3}Q_i^2R^2 -\right.$$
$$- \left(\frac{1}{12} + \frac{2}{3}|Q_i| - \frac{4}{3}Q_i^2\right)\frac{m_i^2}{M_Z^2} + \left(\frac{2}{3}|Q_i| - \frac{8}{3}Q_i^2\right)R\frac{m_i^2}{M_Z^2} +$$
$$+ \left.\left.\frac{4}{3}Q_i^2R^2\frac{m_i^2}{M_Z^2}\right]\frac{1}{M_W^2}L(-M_Z^2, m_i^2, m_i^2)\right\} \qquad (2.19)$$

Finally,[3]

$$Z_A - 1 = \frac{ie^2}{16\pi^2}\left\{\left[-14 + \frac{8}{3}Tr\,Q_i^2\right]P + \frac{2}{3}\left(1 + Tr\,Q_i^2\right) + \frac{4}{3}Tr\,Q_i^2 \log\frac{m_i^2}{m_W^2}\right\}. \tag{2.20}$$

Thus,

$$\begin{aligned}\frac{\delta g}{g} = \frac{ig^2}{16\pi^2}\Bigg\{\left[\frac{43}{6} - \frac{1}{6}N_f\right]P - \frac{1}{3}(1-R)\Big(1 + Tr\,Q_i^2 + \\ + \quad 2Tr\,Q_i^2 \log\frac{m_i^2}{M_W^2}\Big) + \frac{1}{2}\frac{R}{1-R}\left[W(-1) - Z(-1)\right]\Bigg\},\end{aligned} \tag{2.21}$$

where $W(-1)$ and $Z(-1)$ are the finite parts of the counterterms $\delta M_W^2/M_W^2$ and $\delta M_Z^2/M_Z^2$, respectively. Then,

$$\begin{aligned}\Gamma^{c.t.}(p^2,q^2,(p-q)^2) = -\frac{ig^3}{16\pi^2}\frac{3M_\chi^2}{2M_W}\Bigg\{\Bigg[-\frac{3}{2}r_W - 9r_W^{-1} - \\ - \quad \frac{9}{2R}r_Z^{-1} + \frac{6}{M_W^2 M_\chi^2}Tr\,m_i^4\Bigg]P + \\ + \quad \frac{1}{2}\left(\frac{R}{1-R} - 1\right)W(-1) - \frac{1}{2}\frac{R}{1-R}Z(-1) + \\ + \quad \chi(-1) + \frac{3}{2}\chi^F(-1) - 2\Gamma^{3\chi}(tadpoles) - \\ - \quad \frac{1}{3}(1-R)\left(1 + Tr\,Q_i^2 + 2Tr\,Q_i^2\log\frac{m_i^2}{M_W^2}\right)\Bigg\} = \\ = \quad -\frac{ig^3}{16\pi^2}\frac{3M_\chi^2}{2M_W}\Bigg\{\Bigg[-\frac{3}{2}r_W - 9r_W^{-1} - \frac{9}{2R}r_Z^{-1} + \frac{6}{M_W^2 M_\chi^2}Tr\,m_i^4\Bigg]P + \\ + \quad \frac{49}{6} - \frac{28}{3}R - 4R^2 - \frac{25}{24R} - \frac{1}{24R^2} - \\ - \quad \left(\frac{10}{9} - \frac{10}{9}R\right)Tr\,Q_i^2 + \frac{29}{8}r_W - \frac{1}{4}r_W^2 + \frac{1}{4}r_W r_Z + 9r_W^{-1} + \frac{9}{2R}r_Z^{-1} +\end{aligned}$$

[3]Some difference of the renormalization constants from those given in [9] appears firstly due to the approximation $s,t,u,M_V^2,M_\chi^2 \gg m_f^2$ done there (and not used in our consideration) and, secondly, due to the different definition of the $f(d)$ function (used in the trace calculations, see *Appendix A*), that is known to not have influence the physical quantities.

$$
\begin{aligned}
&+ \left(-\frac{9}{8}+\frac{1}{8}r_Z-\frac{1}{8}r_W+\frac{1}{48}r_W^2-\frac{1}{48}r_Wr_Z-\frac{1}{48}r_Z^2\right)r_W\log r_W+\\
&+ \left(-\frac{47}{12}+\frac{7}{3R}-\frac{1}{4R^2}-\frac{1}{48R^3}+\frac{3}{8}r_Z-\frac{1}{8}r_Z^2+\frac{1}{48}r_Z^3\right)\frac{1}{1-R}\log R+\\
&+ \left(-\frac{1}{4}r_W+\frac{3}{8R}+\frac{9}{4R}r_Z^{-1}\right)\log R+\\
&+ \frac{1}{M_W^2}Tr\left[\frac{5}{12}m_i^2+\left(\frac{4}{3}|Q_i|-\frac{8}{3}Q_i^2\right)Rm_i^2+\frac{8}{3}Q_i^2R^2m_i^2\right]+\\
&+ \frac{1}{M_W^4}Tr\left[\frac{1}{12}m_i^4-\frac{1}{12}\frac{R}{1-R}m_i^4-\frac{13}{2}r_W^{-1}m_i^4\right]+\\
&+ Tr\left[\frac{m_i^2}{4M_W^2}\left(1-\frac{R}{1-R}\right)+\frac{1}{12}\frac{1}{1-R}-\frac{1}{3}|Q_i|+3\frac{m_i^4}{M_W^2M_\chi^2}\right]\log\frac{m_i^2}{M_W^2}+\\
&+ \frac{R}{1-R}\left(-\frac{1}{48}-\frac{1}{3}R+\frac{17}{12}R^2+R^3\right)\frac{1}{M_W^2}L(-M_Z^2,M_W^2,M_W^2)+\\
&+ \frac{R}{1-R}\left(-\frac{1}{4}+\frac{1}{12}r_Z-\frac{1}{48}r_Z^2\right)\frac{1}{M_W^2}L(-M_Z^2,M_Z^2,M_\chi^2)+\frac{1}{1-R}\left(-\frac{1}{4}+\frac{1}{2}R\right.\\
&+ \left.\frac{1}{12}r_W-\frac{1}{6}r_Z+\frac{1}{24}r_Wr_Z-\frac{1}{48}r_W^2\right)\frac{1}{M_W^2}L(-M_W^2,M_W^2,M_\chi^2)+\\
&+ \frac{1}{1-R}\left(\frac{25}{12}-\frac{11}{6}R-2R^2-\frac{7}{24R}-\frac{1}{48R^2}\right)\frac{1}{M_W^2}L(-M_W^2,M_W^2,M_Z^2)+\\
&+ \left(-\frac{1}{4}-\frac{1}{8}r_W^{-1}+\frac{3}{2}r_W^{-2}-\frac{9}{2}\frac{1}{r_W^2(r_W-4)}\right)\frac{1}{M_W^2}L(-M_\chi^2,M_W^2,M_W^2)+\\
&+ \left(-\frac{1}{8}-\frac{1}{16}r_Z^{-1}+\frac{3}{4}r_Z^{-2}-\frac{9}{4}\frac{1}{r_Z^2(r_Z-4)}\right)\frac{1}{M_W^2}L(-M_\chi^2,M_Z^2,M_Z^2)+\\
&+ \frac{9}{8M_W^2}L(-M_\chi^2,M_\chi^2,M_\chi^2)-\frac{1}{M_W^2}Tr\left[\frac{1}{24}\frac{R}{1-R}-\right.\\
&- \left(\frac{1}{6}|Q_i|-\frac{1}{3}Q_i^2\right)R-\frac{1}{3}Q_i^2R^2-\\
&- \left.\frac{1}{24}\frac{R}{1-R}\frac{m_i^2}{M_Z^2}-\left(\frac{1}{3}|Q_i|-\frac{2}{3}Q_i^2\right)\frac{m_i^2}{M_Z^2}R-\frac{2}{3}Q_i^2R^2\frac{m_i^2}{M_Z^2}\right]L(-M_Z^2,m_i^2,m_i^2)-\\
&- \frac{1}{M_W^2}Tr\left[\frac{m_i^2}{8M_\chi^2}+\frac{7m_i^4}{8M_\chi^4}\right]L(-M_\chi^2,m_i^2,m_i^2)+\frac{1}{2}\left(\frac{R}{1-R}-1\right)\times
\end{aligned}
$$

$$\times \sum_{ij}^{N_f/2}\left[\frac{m_i^2m_j^2}{3M_W^4}-\left(\frac{1}{3}-\frac{m_i^2+m_j^2}{2M_W^2}\right)\log\frac{m_im_j}{M_W^2}+\right.$$
$$+\frac{(m_i^2-m_j^2)^3}{12M_W^6}\log\frac{m_i^2}{m_j^2}+\left(\frac{1}{6}-\frac{1}{12}\frac{m_i^2+m_j^2}{M_W^2}-\right. \tag{2.22}$$
$$\left.\left.-\frac{1}{12}\frac{(m_i^2-m_j^2)^2}{M_W^4}\right)\frac{1}{M_W^2}L(-M_W^2,m_i^2,m_j^2)\right]K_{ij}K_{ij}^+\Bigg\}-2\Gamma^{3\chi}(tadpoles).$$

It is easy to check that the contribution of the tadpole diagrams is the following one

$$\frac{\delta M_\chi^2}{M_\chi^2}(tadpoles)=\frac{ig^2}{16\pi^2}\left\{\left[\frac{9}{4}r_W+9r_W^{-1}+\frac{9}{2R}r_Z^{-1}-\frac{6}{M_W^2M_\chi^2}Trm_i^4\right]P-\right.$$
$$-\frac{9}{8}r_W+\frac{9}{8}r_W\log r_W-\frac{3}{2}r_W^{-1}-\frac{3}{4R}r_Z^{-1}-\frac{9}{4R}r_Z^{-1}\log R+\frac{3}{2M_W^2M_\chi^2}Tr\ m_i^4-$$
$$\left.-\frac{3}{M_W^2M_\chi^2}Tr\ m_i^4\log\frac{m_i^2}{M_W^2}\right\}. \tag{2.23}$$

Using the coupling constants values from the Table I we obtain

$$\frac{\delta M_W^2}{M_W^2}(tadpoles) = \frac{2}{3}\frac{\delta M_\chi^2}{M_\chi^2}(tadpoles) \tag{2.24}$$
$$\frac{\delta M_Z^2}{M_Z^2}(tadpoles) = \frac{2}{3}\frac{\delta M_\chi^2}{M_\chi^2}(tadpoles) \tag{2.25}$$

and

$$\Gamma^{3\chi}(tadpoles)=\frac{g}{2M_W}\Pi^\chi(tadpoles). \tag{2.26}$$

Thus, one has the following additional terms in the expression for the counterterm $\Gamma^{c.t.}$ in the unitary gauge:

$$\Gamma^{c.t.}(tadpoles) = -\frac{3g}{2}\frac{M_\chi^2}{M_W}\times\frac{2}{3}\frac{\delta M_\chi^2}{M_\chi^2}(tadpoles)=$$
$$= -\frac{3g}{2}\frac{M_\chi^2}{M_W}\times\frac{2}{3}\frac{2M_W}{gM_\chi^2}\Gamma^{3\chi}(tadpoles)=-2\Gamma^{3\chi}. \tag{2.27}$$

For the counterterm $\mathcal{M}$ one has

$$\mathcal{M}^{c.t.}(tadpoles) = -\frac{3g^2}{4}\frac{M_\chi^2}{M_W^2}\times\frac{1}{3}\frac{\delta M_\chi^2}{M_\chi^2}(tadpoles) = -\frac{3g^2}{4}\frac{M_\chi^2}{M_W^2}\times\frac{1}{3}\frac{2M_W}{g}\frac{\Gamma^{3\chi}(tadpoles)}{M_\chi^2} = -\frac{g}{2M_W}\Gamma^{3\chi}. \quad (2.28)$$

As a result, the renormalized vertex is

$$\begin{aligned}
\Gamma^{ren}(p^2,q^2,(p-q)^2) = \frac{ig^3}{16\pi^2}\frac{M_\chi^2}{M_W}\Bigg\{&\left[\frac{3}{4}\frac{p^2q^2+p^2(p-q)^2+q^2(p-q)^2}{M_W^2M_\chi^2}-\frac{9}{4}r_W\right]P+\\
+\;&\frac{1}{4}\frac{p^2+q^2+(p-q)^2}{M_\chi^2}\left(1+\frac{1}{2R}\right)-\\
-\;&\frac{1}{4}\frac{p^2q^2+p^2(p-q)^2+q^2(p-q)^2}{M_W^2M_\chi^2}\left(3+\frac{1}{2}\log R\right)-\\
-\;&\frac{49}{4}+14R+6R^2+\frac{25}{16R}+\frac{1}{16R^2}-\frac{3}{2}r_W-\frac{27}{4}r_W^{-1}-\frac{27}{8R}r_Z^{-1}+\\
+\;&\frac{3}{8}r_W^2-\frac{3}{8}r_Wr_Z+\frac{5}{3}(1-R)Tr\,Q_i^2-\frac{1}{M_W^2}Tr\left[\frac{5}{8}m_i^2+\left(2|Q_i|-4Q_i^2\right)Rm_i^2\right.\\
+\;&\left.4Q_i^2R^2m_i^2\right]-\frac{1}{M_W^4}Tr\left[\frac{1}{8}m_i^4-\frac{1}{8}\frac{R}{1-R}m_i^4-\frac{9}{2}r_W^{-1}m_i^4\right]+\\
+\;&\left(\frac{3}{8}r_W-\frac{9}{16R}\right)\log R-\frac{1}{1-R}\left(-\frac{47}{8}+\frac{7}{2R}-\frac{3}{8R^2}-\frac{1}{32R^3}+\right.\\
+\;&\frac{R}{1-R}\left(-\frac{1}{48}-\frac{1}{3}R+\frac{17}{12}R^2+R^3\right)\frac{1}{M_W^2}L(-M_Z^2,M_W^2,M_W^2)+\\
+\;&\frac{R}{1-R}\left(-\frac{1}{4}+\frac{1}{12}r_Z-\frac{1}{48}r_Z^2\right)\frac{1}{M_W^2}L(-M_Z^2,M_Z^2,M_\chi^2)+\\
+\;&\frac{1}{1-R}\left(-\frac{1}{4}+\frac{1}{2}R+\right.\\
+\;&\left.\frac{1}{12}r_W-\frac{1}{6}r_Z+\frac{1}{24}r_Wr_Z-\frac{1}{48}r_W^2\right)\frac{1}{M_W^2}L(-M_W^2,M_W^2,M_\chi^2)+\\
+\;&\frac{1}{1-R}\left(\frac{25}{12}-\frac{11}{6}R-2R^2-\frac{7}{24R}-\frac{1}{48R^2}\right)\frac{1}{M_W^2}L(-M_W^2,M_W^2,M_Z^2)+\\
+\;&\left(-\frac{1}{4}-\frac{1}{8}r_W^{-1}+\frac{3}{2}r_W^{-2}-\frac{9}{2}\frac{1}{r_W^2(r_W-4)}\right)\frac{1}{M_W^2}L(-M_\chi^2,M_W^2,M_W^2)+
\end{aligned}$$

$$
\begin{aligned}
&+ \left(-\frac{1}{8}-\frac{1}{16}r_Z^{-1}+\frac{3}{4}r_Z^{-2}-\frac{9}{4}\frac{1}{r_Z^2(r_Z-4)}\right)\frac{1}{M_W^2}L(-M_\chi^2,M_Z^2,M_Z^2)+\\
&+ \frac{9}{16}r_Z-\frac{3}{16}r_Z^2+\frac{1}{32}r_Z^3\Big)\log R+\\
&+ \left(-\frac{9}{16}+\frac{3}{16}r_W-\frac{3}{16}r_Z-\frac{1}{32}r_W^2+\frac{1}{32}r_Wr_Z+\frac{1}{32}r_Z^2\right)\times\\
&\times\ r_W\log r_W-\frac{9}{8M_W^2}L(-M_\chi^2,M_\chi^2,M_\chi^2)-\\
&- \frac{1}{M_W^2}Tr\left[\frac{1}{24}\frac{R}{1-R}-\left(\frac{1}{6}|Q_i|-\frac{1}{3}Q_i^2\right)R-\frac{1}{3}Q_i^2R^2-\right.\\
&- Tr\left[\frac{3}{8}\left(1-\frac{R}{1-R}\right)\frac{m_i^2}{M_W^2}+\frac{1}{8}\frac{1}{1-R}-\frac{1}{2}|Q_i|-\frac{3m_i^4}{M_W^2M_\chi^2}\right]\log\frac{m_i^2}{M_W^2}+\\
&+ \left[-\frac{3}{2}r_W^{-1}-\frac{q^2+(p-q)^2-p^2}{4M_\chi^2}+\frac{p^2(q^2+(p-q)^2)}{8M_W^2M_\chi^2}\right]\frac{1}{2p^2}L(p^2,M_W^2,M_W^2)+\\
&+ \left[-\frac{3}{2}r_W^{-1}-\frac{p^2+(p-q)^2-q^2}{4M_\chi^2}+\frac{q^2(p^2+(p-q)^2)}{8M_W^2M_\chi^2}\right]\frac{1}{2q^2}L(q^2,M_W^2,M_W^2)+\\
&+ \left[-\frac{3}{2}r_W^{-1}-\frac{p^2+q^2-(p-q)^2}{4M_\chi^2}+\frac{(p-q)^2(p^2+q^2)}{8M_W^2M_\chi^2}\right]\times\\
&\times\ \frac{1}{2(p-q)^2}L((p-q)^2,M_W^2,M_W^2)+\\
&+ \left[-\frac{3}{4R}r_Z^{-1}-\frac{1}{8R}\frac{q^2+(p-q)^2-p^2}{M_\chi^2}+\frac{p^2(q^2+(p-q)^2)}{16M_W^2M_\chi^2}\right]\times\\
&\times\ \frac{1}{2p^2}L(p^2,M_Z^2,M_Z^2)+\\
&+ \left[-\frac{3}{4R}r_Z^{-1}-\frac{1}{8R}\frac{p^2+(p-q)^2-q^2}{M_\chi^2}+\frac{q^2(p^2+(p-q)^2)}{16M_W^2M_\chi^2}\right]\times\\
&\times\ \frac{1}{2q^2}L(q^2,M_Z^2,M_Z^2)+\\
&+ \left[-\frac{3}{4R}r_Z^{-1}-\frac{1}{8R}\frac{p^2+q^2-(p-q)^2}{M_\chi^2}+\frac{(p-q)^2(p^2+q^2)}{16M_W^2M_\chi^2}\right]\times\\
&\times\ \frac{1}{2(p-q)^2}L((p-q)^2,M_Z^2,M_Z^2)-
\end{aligned}
$$

$$
\begin{aligned}
- \quad & \frac{9}{16} r_W \left[\frac{1}{2p^2} L(p^2, M_\chi^2, M_\chi^2) + \frac{1}{2q^2} L(q^2, M_\chi^2, M_\chi^2) + \right. \\
+ \quad & \left. \frac{1}{2(p-q)^2} L((p-q)^2, M_\chi^2, M_\chi^2) \right] + \\
+ \quad & \frac{1}{M_W^2} Tr \left[\frac{1}{16} \frac{R}{1-R} - \left(\frac{1}{4} |Q_i| - \frac{1}{2} Q_i^2 \right) R - \frac{1}{2} Q_i^2 R^2 - \frac{1}{16} \frac{R}{1-R} \frac{m_i^2}{M_Z^2} - \right. \\
- \quad & \left. \frac{1}{2} \left(|Q_i| - 2Q_i^2 \right) \frac{m_i^2}{M_Z^2} R - Q_i^2 R^2 \frac{m_i^2}{M_Z^2} \right] L(-M_Z^2, m_i^2, m_i^2) + \\
+ \quad & \frac{1}{M_W^2} Tr \left[\frac{3m_i^2}{16 M_\chi^2} + \frac{21 m_i^4}{16 M_\chi^4} \right] L(-M_\chi^2, m_i^2, m_i^2) + \\
+ \quad & \frac{1}{M_W^2 M_\chi^2} Tr\, m_i^4 \left[\frac{1}{2p^2} L(p^2, m_i^2, m_i^2) + \right. \\
+ \quad & \left. \frac{1}{2q^2} L(q^2, m_i^2, m_i^2) + \frac{1}{2(p-q)^2} L((p-q)^2, m_i^2, m_i^2) \right] - \\
- \quad & \frac{3}{4} \left(\frac{R}{1-R} - 1 \right) \sum_{ij}^{N_f/2} \left[\frac{m_i m_j}{3 M_W^2} - \left(\frac{1}{3} - \frac{m_i^2 + m_j^2}{2 M_W^2} \right) \log \frac{m_i m_j}{M_W^2} + \right. \\
+ \quad & \frac{(m_i^2 - m_j^2)^3}{12 M_W^6} \log \frac{m_i^2}{m_j^2} + \\
+ \quad & \left. \left(\frac{1}{6} - \frac{m_i^2 + m_j^2}{12 M_W^6} - \frac{(m_i^2 - m_j^2)^3}{12 M_W^4} \right) \frac{1}{M_W^2} L(-M_W^2, m_i^2, m_j^2) \right] K_{ij} K_{ij}^+ - \\
- \quad & \frac{27}{8} r_W M_\chi^2 I_1(q^2, (p-q)^2, p^2, M_\chi^2, M_\chi^2, M_\chi^2) - \\
- \quad & \left[6 r_W^{-1} M_W^2 + \left(p^2 + q^2 + (p-q)^2 \right) r_W^{-1} + \right. \\
+ \quad & \left. \frac{p^4 + q^4 + (p-q)^4 - p^2 q^2 - p^2 (p-q)^2 - q^2 (p-q)^2}{2 M_\chi^2} - \frac{p^2 q^2 (p-q)^2}{4 M_W^2 M_\chi^2} \right] \times \\
\times \quad & I_1(q^2, (p-q)^2, p^2, M_W^2, M_W^2, M_W^2) - \\
- \quad & \left[\frac{3}{R} M_Z^2 r_Z^{-1} + \frac{1}{2R} \left(p^2 + q^2 + (p-q)^2 \right) r_Z^{-1} + \right. \\
+ \quad & \left. \frac{1}{4R} \frac{p^4 + q^4 + (p-q)^4 - p^2 q^2 - p^2 (p-q)^2 - q^2 (p-q)^2}{M_\chi^2} - \frac{p^2 q^2 (p-q)^2}{8 M_W^2 M_\chi^2} \right] \times \\
\times \quad & I_1(q^2, (p-q)^2, p^2, M_Z^2, M_Z^2, M_Z^2) +
\end{aligned}
$$

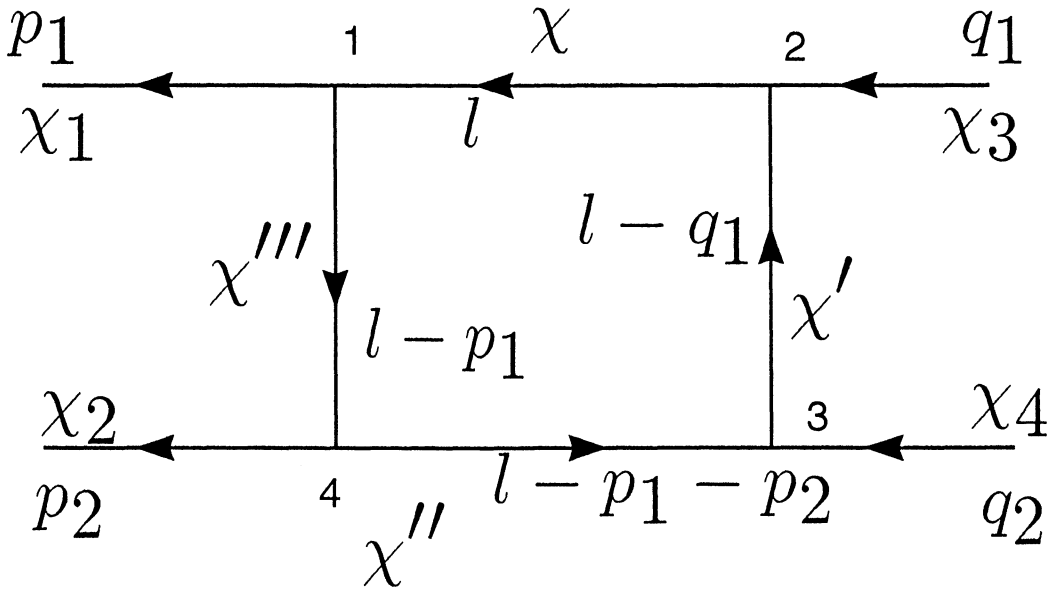

Figure 10:

$$+ \quad \frac{1}{M_W^2 M_\chi^2} Tr\, m_i^4 \left(4m_i^2 + \frac{1}{2}(p^2+q^2+(p-q)^2)\right) \times$$
$$\times \quad I_1(q^2,(p-q)^2,p^2,m_i^2,m_i^2,m_i^2)\Big\}. \tag{2.29}$$

2.3 Box diagrams.

$$i\mathcal{M}(p_1^2,p_2^2,q_1^2,q_2^2,s,t) = \frac{if_1^{3\chi}f_2^{3\chi}f_3^{3\chi}f_4^{3\chi}}{16\pi^2} I_2(q_1^2,q_2^2,p_2^2,p_1^2,s,t;M_\chi^2,M_{\chi'}^2,M_{\chi''}^2,M_{\chi'''}^2), \tag{2.30}$$

$$i\mathcal{M}(p_1^2,p_2^2,q_1^2,q_2^2,s,t) = \frac{if_1^{3\chi}f_2^{3\chi}f_3^{3\chi}f_4^{3\chi}}{16\pi^2} I_2(q_1^2,p_2^2,q_2^2,p_1^2,u,t;M_\chi^2,M_{\chi'}^2,M_{\chi''}^2,M_{\chi'''}^2). \tag{2.31}$$

The analitical result of the diagram (Fig. 12) and the similar diagram

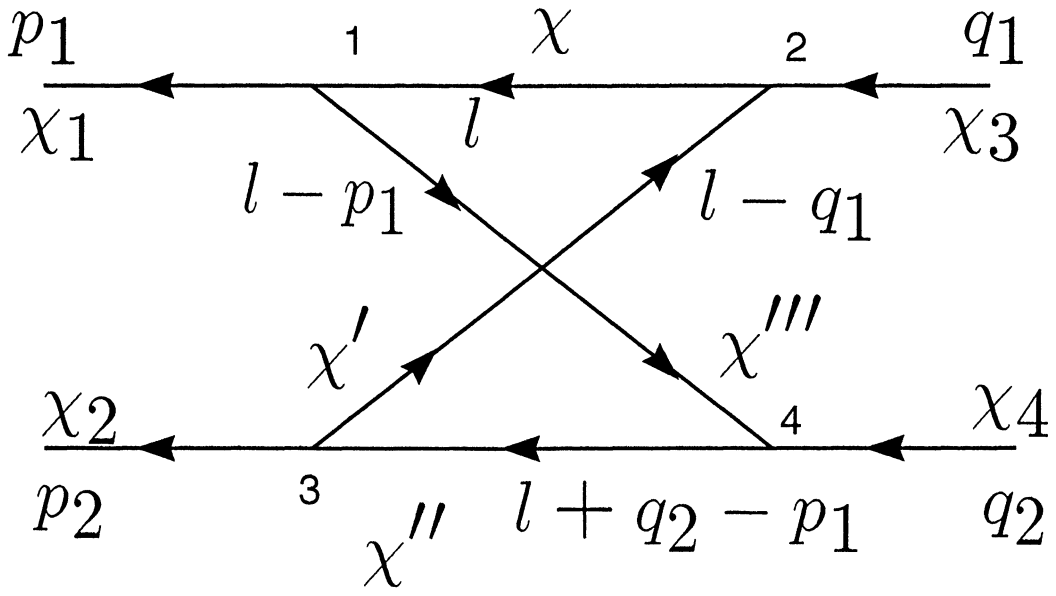

Figure 11:

with the opposite lepton current direction is

$$
\begin{aligned}
& i\mathcal{M}(p_1^2, p_2^2, q_1^2, q_2^2, s, t) = -\frac{if_1^\chi f_2^\chi f_3^\chi f_4^\chi}{4\pi^2}\left\{-2B_5P - \frac{B_5}{2} - \frac{B_5}{2}I_0(s, m_1^2, m_3^2) - \right. \\
- \quad & \frac{B_5}{2}I_0(t, m_2^2, m_4^2) + \frac{1}{2}\left[B_5\left(q_1q_2 - m_2^2\right) - B_6m_1m_2 - B_7m_1m_3 - B_9m_2m_3\right] \times \\
\times \quad & I_1(q_1^2, q_2^2, s, m_1^2, m_2^2, m_3^2) + \\
- \quad & \frac{1}{2}\left[B_5\left(q_1p_1 + m_1^2\right) - B_6m_1m_2 - B_8m_1m_4 - B_{10}m_2m_4\right] I_1(q_1^2, t, p_1^2, m_1^2, m_2^2, m_4^2) + \\
+ \quad & \frac{1}{2}\left[B_5\left(p_1p_2 - m_4^2\right) - B_7m_1m_3 - B_8m_1m_4 - B_{11}m_3m_4\right] I_1(s, p_2^2, p_1^2, m_1^2, m_3^2, m_4^2) + \\
- \quad & \frac{1}{2}\left[B_5\left(q_2p_2 - m_3^2\right) - B_9m_2m_3 - B_{10}m_2m_4 - B_{11}m_3m_4\right] I_1(q_2^2, p_2^2, t, m_2^2, m_3^2, m_4^2) + \\
+ \quad & \frac{1}{4}\left[B_5\left((q_1^2 + m_1^2 + m_2^2)(p_2^2 + m_3^2 + m_4^2) - (s + m_1^2 + m_3^2)(t + m_2^2 + m_4^2) + \right.\right. \\
+ \quad & (p_1^2 + m_1^2 + m_4^2)(q_2^2 + m_2^2 + m_3^2) + 2B_6m_1m_2(p_2^2 + m_3^2 + m_4^2) + \\
+ \quad & 2B_7m_1m_3(t + m_2^2 + m_4^2) +
\end{aligned}
$$

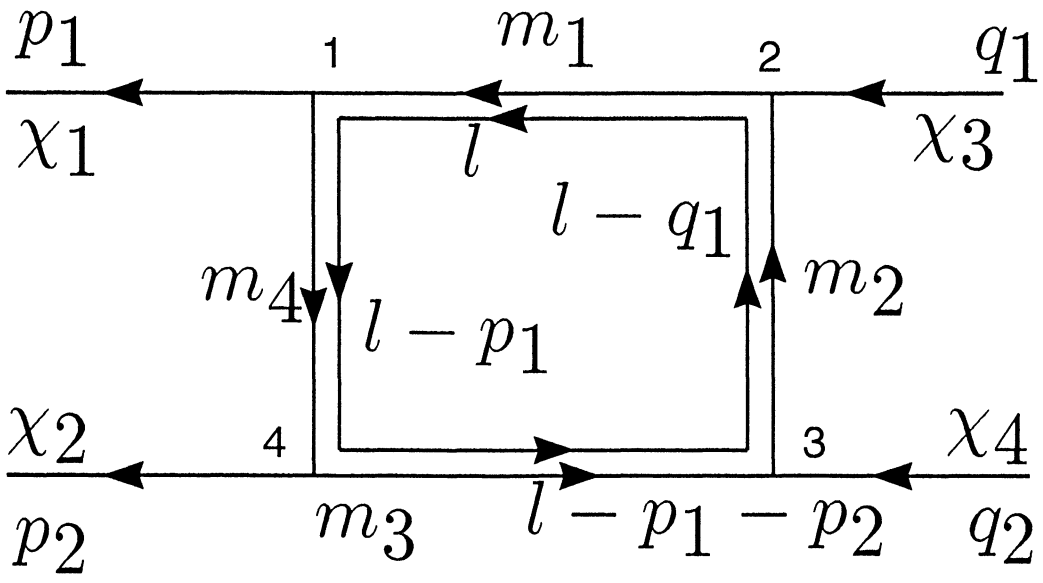

Figure 12:

$$
\begin{aligned}
&+ \quad 2B_8 m_1 m_4 (q_2^2 + m_2^2 + m_3^2) + 2B_9 m_2 m_3 (p_1^2 + m_1^2 + m_4^2) + \\
&+ \quad 2B_{10} m_2 m_4 (s + m_1^2 + m_3^2) + \\
&+ \quad 2B_{11} m_3 m_4 (q_1^2 + m_1^2 + m_2^2) + \\
&+ \quad 4B_{12} m_1 m_2 m_3 m_4] \, I_2(q_1^2, q_2^2, p_2^2, p_1^2, s, t; m_1^2, m_2^2, m_3^2, m_4^2) \Big\} ,
\end{aligned}
\tag{2.32}
$$

where

$$
\begin{aligned}
B_5 &= 1 - b_1 b_2 + b_1 b_3 - b_1 b_4 - b_2 b_3 + b_2 b_4 - b_3 b_4 + b_1 b_2 b_3 b_4, \\
B_6 &= 1 + b_1 b_2 + b_1 b_3 - b_1 b_4 + b_2 b_3 - b_2 b_4 - b_3 b_4 - b_1 b_2 b_3 b_4, \\
B_7 &= 1 + b_1 b_2 - b_1 b_3 - b_1 b_4 - b_2 b_3 - b_2 b_4 + b_3 b_4 + b_1 b_2 b_3 b_4, \\
B_8 &= 1 + b_1 b_2 - b_1 b_3 + b_1 b_4 - b_2 b_3 + b_2 b_4 - b_3 b_4 - b_1 b_2 b_3 b_4, \\
B_9 &= 1 - b_1 b_2 - b_1 b_3 - b_1 b_4 + b_2 b_3 + b_2 b_4 + b_3 b_4 - b_1 b_2 b_3 b_4, \\
B_{10} &= 1 - b_1 b_2 - b_1 b_3 + b_1 b_4 + b_2 b_3 - b_2 b_4 - b_3 b_4 + b_1 b_2 b_3 b_4, \\
B_{11} &= 1 - b_1 b_2 + b_1 b_3 + b_1 b_4 - b_2 b_3 - b_2 b_4 + b_3 b_4 - b_1 b_2 b_3 b_4, \\
B_{12} &= 1 + b_1 b_2 + b_1 b_3 + b_1 b_4 + b_2 b_3 + b_2 b_4 + b_3 b_4 + b_1 b_2 b_3 b_4,
\end{aligned}
\tag{2.33}
$$

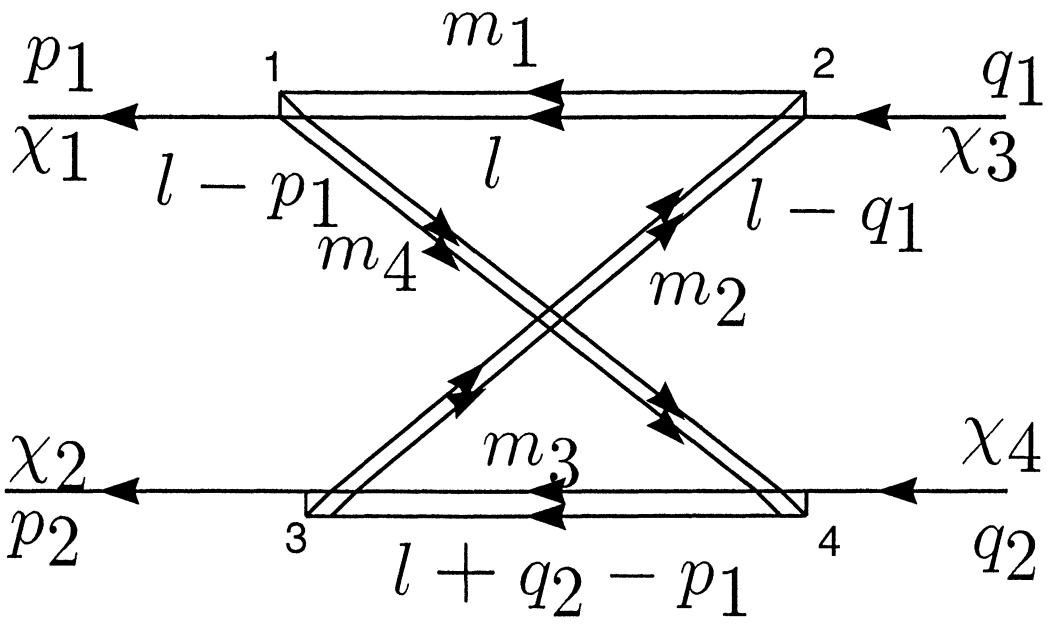

Figure 13:

The diagram (Fig. 13) and the analogous diagram with the opposite lepton current direction are described by the above expression but with the substitution $p_2 \Leftrightarrow -q_2$.

The diagram (Fig. 14) and the similar diagram with the opposite vector boson current direction are described by

$$i\mathcal{M}(p_1^2, p_2^2, q_1^2, q_2^2, s, t) = \frac{i f_1^{V\chi} f_2^{V\chi} f_3^{V\chi} f_4^{V\chi}}{16\pi^2} \left\{ \left[\frac{3}{2M_V^6} \left(s + t - p_1^2 - p_2^2 - q_1^2 - q_2^2 \right) - \right.\right.$$

$$- \frac{1}{8M_V^8} \left((p_1^2 + p_2^2 + q_1^2 + q_2^2)(p_1^2 + p_2^2 + q_1^2 + q_2^2 - \frac{s+t}{6}) + p_1^2 q_2^2 + p_2^2 q_1^2 - \right.$$

$$\left.\left. - \frac{(k_2^2 - k_1^2)(p_2^2 - p_1^2)}{3} - \frac{(k_1^2 - p_1^2)(k_2^2 - p_2^2)}{3} - \frac{s^2 + t^2 - st}{3} \right) \right] P +$$

$$+ \left[3 + \frac{1}{2M_V^2} \left(p_1^2 + p_2^2 + q_1^2 + q_2^2 \right) + \frac{1}{4M_V^4} \left(p_1^4 + p_2^4 + q_1^4 + q_2^4 + \right.\right.$$

$$\left.\left. + \; s^2 + t^2 - (s+t)(p_1^2 + p_2^2 + q_1^2 + q_2^2) + p_1^2 q_2^2 + p_2^2 q_1^2 \right) +$$

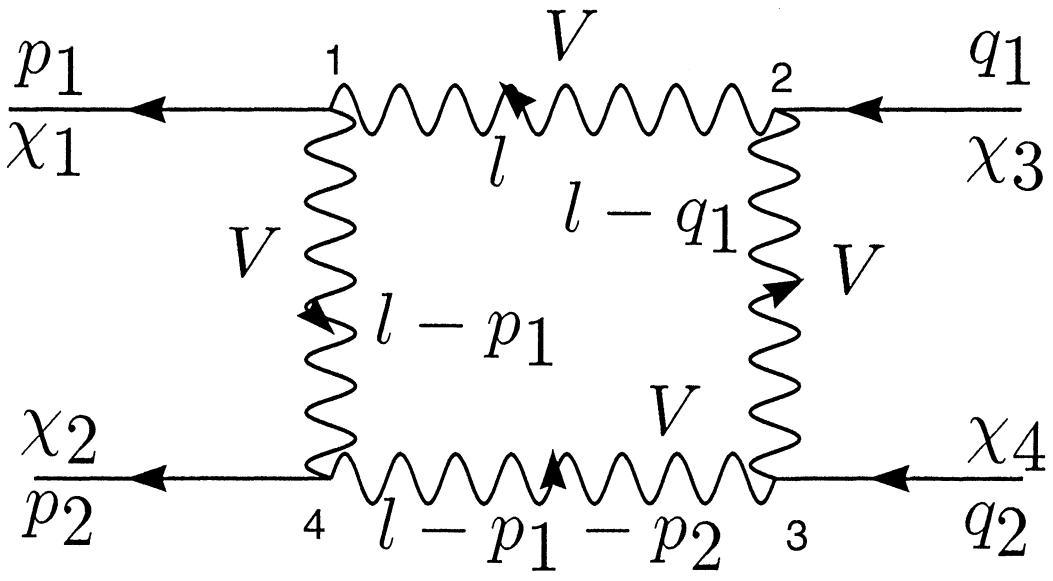

Figure 14:

$$
\begin{aligned}
&+ \quad \frac{1}{8M_V^6}\left(p_1^2p_2^2(q_1^2+q_2^2)+q_1^2q_2^2(p_1^2+p_2^2)-s(p_1^2p_2^2+q_1^2q_2^2)-t(p_1^2q_1^2+p_2^2q_2^2)\right)+\\
&+ \quad \frac{1}{16M_V^8}\left(p_1^2p_2^2q_1^2q_2^2\right)\Big] I_2(q_1^2,q_2^2,p_2^2,p_1^2,s,t,M_V^2,M_V^2,M_V^2,M_V^2)+\\
&+ \quad \Big[\frac{1}{4M_V^4}\left(-p_1^2-p_2^2+t+2s-F_1\right)+\frac{1}{8M_V^6}\left(t(q_1^2+q_2^2)+s(p_1^2+p_2^2)-st-2q_1^2q_2^2-\right.\\
&- \quad \left.p_1^2q_2^2-p_2^2q_1^2+sF_1\right)-\frac{q_1^2q_2^2}{16M_V^8}\left(p_1^2+p_2^2-t+F_1\right)\Big] I_1(q_1^2,q_2^2,s,M_V^2,M_V^2,M_V^2)+\\
&+ \quad \Big[\frac{1}{4M_V^4}\left(-q_1^2-q_2^2+t+2s-F_2\right)+\frac{1}{8M_V^6}\left(t(p_1^2+p_2^2)+s(q_1^2+q_2^2)-st-2p_1^2p_2^2-\right.\\
&- \quad \left.p_1^2q_2^2-p_2^2q_1^2+sF_2\right)-\frac{p_1^2p_2^2}{16M_V^8}\left(q_1^2+q_2^2-t+F_2\right)\Big] I_1(p_1^2,p_2^2,s,M_V^2,M_V^2,M_V^2)+\\
&+ \quad \Big[\frac{1}{4M_V^4}(-p_2^2-q_2^2+s+2t-F_3)+\frac{1}{8M_V^6}\left(s(p_1^2+q_1^2)+t(p_2^2+q_2^2)-\right.\\
&- \quad \left.st-2p_1^2q_1^2-p_1^2q_2^2-p_2^2q_1^2+tF_3\right)-
\end{aligned}
$$

$$
\begin{aligned}
&- \quad \frac{p_1^2 q_1^2}{16 M_V^8}(p_2^2 + q_2^2 - s + F_3)\Big] \, I_1(q_1^2, p_1^2, t, M_V^2, M_V^2, M_V^2) + \\
&+ \quad \Big[\frac{1}{4M_V^4}\left(-p_1^2 - q_1^2 + s + 2t - F_4\right) + \\
&+ \quad \frac{1}{8M_V^6}\left(s(p_2^2 + q_2^2) + t(p_1^2 + q_1^2) - st - 2p_2 q_2 - p_1^2 q_2^2 - p_2^2 q_1^2 + tF_4\right) - \\
&- \quad \frac{p_2^2 q_2^2}{16 M_V^8}\left(p_1^2 + q_1^2 - s + F_4\right)\Big] \, I_1(q_2^2, p_2^2, t, M_V^2, M_V^2, M_V^2) + \\
&+ \quad \Big[\frac{1}{4M_V^4}(1 + F_5 + F_6) + \frac{1}{8M_V^6}\Big(\frac{s+t+u}{2} - 2q_1^2 + p_1 q_2 + p_2^2 - q_2^2 - p_1^2 - \\
&- \quad sF_5 - tF_6) + \frac{q_1^2}{16 M_V^8}\Big(\frac{s+t+u}{2} + p_2 q_1 - p_1^2 - p_2^2 - \\
&- \quad q_1^2 - q_2^2 + q_2^2 F_5 + p_1^2 F_6\Big)\Big] \, I_0(q_1^2, M_V^2, M_V^2) + \\
&+ \quad \Big[\frac{1}{4M_V^4}(1 - F_7 - F_8) + \frac{1}{8M_V^6}\Big(\frac{s+t+u}{2} - 2q_2^2 + p_2 q_1 + p_1^2 - \\
&- \quad q_1^2 - p_2 - sF_7 - tF_8\Big) + \\
&+ \quad \frac{q_2^2}{16 M_V^8}\Big(\frac{s+t+u}{2} + p_2 q_1 - p_1^2 - p_2^2 - q_1^2 - q_2^2 + q_1^2 F_7 + p_2^2 F_8\Big)\Big] \, I_0(q_2^2, M_V^2, M_V^2) \\
&+ \quad \Big[\frac{1}{4M_V^4}(1 + F_9 + F_{10}) + \frac{1}{8M_V^6}\Big(\frac{s+t+u}{2} - 2p_1^2 + p_2 q_1 + \\
&+ \quad q_2^2 - p_2^2 - q_1^2 - sF_9 - tF_{10}\Big) + \\
&+ \quad \frac{p_1^2}{16 M_V^8}\Big(\frac{s+t+u}{2} + p_2 q_1 - p_1^2 - p_2^2 - q_1^2 - q_2^2 + q_1^2 F_9 + p_2^2 F_{10}\Big)\Big] \times \\
&\times \quad I_0(p_1^2, M_V^2, M_V^2) + \Big[\frac{1}{4M_V^4}(1 + F_{11} + F_{12}) + \\
&+ \quad \frac{1}{8M_V^6}\Big(\frac{s+t+u}{2} - 2p_2^2 + p_1 q_2 + q_1^2 - p_1^2 - q_2^2 - sF_{11} - tF_{12}\Big) + \\
&+ \quad \frac{p_2^2}{16 M_V^8}\Big(\frac{s+t+u}{2} + p_1 q_2 - p_1^2 - p_2^2 - \\
&- \quad q_1^2 - q_2^2 + p_1^2 F_{11} + q_2^2 F_{12}\Big)\Big] \, I_0(p_2^2, M_V^2, M_V^2) +
\end{aligned}
$$

$$
\begin{aligned}
&+ \left[-\frac{1}{4M_V^4}(2-F_{13}-F_{14})+\frac{1}{8M_V^6}\left(\frac{11}{6}s+\frac{5}{3}t-\frac{5}{6}p_1^2-\frac{5}{6}p_2^2-\frac{5}{6}q_1^2-\frac{5}{6}q_2^2-\right.\right.\\
&- \left.\frac{(k_2^2-k_1^2)(p_2^2-p_1^2)}{6s}-sF_{13}-sF_{14}\right)-\\
&- -\frac{1}{16M_V^8}\left(p_1^2p_2^2+q_1^2q_2^2+\frac{q_1^2p_2^2+p_1^2q_2^2}{2}-\frac{s(p_1^2+p_2^2+q_1^2+q_2^2)}{6}-\right.\\
&- \left.\left.\frac{(k_1^2-p_1^2)(k_2^2-p_2^2)}{3}-\frac{st+2s^2}{6}+q_1^2q_2^2F_{13}+p_1^2p_2^2F_{14}\right]I_0(s,M_V^2,M_V^2)-\right.\\
&- \left[-\frac{1}{4M_V^4}(2-F_{15}-F_{16})+\frac{1}{8M_V^6}\left(\frac{11}{6}s+\frac{5}{3}t-\frac{5}{6}p_1^2-\frac{5}{6}p_2^2-\frac{5}{6}q_1^2-\frac{5}{6}q_2^2+\right.\right.\\
&+ \left.\frac{(k_1^2-p_1^2)(k_2^2-p_2^2)}{6t}-tF_{15}-tF_{16}\right)-\\
&- \frac{1}{16M_V^8}\left(p_1^2q_1^2+p_2^2q_2^2+\frac{p_1^2q_2^2+p_2^2q_1^2}{2}+\frac{t(p_1^2+p_2^2+q_1^2+q_2^2)}{6}-\right.\\
&- \left.\left.\frac{(k_1^2-p_1^2)(k_2^2-p_2^2)}{3}-\frac{2t^2+st}{6}-p_1^2q_1^2F_{15}-p_2^2q_2^2F_{16}\right)\right]\times\\
&\times\ I_0(t,M_V^2,M_V^2)+\frac{1}{16M_V^6}\log\frac{M_V^2}{M_W^2}\left[s+t-\frac{14}{3}p_1^2-\frac{14}{3}p_2^2-\frac{14}{3}q_1^2-\frac{14}{3}q_2^2+\right.\\
&+ \left.\frac{(k_2^2-k_1^2)(p_2^2-p_1^2)}{3s}+\frac{(k_1^2-p_1^2)(k_2^2-p_2^2)}{3t}\right]+\\
&+ \frac{1}{4M_V^6}\left[p_1^2+p_2^2+q_1^2+q_2^2\right]+\frac{1}{16M_V^8}\left[\frac{s^2+4st+t^2}{18}+\right.\\
&+ \left.\left.\frac{(k_2^2-k_1^2)(p_2^2-p_1^2)+(k_1^2-p_1^2)(k_2^2-p_2^2)}{18}-\frac{(s+t)(p_1^2+p_2^2+k_1^2+k_2^2)}{18}\right]\right\}. \qquad (2.34)
\end{aligned}
$$

The result from Fig. 15 and the analogous diagram with the opposite vector boson current direction are obtained from the above expression but with the substitution $p_2 \Leftrightarrow -q_2$.

Here,

$$
\begin{aligned}
F_1 = &\frac{1}{s^2+q_1^4+q_2^4-2sq_1^2-2sq_2^2-2q_1^2q_2^2}\times \qquad (2.35)\\
&\left\{(t+q_1^2-p_1^2)\left[(s+q_1^2-q_2^2)(q_1^2-q_2^2)-2sq_1^2\right]+q_1^2(p_2^2-p_1^2+q_1^2-q_2^2)(s+q_2^2-q_1^2)\right\}
\end{aligned}
$$

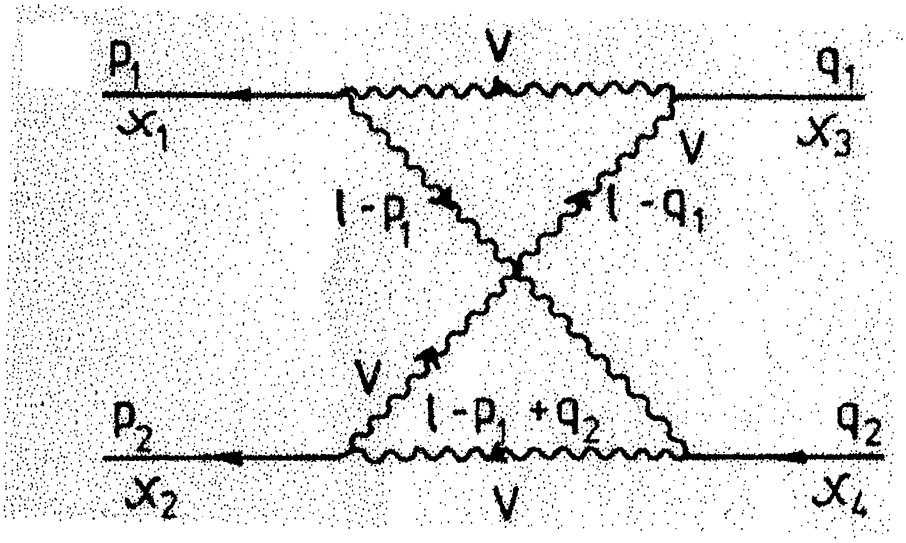

Figure 15:

$$F_2 = \frac{1}{s^2+p_1^4+p_2^4-2sp_1^2-2sp_2^2-2p_1^2p_2^2} \times \tag{2.36}$$
$$\left\{(t+p_1^2-q_1^2)\left[(s+p_1^2-p_2^2)(p_1^2-p_2^2)-2sp_1^2\right]+p_1^2(p_1^2-p_2^2+q_2^2-q_1^2)(s+p_2^2-p_1^2)\right\}$$

$$F_3 = \frac{1}{t+p_1^4+q_1^4-2p_1^2q_1^2-2tp_1^2-2tq_1^2} \times \tag{2.37}$$
$$\left\{(s+q_1^2-q_2^2)\left[(t+q_1^2-p_1^2)(q_1^2-p_1^2)-2tq_1^2\right]+q_1^2(p_2^2-p_1^2+q_1^2-q_2^2)(t+p_1^2-q_1^2)\right\}$$

$$F_4 = \frac{1}{t^2+p_2^4+q_2^4-2tp_2^2-2tq_2^2-2p_2^2q_2^2} \times \tag{2.38}$$
$$\left\{(s+q_2^2-q_1^2)\left[(t+q_2^2-p_2^2)(q_2^2-p_2^2)-2tq_2^2\right]+q_2^2(p_1^2-p_2^2+q_2^2-q_1^2)(t+q_2^2-p_2^2)\right\}$$

$$F_5 = \frac{(t+q_1^2-p_1^2)(s+q_1^2-q_2^2)+2q_1^2(p_1^2-p_2^2+q_2^2-q_1^2)}{s^2+q_1^4+q_2^4-2sq_1^2-2sq_2^2-2q_1^2q_2^2} \tag{2.39}$$

$$F_6 = \frac{(s+q_1^2-q_2^2)(t+q_1^2-p_1^2)+2q_1^2(p_1^2-p_2^2+q-2^2-q_1^2)}{t^2+p_1^4+q_1^4--2tp_1^2-2tq_1^2-2p_1^2q_1^2} \tag{2.40}$$

$$F_7 = \frac{(t+q_1^2-p_1^2)(s+q_2^2-q_1^2)+(p_1^2-p_2^2+q_2^2-q_1^2)(s-q_1^2-q_2^2)}{s^2+q_1^4+q_2^4-2sq_1^2-2sq_2^2-2q_1^2q_2^2} \tag{2.41}$$

$$F_8 = \frac{(s+q_2^2-q_1^2)(t+q_2^2-p_2^2)+2q_2^2(p_2^2-p_1^2+q_1^2-q_2^2)}{t^2+p_2^4+q_2^4-2tp_2^2-2tq_2^2-2p_2^2q_2^2} \tag{2.42}$$

$$F_9 = \frac{(t+p_1^2-q_1^2)(s+p_1^2-p_2^2)+2p_1^2(p_2^2-p_1^2+q_1^2-q_2^2)}{s^2+p_1^4+p_2^4-2sp_1^2-2sp_2^2-2p_1^2p_2^2} \tag{2.43}$$

$$F_{10} = \frac{(s+q_1^2-q_2^2)(t+p_1^2-q_1^2)+(t-q_1^2-p_1^2)(p_2^2-p_1^2+q_1^2-q_2^2)}{t^2+p_1^4+q_1^4-2tp_1^2-2tq_1^2-2p_1^2q_1^2} \tag{2.44}$$

$$F_{11} = \frac{(t+p_1^2-q_1^2)(s+p_2^2-p_1^2)+(s-p_1^2-p_2^2)(p_2^2-p_1^2+q_1^2-q_2^2)}{s^2+p_1^4+p_2^4-2sp_1^2-2sp_2^2-2p_1^2p_2^2} \tag{2.45}$$

$$F_{12} = \frac{(s+q_2^2-q_1^2)(t+p_2^2-q_2^2)+(t-p_2^2-q_2^2)(p_2^2-p_1^2+q_1^2-q_2^2)}{t^2+p_2^4+q_2^4-2tp_2^2-2tq_2^2-2p_2^2q_2^2} \tag{2.46}$$

$$F_{13} = \frac{-2s(t+q_1^2-p_1^2)+(s+q_1^2-q_2^2)(p_1^2-p_2^2+q_2^2-q_1^2)}{s^2+q_1^4+q_2^4-2sq_1^2-2sq_2^2-2q_1^2q_2^2} \tag{2.47}$$

$$F_{14} = \frac{-2s(t+p_1^2-q_1^2)+(s+p_1^2-p_2^2)(p_1^2-p_2^2+q_2^2-q_1^2)}{s^2+p_1^4+p_2^4-2sp_1^2-2sp_2^4-2p_1^2p_2^2} \quad (2.48)$$

$$F_{15} = \frac{-2t(s+q_1^2-q_2^2)+(t+q_1^2-p_1^2)(p_1^2-p_2^2+q_2^2-q_1^2)}{t^2+p_1^4+q_1^4-2tp-1^2-2tq_1^2-2q_1^2q_2^2} \quad (2.49)$$

$$F_{16} = \frac{-2t(s+q_2^2-q_1^2)+(t+q_2^2-p_2^2)(p_1^2-p_2^2+q_2^2-q_1^2)}{t^2+p_2^4+q_2^4-2tp_2^2-2tq_2^2-2p_2^2q_2^2} \quad (2.50)$$

and

$$\begin{aligned} p_1p_2 &= \frac{1}{2}\left(s-p_1^2-p_2^2\right), \qquad p_1q_2 = \frac{1}{2}\left(s+t-p_2^2-q_1^2\right), \\ q_1q_2 &= \frac{1}{2}\left(s-q_1^2-q_2^2\right), \qquad p_2q_1 = \frac{1}{2}\left(s+t-p_1^2-q_2^2\right), \\ p_1q_1 &= -\frac{1}{2}\left(t-p_1^2-q_1^2\right), \\ p_2q_2 &= -\frac{1}{2}\left(t-p_2^2-q_2^2\right) \end{aligned} \quad (2.51)$$

with s, t, u being the Mandelstam variables. I_0, I_1, I_2 are the scalar one-loop integrals calculated in [14].

3 The one-loop amplitudes.

The box diagrams of the previous Section and the diagrams drawn at *Fig. 16* (see also [13b]) contribute to the Higgs-Higgs amplitude up to fourth order of perturbation theory to give

$$i\mathcal{M}_a = \frac{9ig^2}{4} r_W \frac{M_\chi^2}{t+M_\chi^2}, \quad (3.52)$$

$$i\mathcal{M}_{b,c} = -\frac{3g}{2} r_W \frac{M_W \Gamma^{ren}(p_{1,2}^2, q_{1,2}^2, t)}{t+M_\chi^2}, \quad (3.53)$$

$$i\mathcal{M}_{d,e} = \frac{9g^2}{4} r_W \frac{M_\chi^2 \Pi^{ren}(p_{1,2}^2)}{(p_{1,2}^2+M_\chi^2)(t+M_\chi^2)}, \quad (3.54)$$

$$i\mathcal{M}_{f,g} = \frac{9g^2}{4} r_W \frac{M_\chi^2 \Pi^{ren}(q_{1,2}^2)}{(q_{1,2}^2+M_\chi^2)(t+M_\chi^2)}, \quad (3.55)$$

$$i\mathcal{M}_h = \frac{9g^2}{4} r_W \frac{M_\chi^2 \Pi^{ren}(t)}{(t+M_\chi^2)^2}, \tag{3.56}$$

$$i\mathcal{M}_i = \frac{9g^4}{16} r_W^2 \Pi^{(3)}(t), \tag{3.57}$$

$$i\mathcal{M}_j = \frac{g^4}{4}\Pi^{(5)}(t)|_{M_V^2=M_W^2} + \frac{g^4}{4}\frac{1}{R^2}\Pi^{(5)}(t)|_{M_V^2=M_Z^2}, \tag{3.58}$$

$$i\mathcal{M}_{k,l} = -\frac{27}{16} g^4 r_W^2 M_\chi^2 \Gamma^{(1)}(p_{1,2}^2, q_{1,2}, t), \tag{3.59}$$

$$\begin{aligned} i\mathcal{M}_{m,n} = & -\frac{g^4}{2} M_W^2 \Gamma^{(3)}(p_{1,2}^2, q_{1,2}, t)|_{M_V^2=M_W^2} - \\ & -\frac{g^4}{2}\frac{1}{R^2} M_Z^2 \Gamma^{(3)}(p_{1,2}^2, q_{1,2}, t)|_{M_V^2=M_Z^2}, \end{aligned} \tag{3.60}$$

$$i\mathcal{M}_o = -\frac{3ig^2}{4} r_W, \tag{3.61}$$

$$i\mathcal{M}_p = -\frac{3g^2}{4} r_W \frac{\Pi^{ren}(p_1^2)}{(p_1^2+M_\chi^2)}, \tag{3.62}$$

$$i\mathcal{M}_r = -\frac{3g^2}{4} r_W \frac{\Pi^{ren}(p_2^2)}{(p_2^2+M_\chi^2)}, \tag{3.63}$$

$$i\mathcal{M}_s = -\frac{3g^2}{4} r_W \frac{\Pi^{ren}(q_1^2)}{(q_1^2+M_\chi^2)}, \tag{3.64}$$

$$i\mathcal{M}_t = -\frac{3g^2}{4} r_W \frac{\Pi^{ren}(q_2^2)}{(q_2^2+M_\chi^2)}. \tag{3.65}$$

The digrams describing the interaction of two Higgs particle (s-channel)are presnted in [13], a solid line corresponds to the renormalized propagator and a black circle, to the renormalized vertex.

In the framework of the renormalization scheme [9] (using the unitary gauge) the appropriate counterterm for 4χ interaction is written as follows:

$$i\mathcal{M}^{c.t.} = -\frac{3g^2 M_\chi^2}{4M_W^2}\left[2(Z_\chi - 1) + 2\frac{\delta g}{g} + \frac{\delta M_\chi^2}{M_\chi^2} - \frac{\delta M_W^2}{M_W^2}\right]. \tag{3.66}$$

After substitution of the renormalization constants (see preceding Section) we have

$$i\mathcal{M}^{c.t}(p_1^2, p_2^2, q_1^2, q_2^2, s, t) = -\frac{ig^4}{16\pi^2}\frac{3r_W}{4}\left\{\left[-\frac{3}{4}r_W - 9r_W^{-1} - \frac{9}{2R}r_Z^{-1} + \right.\right.$$

$$
\begin{aligned}
&+ \quad \frac{6}{M_W^2 M_\chi^2} Tr\, m_i^4 \Big] P + \frac{52}{3} - \frac{56}{3}R - 8R^2 - \frac{19}{12R} - \frac{1}{12R^2} + \frac{31}{8} r_W - \\
&- \quad \frac{1}{2} r_W^2 + \frac{1}{2} r_W r_Z + \frac{21}{2} r_W^{-1} + \frac{21}{4R} r_Z^{-1} + \\
&+ \quad (-\frac{3}{8} r_W + \frac{3}{4R} + \frac{9}{4R} r_Z^{-1}) \log R + \frac{1}{1-R} (-\frac{47}{6} + \frac{14}{3R} - \frac{1}{2R^2} - \frac{1}{24R^3} + \\
&+ \quad \frac{3}{4} r_Z - \frac{1}{4} r_Z^2 + \frac{1}{24} r_Z^3) \log R + (-\frac{3}{4} - \frac{1}{4} r_W + \frac{1}{4} r_Z + \frac{1}{24} r_W^2 - \\
&- \quad \frac{1}{24} r_W r_Z - \frac{1}{24} r_Z^2) r_W \log r_W - \frac{20}{9} (1-R) Tr\, Q_i^2 + \\
&+ \quad \frac{1}{2M_W^2} \frac{R}{1-R} (-\frac{1}{12} - \frac{4}{3}R + \frac{17}{3}R^2 + 4R^4) L(-M_Z^2, M_W^2, M_W^2) + \\
&+ \quad \frac{1}{2M_W^2} \frac{R}{1-R} (-1 + \frac{1}{3} r_Z - \frac{1}{12} r_Z^2) L(-M_Z^2, M_Z^2, M_\chi^2) + \\
&+ \quad \frac{1}{2M_W^2} \frac{1}{1-R} (\frac{25}{3} - \frac{22}{3}R - 8R^2 - \frac{7}{6R} - \frac{1}{12R^2}) L(-M_W^2, M_W^2, M_Z^2) + \\
&+ \quad \frac{1}{2M_W^2} \frac{1}{1-R} \Big(-1 + 2R + \frac{1}{3} r_W - \frac{2}{3} r_Z + \\
&+ \quad \frac{1}{6} r_W r_Z - \frac{1}{12} r_W^2 \Big) L(-M_W^2, M_W^2, M_\chi^2) + \\
&+ \quad \frac{1}{M_W^2} (-\frac{3}{8} + \frac{3}{2} r_W^{-2} - 6 \frac{1}{r_W^2 (r_W - 4)}) L(-M_\chi^2, M_W^2, M_W^2) + \\
&+ \quad \frac{1}{M_W^2} (-\frac{3}{16} + \frac{3}{4} r_Z^{-2} - 3 \frac{1}{r_Z^2 (r_Z - 4)}) L(-M_\chi^2, M_Z^2, M_Z^2) + \\
&+ \quad \frac{21}{16 M_W^2} L(-M_\chi^2, M_\chi^2, M_\chi^2) + \\
&+ \quad \frac{1}{M_W^2} Tr \left[\frac{1}{3} m_i^2 + (\frac{8}{3} |Q_i| - \frac{16}{3} Q_i^2) R m_i^2 + \frac{16}{3} Q_i^2 R^2 m_i^2 \right] + \\
&+ \quad \frac{1}{M_W^4} Tr \left[\frac{1}{6} m_i^4 - \frac{1}{6} \frac{R}{1-R} m_i^4 - \frac{15}{2} r_W^{-1} m_i^4 \right] + \\
&- \quad \frac{1}{M_W^2} Tr \left[\frac{1}{6} \frac{1}{1-R} M_W^2 - \frac{2}{3} |Q_i| M_W^2 + \frac{1}{2} (1 - \frac{R}{1-R}) m_i^2 + \frac{3}{M_\chi^2} m_i^4 \right] \times \\
&\times \quad \log \frac{m_i^2}{M_W^2} + \frac{1}{M_W^2} Tr \left[-\frac{1}{12} \frac{R}{1-R} + (\frac{1}{3} |Q_i^2| - \frac{2}{3} Q_i^2) R + \frac{2}{3} Q_i^2 R^2 + \right.
\end{aligned}
$$

$$+ \quad \frac{1}{12}\frac{R}{1-R}\frac{m_i^2}{M_Z^2} + (\frac{2}{3}|Q_i| - \frac{4}{3}Q_i^2)R\frac{m_i^2}{M_Z^2} + \frac{4}{3}Q_i^2R^2\frac{m_i^2}{M_Z^2}\Big] L(-M_Z^2, m_i^2, m_i^2) -$$

$$- \quad \frac{1}{M_W^2}Tr\left[\frac{m_i^2}{4M_\chi^2} + 2\frac{m_i^4}{M_\chi^4}\right] L(-M_\chi^2, m_i^2, m_i^2) + (\frac{R}{1-R} - 1)\times$$

$$\times \quad \sum_{ij}^{N_f/2}\Big[\frac{1}{3}\frac{m_i^2m_j^2}{M_W^4} - \frac{1}{3} - \frac{m_i^2+m_j^2}{2M_W^2})\log\frac{m_im_j}{M_W^2} + \frac{1}{12}\frac{(m_i^2-m_j^2)^3}{M_W^6}\log\frac{m_i^2}{m_j^2} +$$

$$+ \quad (\frac{1}{6M_W^2} - \frac{m_i^2+m_j^2}{12M_W^4} - \frac{(m_i^2-m_j^2)^2}{12M_W^6})L(-M_W^2, m_i^2, m_j^2)\Big] K_{ij}K_{ij}^+\Big\} -$$

$$- \quad \frac{g}{2M_W}\Gamma^{3\chi}(tadpoles)\,. \qquad (3.67)$$

I would also lke to note that it is not useful to use the Stuart's computer algebra programm [21] since the preparation of the input data for the two-Higgs processes would consume more time than the calculations by hand.

4 Summary.

We calculated the Higgs-Higgs amplitude in the fourth order of perturbation theory (that is, with taking into account the one-loop corrections) in the Standard Model. The results do not coincide in full with the Durand *et al.* calculations in the Feynman gauge and within the different renormalization scheme [16].[4]

There exists a rather large number of different variants of the SM extensions. The most of these models are characterized by enlarging of the Higgs sector, namely by introduction of two and even more Higgs boson doublets [23]-[25]. The supersymmetric extension of the SM [26, 27] also requires introduction of at least two doublets of the scalar particles. The interest in these models has grown up in connection with the problem of suppression of the CP violation in strong interactions [28] and the problem of $B^0\bar{B}^0$ mixing [29] because they give the alternative theoretical solution to the problem of electroweak violation of the CP invariance [25, 30]. Therefore, in the approaching paper we are going to consider the Higgs-Higgs

[4]Recently, several authors proposed models which depended on the 4-potential, and, hence, on the gauge.

interaction problem in the framework of the extended variants of the SM. This is easily possible due to introduction of the parameters a_i, b_i for the fermionic interactions.

Acknowledgements. The author express his sincere gratitude to D. Yu. Bardin, R. N. Faustov, and Yu. N. Tyukhtyaev for valuable discussions. I appreciate very much the assistance of V. I. Kikot' in calculations and I thank N. B. Skachkov for putting forward the problem.

Appendix.

The integrals I_0, I_1 and I_2 are taken from the t'Hooft-Veltaman paper [14]

$$I_0(q^2, M_1^2, M_2^2) = \int_0^1 dx \log \frac{q^2 x(1-x) + M_1^2 x + M_2^2(1-x)}{M_W^2} =$$
$$= -2 + \log \frac{M_1 M_2}{M_W^2} - \frac{1}{2}\frac{M_1^2 - M_2^2}{q^2} \log \frac{M_1^2}{M_2^2} + \frac{1}{2q^2} L(q^2, M_1^2, M_2^2) \quad (4.68)$$

where

$$L(q^2, M_1^2, M_2^2) = \Big[(q^2 + M_1^2 + M_2^2) -$$
$$- \quad 4M_1^2 M_2^2\Big] \int_0^1 \frac{dx}{q^2 x(1-x) + M_1^2 x + M_2^2(1-x)}, \quad (4.69)$$

see Ref. [9a,p.440].

Next,

$$I_1(q^2, (p-q)^2, p^2, M_1^2, M_2^2, M_3^2) = \int_0^1 dx \int_0^x dy \Big[ax^2 + by^2 + cxy +$$
$$+ \quad dx + ey + f\Big]^{-1}, \quad (4.70)$$

with

$a = -(p-q)^2$, $\quad d = M_2^2 - M_3^2 + (p-q)^2$

$b = -q^2$, $\quad e = M_1^2 - M_2^2 + 2pq - q^2$

$c = -2(pq - q^2)$, $\quad f = M_3^2 - i\epsilon$.

And,

$$I_2(q_1^2, q_2^2, p_2^2, p_1^2, s, t, M_1^2, M_2^2, M_3^2, M_4^2) = \quad (4.71)$$

$$= \int_0^1 dx \int_0^x dy \int_0^y dz \left[ax^2 + by^2 + gz^2 + cxy + hxz + jyz + \right.$$
$$+ \left. dx + ey + kz + f\right]^{-2},$$

with

$a = -p_2^2$, $f = M_4^2 - i\epsilon$
$b = -q_2^2$, $g = -q_1^2$
$c = 2p_2q_2$, $h = 2p_2q_1$
$d = M_3^2 - M_4^2 + p_2^2$, $j = -2q_1q_2$
$e = M_2^2 - M_3^2 + q^2 - 2p_2q_2$, $k = M_1^2 - M_2^2 + q_1^2 + 2q_1q_2 - 2q_1p_2$.

The traces of γ- matrices in an d-dimensional space are

$$Tr\,\gamma_\alpha = Tr\,\gamma_5 = Tr\,\gamma_\alpha\gamma_\beta\gamma_5 = 0, \tag{4.72}$$
$$Tr\,\gamma_\alpha\gamma_\beta = f(d)\delta_{\alpha\beta}, \tag{4.73}$$
$$Tr\,\gamma_\alpha\gamma_\beta\gamma_\rho\gamma_\sigma = f(d)d_{\alpha\beta\rho\sigma}, \tag{4.74}$$
$$Tr\,\gamma_\alpha\gamma_\beta\gamma_\rho\gamma_\sigma\gamma_5 = f(d)\epsilon_{\alpha\beta\rho\sigma}, \tag{4.75}$$

where

$$d_{\alpha\beta\rho\sigma} = \delta_{\alpha\beta}\delta_{\rho\sigma} - \delta_{\alpha\rho}\delta_{\beta\sigma} + \delta_{\alpha\sigma}\delta_{\beta\rho}. \tag{4.76}$$

In the present work we use $f(d) = 2\omega = 4 - 2\epsilon$, d is the dimension of the space in the dimensional regularization.

References

[1] LHC Reports, CERN-LHC-2001-001 to 007, CERN-LHC-2002-001 to 024.

[2] R. N. Cahn and M. Suzuki, *Phys. Lett.* **134B**(1-2), 115-119 (1984).

[3] M.Anselmino *et al.*, *Phys. Lett.* **147B**(1-3), 207-211 (1984).

[4] J.A.Grifols, *Phys. Lett.* **264B**(1-2), 149-153 (1991); J. A. Grifols and J. L. Diaz Cruz, UAB-FT-280-92, Dec. 1991.

[5] G. Passarino, *Phys. Lett.* **156B**(3-4), 231-235 (1985); *ibid.* **161B**(4-6), 341-346 (1985).

[6] M. Veltman, *Phys. Lett.* **139B**(4), 307-309 (1984).

[7] R. Casalbuoni *et al.*, *Int. J. Mod. Phys.* **A4**(5), 1065-1110 (1989).

[8] M. Veltman and F. Yndurain, *Nucl. Phys.* **B325**(1), 1-17 (1989).

[9] D. Yu. Bardin, P. Ch. Christova and O. M. Fedorenko, *Nucl. Phys.* **B175**(3), 435-461 (1980); *ibid.* **B197**(1), 1-44 (1982).

[10] A. Sirlin, *Phys. Rev. D* **22**(4), 971-981 (1980).

[11] *Topical Conference on Radiative Corrections in* $SU(2) \times U(1)$. Miramare-Trieste, Italy, June 6-8, 1983.

[12] D. Yu. Bardin, *Precision Verifications of the Standard Theory. JINR Lectures for Young Scientists. No. 46* P2-88-189, Dubna:JINR, 1988, pp. 22-23 [in Russian].

[13] V. V. Dvoeglazov, V. I. Kikot' and N. B. Skachkov JINR Communications E2-90-569, E2-90-570, Dubna:JINR, 1990; V.V.Dvoeglazov and N.B.Skachkov, JINR Communications E2-91-114,E2-91-115,E2-91-179, Dubna: JINR, 1991.

[14] G. t' Hooft and M. Veltman, *Nucl. Phys.* **B153**(3-4), 365-401 (1979).

[15] G. Passarino and M. Veltman, *Nucl. Phys.* **B160**(1), 151-207 (1979).

[16] P.N. Maher, L.Durand and K.Riesselmann, *Phys. Rev. D* **48**(3), 1061-1083 (1993); *ibid.* , 1084-1096; L. Durand, J. M. Johnson and J. L. Lopez, *Phys. Rev. D* **45**(9), 3112-3127 (1992); L. Durand, J. M. Johnson and P. N. Maher, *Phys. Rev. D* **44**(1), 127-138 (1991); L. Durand, J. M. Johnson and J. L. Lopez, *Phys. Rev. Lett.* **64**(11), 1215-1218 (1990).

[17] W. Marciano, G. Valencia and S. Willenbrock, *Phys. Rev. D* **40**(5), 1725R (1989); G. E. Vagenakis, Europhysics Lett. **12**, 89 (1990).

[18] B. W. Lee, C. Quigg and M. B. Thacker, *Phys. Rev. Lett.* **38**(16), 883-885 (1977); *Phys. Rev. D* **16**(5), 1519-1531 (1977).

[19] J. Cornwall, D. Levin and G. Ticktopoulos, *Phys. Rev. D* **10**(4), 1145-1167 (1974).

[20] A. A. Logunov and A. N. Tavkhelidze, Nuovo Cimento **29**, 380-399 (1963); V. G. Kadyshevsky, Nucl. Phys. B**62**, 125-148 (1968).

[21] R. Stuart, Comp. Phys. Comm. **48**, 367 (1988); R. Stuart and A. Gognora, ibid. **56**, 337 (1990).

[22] G. t'Hooft, Nucl. Phys. B**33**1, 173-199 (1971); *ibid.* **B35**(1), 167-188 (1971).

[23] H. Georgi, *Hadronic J.* **1**(1), 155-168 (1978).

[24] J. F. Donoghue and Ling-Fong Li, *Phys. Rev. D* **19**(3), 945-955 (1979).

[25] G. C. Branco, A. J. Buras and J.-M. Gerard, *Nucl. Phys.* **B259**(2-3), 306-330 (1985).

[26] H. E. Haber and G. L. Kane, *Phys. Repts.* **117**(2-4), 75-263 (1985).

[27] J. F. Gunion and H. E. Haber, *Nucl. Phys.* **B272**(1), 1-76 (1986); *ibid.* **B278**(3), 449-492 (1986); *ibid.* **B307**(3), 445-475 (1988).

[28] R. D. Peccei and H. R. Quinn, *Phys. Rev. Lett.* **38**(25), 1440-1443 (1977); *Phys. Rev. D* **16**(6), 1791-1797 (1977).

[29] S. L. Glashow and E. E. Jenkins, *Phys. Lett.* **196B**(2), 233-236 (1987); S. Nandi, *Phys. Lett.* **202B**(3), 385-387 (1988).

[30] T. D. Lee, *Phys. Rev. D* **8**(4), 1226-1239 (1973); S. Weinberg, *Phys. Rev. Lett.* **37**(11), 655-661 (1976).

GEODISIC CURVATURES AND NATURAL LIFTS OF SPHERICAL INDICATORS OF TIMELIKE MANNHEIM PAIR CURVES

Süleyman Şenyurt
Faculty of Arts and Sciences
Department of Mathematics, Ordu University
52200, Ordu, Turkey
senyurtsuleyman@hotmail.com

Received November 20, 2014
Revised January 8, 2015

Abstract

In this paper, we take Mannheim curve and Mannheim partner curve with respect to $\mathbb{L}^3$ Lorentz space, S_1^2 Lorentz sphere or H_0^2 Hyperbolic sphere, then we have calculated arc lengths of spherical indicator curves (T^*), (N^*) and (B^*) curves of Mannheim partner curves. We have calculated geodesic curves of them, and also we have figured out some relations among them. In addition, if the natural lifts geodesic spray of spherical indicator curvatures of Mannheim partner curve is an integral curve, then we have expressed how Mannheim Curve is supposed to be.

MSC (2010): 53B30, 53C50
Key word: Lorentz space, Mannheim curve, Geodesic curvatures, Geodesic spray, Natural lift.

Copyright © 2016 by Hadronic Press, Inc., Palm Harbor, FL 34684, USA

1 Introduction

There are lots of researches to be done in 3-dimensional Euclidean space on differential geometry of curves. Especially, many theories were obtained by making connections two curves' mutual points and between Frenet frames. Well known researches are related with Bertrand curves and Involute-Evolute curves, [6] [4], [7], [20]. Those curves were studied carefully in different spaces, therefore, so many results were gained. Bertrand curves' Frenet frames create spherical indicator curves on unit sphere surface in those spherical indicator curves' natural lifts and geodisic sprays are defined in Euclidean and Minkowski space [5], [17], [3], [8].

Mannheim curve was firstly defined by A. Mannheim in 1878. Any curve can be a Mannheim curve if and only if $\kappa = \lambda(\kappa^2 + \tau^2)$, where λ is a nonzero constant κ is the curvature and τ is the torsion. After a time, Mannheim curve was redefined by Liu and Wang. According to this new definition, if the first curve's principal normal vector and the second curve's binormal vector are linearly dependent, the first curve was named as Mannheim curve, and the second curve was named as Mannheim partner curve [22], [10]. There are so many researches done by some mathematicians after Liu and Wang's definition [12], [15], [16], [14].

2 Preliminaries

Let $\alpha : I \to E^3$, $\alpha(t) = (\alpha_1(s), \alpha_2(s), \alpha_3(s))$ be a unit speed differentiable curve. $\{T, N, B\}$ be Frenet frame of $\alpha : I \to E^3$ curve's Frenet as , κ be curvature and τ be torsion. In this position there are some equations among them;

$$\begin{cases} T'(s) = \kappa(s)N(s) \\ N'(s) = -\kappa(s)T(s) + \tau(s)B(s) \\ B'(s) = -\tau(s)N(s). \end{cases} \tag{1}$$

(see [9]). By using (1), we can get W Darboux vector as;

$$W = \tau T + \kappa B \tag{2}$$

If φ is the angle between W and B, then the unit Darboux vector is ;

$$C = \sin\varphi T + \cos\varphi B \tag{3}$$

Let X be a differentiable vector space on M. (Note that M is any vector space)

$$\frac{d}{ds}(\alpha(s)) = X(\alpha(s)) \tag{4}$$

The curve α is an integral curve of X if and only if

$$\frac{d}{ds}(\alpha(s)) = X(\alpha(s)).$$

Suppose that $TM = \bigcup_{P\in M} T_M(P)$ then,

$$\overline{\alpha} : I \to TM, \overline{\alpha}(s) = (\alpha(s), \alpha'(s)) \tag{5}$$

$\overline{\alpha} : I \to TM$ curve is natural lift of $\alpha : I \to M$ and for $v \in TM$

$$X(v) = -\langle v, S(v)\rangle \mathrm{N}|_P$$

X vector space is called geodesic spray (see [5], [20]). Where

$$\overline{D}_X Y = D_X Y + \langle S(X), Y\rangle \mathrm{N} \tag{6}$$

Equation (6) is a Gauss equation on M. $(T), (N)$, (B) spherical indicator curves' equations are given respectively;

$$\begin{cases} \alpha_T(s) = T(s) \\ \alpha_N(s) = N(s) \\ \alpha_B(s) = B(s) \end{cases}$$

With respect to $\mathbb{E}^3$, arc lengths and geodesic curvatures of those curves are given respectively as ;

$$s_T = \int_0^s \kappa ds,\ s_N = \int_0^s \|W\| ds,\ \ s_B = \int_0^s \tau ds,\ \ s_C = \int_0^s \varphi' ds \tag{7}$$

$$\begin{cases} k_T = \dfrac{1}{\cos\varphi}, \\ k_N = \sqrt{1+\left(\frac{\varphi'}{\|W\|}\right)^2}, \\ k_B = \dfrac{1}{\sin\varphi}, \\ k_C = \sqrt{1+\left(\frac{\|W\|}{\varphi'}\right)^2}. \end{cases} \tag{8}$$

With respect to S^2, geodesic curvatures are given by;

$$\gamma_T = \tan\varphi,\ \gamma_N = \frac{\varphi'}{\|W\|},\ \gamma_B = \cot\varphi,\ \gamma_C = \frac{\|W\|}{\varphi'}\ (see[9]). \tag{9}$$

Let $\overline{\alpha} : I \to TM$ be natural lift of $\alpha : I \to M$. X geodesic spray is an integral curve if and only if there is a geodesic curve on M, (see [5]).
Let $\alpha : I \to \mathbb{E}^3$ and $\alpha^* : I \to E^3$ be two differentiable curves. Suppose that Frenet frames on the points of $\alpha(s)$ and $\alpha^*(s)$ are given $\{T(s), N(s), B(s)\}$ and $\{T^*(s), N^*(s), B^*(s)\}$ respectively . If α curve's principal normal vector and α^* curve's binormal vector are linearly dependent, α curve is called Mannheim curve, α^* curve is called Mannheim partner curve, and it is shown as (α, α^*), [22]. Mannheim curve's equation is given as;

$$\alpha^*(s^*) = \alpha(s) - \lambda N(s)\ \ or\ \ \alpha(s) = \alpha^*(s^*) + \lambda B^*(s^*)(see[12]).$$

There exist following equations among these curves:

$$\begin{cases} T = \cos\theta T^* + \sin\theta N^* \\ N = B^* \\ B = -\sin\theta T^* + \cos\theta N^*. \end{cases} \tag{10}$$

$$\cos\theta = \frac{ds^*}{ds},\ \sin\theta = \lambda\tau^*\frac{ds^*}{ds} \tag{11}$$

$$\begin{cases} T^* = \cos\theta T - \sin\theta B \\ N^* = \sin\theta T + \cos\theta B \\ B^* = N. \end{cases} \tag{12}$$

where $\sphericalangle\ (T,T^*)=\theta$, (see [12]). Let κ be curvature of α,τ be torsion of α, and let κ^* be curvature of α^*,τ^* be torsion of α^*. Then, there are following equations;

$$\begin{cases} \kappa = \tau^* \sin\theta \cdot \dfrac{ds^*}{ds} \\ \tau = -\tau^* \cos\theta \cdot \dfrac{ds^*}{ds}. \end{cases} \tag{13}$$

$$\begin{cases} \kappa^* = \dfrac{d\theta}{ds^*} \\ \tau^* = (\kappa \sin\theta - \tau\cos\theta) \cdot \dfrac{ds^*}{ds}, \end{cases} \tag{14}$$

$$\tau^* = \frac{\kappa}{\lambda\tau} \ (see[12]). \tag{15}$$

For $X = (x_1, x_2, x_3)$, $Y = (y_1, y_2, y_3) \in \mathbb{IR}^3$ $g : IR^3 \times IR^3 \to IR$,

$$g(X,Y) = x_1y_1 + x_2y_2 - x_3y_3 \tag{16}$$

This inner product space is defined as Lorentz space and symbolized as $\mathbb{IL}^3$. Norm of the vector $X \in \mathbb{IL}^3$ is $\|X\|_{\mathbb{IL}} = \sqrt{|g(X,X)|}$. For and

$$X \times Y = (x_3y_2 - x_2y_3, x_1y_3 - x_3y_1, x_1y_2 - x_2y_1)$$

$X \times Y$ is called the vector product of X and Y, (see [1]). Let T be tangent vector of $\alpha : I \to \mathbb{IL}^3$. $\alpha : I \to \mathbb{IL}^3$ is respectively defined as;

i) If $g(T,T) > 0$, αcurve is a spacelike curve,

ii) If $g(T,T) < 0$, αcurve is a timelike curve,

iii) If $g(T,T) = 0$, α curve is a lightlike or null curve, (see [11]).

Let $\alpha : I \to \mathbb{IL}^3$ be a differentiable timelike curve. In this case, T is timelike curve, N and B are spacelike curve, and Frenet formulas are given;

$$\begin{cases} T' = \kappa N \\ N' = \kappa T - \tau B \\ B' = \tau N \end{cases} \tag{17}$$

(see [23]), where

$$W = \tau T - \kappa B \tag{18}$$

(see [21]). In this situation, there are two cases for W Darboux vector if W is spacelike curve, the Lorentzian timelike angle φ between $-B$ and W, then;

$$\kappa = \|W\| \cosh\varphi \ , \tau = \|W\| \sinh\varphi \tag{19}$$

And unit Darboux vector is;

$$C = \sinh\varphi T - \cosh\varphi B \tag{20}$$

If W is timelike, κ and τ are formulized;

$$\kappa = \|W\| \sinh\varphi \ , \tau = \|W\| \cosh\varphi \tag{21}$$

The unit Darboux vector is;

$$C = \cosh\varphi T - \sinh\varphi B. \tag{22}$$

Let M be a Lorentz manifold, and $\overline{M}$ be a hypersurface of M. Suppose that S is a shape operator which is obtained from N normal of $\overline{M}$, D is the connection on M, $\bar{D}$ is the connection on $\overline{M}$, For $X, Y \in \chi(\overline{M})$, Gauss equation is;

$$D_X Y = \bar{D}_X Y + \varepsilon g(S(X), Y)N \tag{23}$$

where $S(X) = -D_X N$ and $\varepsilon = g(N, N)$, (see [19]).

$$S_1^2(r) = \left\{ X \in IR_1^3 \middle| \, g(X, X) = r^2, \ r \in IR \right\}$$

is defined as Lorentz sphere,

$$H_0^2(r) = \left\{ X \in IR_1^3 \middle| \, g(X, X) = -r^2, \ r \in IR \right\}$$

is defined as hyperbolic sphere.

3 Timelike Mannheim Curve Pairs.

Definition 3.1: Let $\alpha : I \to \mathbb{IL}^3$ and $\alpha^* : I \to \mathbb{IL}^3$ be a timelike curve. Suppose that Frenet frames of α on the point of $\alpha(s)$ is $\{T(s), N(s), B(s)\}$ and Frenet frames of α^* on the point of $\alpha^*(s)$ is $\{T^*(s), N^*(s), B^*(s)\}$. If principal normal vector of α^* and binormal vector of α^* are linearly dependent, then the curve α is called Mannheim curve and the curve α^* is called Mannheim partner curve. This pair curve is briefly symbolized as (α, α^*) and it is named timelike Mannheim curve pairs.

Theorem 3.1: The distance between (α, α^*) timelike Mannheim curve pair is constant.

Proof: It can be written that; $\alpha(s) = \alpha^*(s^*) + \lambda(s^*)B^*(s^*)$. If this equation is derived with respect to s^* parameter, we can write;

$$T\frac{ds}{ds^*} = T^* + \lambda\tau^* N^* + \lambda' B^*$$

If we get inner product of the last equation and B^*, then $\lambda' = 0$. From the definition of Euclidean distance, we can write;

$$\begin{aligned} d(\alpha^*(s^*), \alpha(s)) &= \|\alpha(s) - \alpha^*(s^*)\| \\ &= |\lambda| = \text{constant} \end{aligned}$$

Theorem 3.2: Let (α, α^*) be a timelike Mannheim curve pair. Suppose that α curve's and α^* curve's Frenet frames of curves α and α^* are $\{T, N, B\}$ and $\{T^*, N^*, B^*\}$ respectively . In this case, there are following equations;

$$\begin{cases} T^* = -\cosh\theta T + \sinh\theta B \\ N^* = \sinh\theta T - \cosh\theta B \\ B^* = N \end{cases} \tag{24}$$

$$-\cosh\theta = \frac{ds^*}{ds}, \quad \sinh\theta = \lambda\tau^*\frac{ds^*}{ds} \tag{25}$$

$$\begin{cases} T = -\cosh\theta T^* - \sinh\theta N^* \\ N = B^* \\ B = -\sinh\theta T^* - \cosh\theta N^*. \end{cases} \tag{26}$$

Proof: If we derive $\alpha^*(s^*) = \alpha(s) - \lambda N(s)$ with respect to the parameter s, we can write;

$$T^* \frac{ds^*}{ds} = (1 - \lambda\kappa)T(s) + \lambda\tau B \tag{27}$$

If we take inner product of (27) and T, then;

$$-\cosh\theta \frac{ds^*}{ds} = 1 - \lambda\kappa, \tag{28}$$

If we take inner product of (27) and B, then;

$$\sinh\theta \frac{ds^*}{ds} = \lambda\tau \tag{29}$$

If (28) and (29) are plugged into (27), we can write;

$$T^* = -\cosh\theta T + \sinh\theta B$$

From Frenet formulas, the following equations can be found;

$$N^* = \sinh\theta T - \cosh\theta B,$$

$$B^* = N.$$

Obviously, we have shown the equation (24). If we arrange this equation with respect to T and B, then we can find the equation of (26). If $\alpha(s) = \alpha^*(s^*) + \lambda B^*(s^*)$ is derived with respect to the parameter s , it can be found ;

$$T = T^* \frac{ds^*}{ds} + \lambda\tau^* \frac{ds^*}{ds} N^*$$

If we consider the corresponding value of T from the equation (26), equation (25) is proven.

Theorem 3.3: Let (α, α^*) be a timelike Mannheim curve pair. Let κ be curvature of α, and let τ be torsion of α. In this case, we have the following equation

$$\lambda\kappa + \mu\tau = 1$$

Proof: If we divide (28) to (29), we can write;

$$-\tanh\theta = \frac{\lambda\kappa - 1}{\lambda\tau}$$

If we get $\mu = \lambda \tanh\theta$, the result is proven.

Theorem 3.4: Let (α, α^*)be a timelike Mannheim curve pair. In this case, there are following equations among curvatures;

$$\kappa = \tau^* \sinh\theta \frac{ds^*}{ds}, \ \tau = \tau^* \cosh\theta \frac{ds^*}{ds}, \tag{30}$$

$$\kappa^* = -\frac{d\theta}{ds^*} = -\theta' \frac{ds}{ds^*}, \ \tau^* = \kappa \sinh\theta \frac{ds}{ds^*} - \tau \cosh\theta \frac{ds}{ds^*}. \tag{31}$$

Proof: If we differentiate $\langle T, B^* \rangle = 0$, then $\kappa = \tau^* \sinh\theta \frac{ds^*}{ds}$,

If we differentiate $\langle B, B^* \rangle = 0$, then $\tau = \tau^* \cosh\theta \frac{ds^*}{ds}$,

If we differentiate $\langle T, T^* \rangle = \sinh\theta$, then $\kappa^* = -\frac{d\theta}{ds^*} = -\theta' \frac{ds}{ds^*}$,

If we differentiate $\langle N, N^* \rangle = 0$, then $\tau^* = \kappa \sinh\theta \frac{ds}{ds^*} - \tau \cosh\theta \frac{ds}{ds^*}$.

Therefore, the result is proven.

Theorem 3.5: Let (α, α^*) be a timelike Mannheim curve pair. Let κ^* be curvature of α^*, τ^*be torsion of α^* and τ be torsion of α. Then the following equation holds;

$$\tau^* = \frac{\kappa}{\lambda\tau}. \tag{32}$$

Proof: If we take equations from (25) and if we multiply side by side (28) and (28), then the result is proven.

Theorem 3.6: Let (α, α^*) be a timelike Mannheim curve pair. Then the following equation holds between W Darboux vector of the curve α and T^* tangent vector of the curve α^*;

$$W = -\tau^* \frac{ds^*}{ds} T^* \tag{33}$$

Proof: We know that $W = \tau T - \kappa B$. If we take the corresponding values of T and B from (26), and then if we plug into those values in (33), Then, if we get the corresponding values of κ and τ from (30), and then if we plug into those values in (33), the result is proven.

Result 3.1: Let (α, α^*) be a timelike Mannheim curve pair. Let φ be the angle between Darboux vector of the curve α and binormal vector of the α. Then the following equation occurs between θ and φ

$$\cosh\varphi = \cosh\theta \ , \ \sinh\varphi = -\sinh\theta. \tag{34}$$

Proof: W is a timelike vector from (33). we can write from equation (22);

$$C = \cosh\varphi T - \sin h\varphi B$$

If we consider $C = T^*$, we can write;

$$\begin{cases} \cos h\varphi = -\sinh\theta \\ -\sin h\varphi = \cosh\theta. \end{cases}$$

Theorem 3.7: Let (α, α^*) be a timelike Mannheim curve pair. Then the following equation holds between W Darboux vector of the curve α and W^* Darboux vector of the curve α^*

$$W^* = \frac{1}{\cosh\theta}W - \frac{\theta'\kappa}{\lambda\kappa\|W\|}N. \tag{35}$$

Proof: It can be written $\tau^*T^* = -W^* + \kappa^*B^*$ because α^* Manheim partner curve's W^* vector is spacelike. If this equation is plugged into (33), and if we consider that B^*= N, then the following equation holds.

$$W = -\frac{ds^*}{ds}(W^* + \kappa^*N)$$

If the corresponding value of $\frac{ds}{ds^*}$ from (25) is written in this equation, then;

$$W^* = \frac{1}{\cosh\theta}W - \kappa^*N$$

On the other hand, from equation (30), we can write that $\frac{ds}{ds^*} = \frac{\tau^*}{\|W\|}$. If the corresponding value of τ^* in (32) is written in this equation, then;

$\frac{ds}{ds^*} = \frac{-\kappa}{\lambda\tau \|W\|}$. If we plug this equation into $\kappa^* = \theta' \frac{ds}{ds^*}$, the following equation holds.

$$\kappa^* = -\theta' \frac{\kappa}{\lambda\tau \|W\|} \tag{36}$$

If we write this value of κ^* in(38), the result is proven.
Let s_T be $\alpha : I \to \mathbb{IL}^3$ timelike Mannheim curve's (T) tangent indicator's, k_T be (T) tangent indicator's geodesic cuvature on $\mathbb{IL}^3$. Suppose that T_T a unit tangent vector of (T), then;

$$k_T = \|D_{T_T} T_T\| .$$

If $\alpha_T(s) = T(s)$ tangent indicator is derived with respect to s_T the parameter, we can write;

$$T_T = N \tag{37}$$

If we derive one more time and simplify the equation, the following equation holds.

$$D_{T_T} T_T = T - \frac{\tau}{\kappa} B \tag{38}$$

From the definition of geodesic curvature;

$$k_T = \sqrt{\left| -1 + \frac{\tau^2}{\kappa^2} \right|} \tag{39}$$

If we consider equations (19), (21) and (34), we can write;

$$\begin{cases} k_T = \dfrac{1}{\cosh\theta} & ,W \text{ spacelike} \\ k_T = \dfrac{1}{\sinh\theta} & ,W \text{ timelike} \end{cases} . \tag{40}$$

Similarly, if $\alpha_N(s) = N(s)$ principal normal indicator is derived with respect to s_N the parameter, from equations (19), (21) and (34)

$$\begin{cases} T_N = \cosh\theta T - \sinh\theta B & ,W \text{ spacelike} \\ T_N = \sinh\theta T - \cosh\theta B & ,W \text{ timelike} \end{cases} . \tag{41}$$

If we derive one more time, the following equation holds.

$$\begin{cases} D_{T_N}T_N = \dfrac{\theta'}{\|W\|}\left(\sinh\theta T - \cosh\theta B\right) + N & ,W \text{ spacelike} \\ D_{T_N}T_N = \dfrac{\theta'}{\|W\|}\left(\cosh\theta T - \sinh\theta B\right) - N & ,W \text{ timelike} \end{cases} . \tag{42}$$

From the definition of geodesic curvature;

$$\begin{cases} k_N = \sqrt{\left|1 + \left(\dfrac{\theta'}{\|W\|}\right)^2\right|} & ,W \text{ spacelike} \\ k_N = \sqrt{\left|1 - \left(\dfrac{\theta'}{\|W\|}\right)^2\right|} & ,W \text{ timelike} \end{cases} . \tag{43}$$

If $\alpha_B(s) = B(s)$ binormal indicator is derived with respect to s_B the parameter, and if we chose the positive routing then;

$$D_{T_B}T_B = \frac{\kappa}{\tau}T - B. \tag{44}$$

From the definition of geodesic curvature

$$k_B = \sqrt{\left|1 - \frac{\kappa^2}{\tau^2}\right|} \tag{45}$$

And also from equation (19), (21) and (34)

$$\begin{cases} k_B = \dfrac{1}{\sinh\theta} & ,W \text{ spacelike} \\ k_B = \dfrac{1}{\cosh\theta} & ,W \text{ timelike} \end{cases} . \tag{46}$$

Result 3.2: Let (α, α^*) be a timelike Mannheim curve pair. α Mannheim curve's spherical indicators are $(T), (N)$ and (B), with respect to $\mathbb{IL}^3$, geodesic curvatures of $(T), (N)$ and (B) are respectively;

$$\begin{cases} k_T = \frac{1}{\cosh\theta} & ,W \text{ spacelike} \\ k_T = \frac{1}{\sinh\theta} & ,W \text{ timelike} \end{cases} ,$$

$$\begin{cases} k_N = \sqrt{\left|1+\left(\frac{\theta'}{\|W\|}\right)^2\right|} & ,W \text{ spacelike} \\ k_N = \sqrt{\left|1-\left(\frac{\theta'}{\|W\|}\right)^2\right|} & ,W \text{ timelike} \end{cases},$$

$$\begin{cases} k_B = \frac{1}{\sinh\theta} & ,W \text{ spacelike} \\ k_B = \frac{1}{\cosh\theta} & ,W \text{ timelike} \end{cases},$$

Let D be $\alpha : I \to \mathbb{IL}^3$ Mannheim curve's connection on $\mathbb{IL}^3$, let $\bar{D}$ be $\alpha : I \to \mathbb{IL}^3$ Mannheim curve's connection on S_1^2, and let $\bar{\bar{D}}$ be $\alpha : I \to \mathbb{IL}^3$ Mannheim curve's connection on H_0^2.Suppose that ξ is unit normal vector space of $S_1^2$and H_0^2, then;

$$D_X Y = \bar{D}_X Y + \varepsilon g(S(X), Y)\xi, \qquad \varepsilon = g(\xi, \xi)$$

$$D_X Y = \bar{\bar{D}}_X Y + \varepsilon g(S(X), Y)\xi, \qquad \varepsilon = g(\xi, \xi).$$

where S is shape operator of S_1^2 and H_0^2, and corresponding matrix is;

$$S = \begin{bmatrix} -1 & 0 \\ 0 & -1 \end{bmatrix}$$

(see [6]). Let γ_T be (T) tangent indicator's geodesic curvature on H_0^2, then;

$$\gamma_T = \left\|\bar{\bar{D}}_{T_T} T_T\right\|$$

From Gauss equation, we can write;

$$D_{T_T} T_T = \bar{\bar{D}}_{T_T} T_T + \varepsilon g(S(T_T), T_T) T$$

where

$$\varepsilon = g(T, T) = -1, \quad S(T_T) = -T_T, \text{ and } g(S(T_T), T_T) = -1$$

If we write those values in Gauss equation, and if we consider (38), we can write;

$$\bar{\bar{D}}_{T_T} T_T = -\frac{\tau}{\kappa} B \tag{47}$$

And also from equation (19), (21) and (34)

$$\begin{cases} \gamma_T = \tanh\theta & ,W \text{ spacelike} \\ \gamma_T = \coth\theta & ,W \text{ timelike} \end{cases} \tag{48}$$

Similarly, let γ_N be geodesic curvature of (N) principal normal indicator on S_1^2, then; from Gauss equation, we can write;

$$\begin{cases} \bar{D}_{T_N} T_N = \dfrac{\theta'}{\|W\|}(\sinh\theta T - \cosh\theta B) & ,T_N \text{ spacelike} \\ \bar{D}_{T_N} T_N = \dfrac{\theta'}{\|W\|}(\cosh\theta T - \sinh\theta B) & ,T_N \text{ timelike} \end{cases} \tag{49}$$

and

$$\gamma_N = \frac{\theta'}{\|W\|}. \tag{50}$$

Let γ_B be geodesic curvature of (B) binormal indicator on S_1^2, then; from Gauss equation and if we consider (44), we can write;

$$\bar{D}_{T_B} T_B = \frac{\kappa}{\tau} T \tag{51}$$

From equation (19), (21) and (34) it can be written;

$$\begin{cases} \gamma_B = \coth\theta & ,W \text{ spacelike} \\ \gamma_B = \tanh\theta & ,W \text{ timelike} \end{cases} \tag{52}$$

Result 3.3: Let (α, α^*) be a timelike Mannheim curve pair. α Mannheim curve's spherical indicators are $(T), (N)$ and (B), with respect to S_1^2 Lorentz sphere or H_0^2 hyperbolic sphere, geodesic curvatures of $(T), (N)$ and (B) are respectively;

$$\begin{cases} \gamma_T = \tanh\theta & ,W \text{ spacelike} \\ \gamma_T = \coth\theta & ,W \text{ timelike} \end{cases}$$

$$\gamma_N = \frac{\theta'}{\|W\|},$$

$$\begin{cases} \gamma_B = \coth\theta & ,W \text{ spacelike} \\ \gamma_B = \tanh\theta & ,W \text{ timelike} \end{cases}$$

Let $\alpha^* : I \to \mathbb{IL}^3$ be timelike Mannheim partner curve, and let s_{T^*} be Mannheim partner curve's (T^*) tangent indicator's arc length, then;

$$\begin{cases} s_{T^*} = \int_0^s \sqrt{(\theta')^2 + \|W\|^2}\, ds & ,W \text{ spacelike} \\ s_{T^*} = \int_0^s \theta' ds & ,W \text{ timelike} \end{cases} \tag{53}$$

Similarly, arc lengths of (N^*) and (B^*) are found as;

$$\begin{cases} s_{N^*} = \int_0^s \theta' ds & ,W \text{ spacelike} \\ s_{N^*} = \int_0^s \sqrt{\left|-(\theta')^2 + \|W\|^2\right|}\, ds & ,W \text{ timelike} \end{cases} \tag{54}$$

$$s_{B^*} = \int_0^s \|W\|\, ds \tag{55}$$

Result 3.4: Let (α, α^*) be a timelike Mannheim curve pair. The arc lengths of spherical indicator of Frenet vector of α^* Mannheim partner curve in terms of $\mathbb{IL}^3$ are

$$\begin{cases} s_{T^*} = \int_0^s \sqrt{(\theta')^2 + \|W\|^2}\, ds & ,W \text{ spacelike} \\ s_{T^*} = \int_0^s \theta' ds & ,W \text{ timelike} \end{cases}$$

$$\begin{cases} s_{N^*} = \int_0^s \theta' ds & ,W \text{ spacelike} \\ s_{N^*} = \int_0^s \sqrt{\left|-(\theta')^2 + \|W\|^2\right|}\, ds & ,W \text{ timelike} \end{cases}$$

$$s_{B^*} = \int_0^s \|W\|\, ds \ .$$

Let k_{T^*} be geodesic curvature of tangent indicator $\alpha^*_{T^*}(s) = T^*(s)$, let s_{T^*} be arc parameter, and let T_{T^*} be unit tangent vector. Then, we can say;

$$\begin{cases} T_{T^*} = \dfrac{\sinh\theta T - \cosh\theta B}{\sqrt{1 + \left(\frac{\|W\|}{\theta'}\right)^2}} - \dfrac{N}{\sqrt{1 + \left(\frac{\theta'}{\|W\|}\right)^2}} & ,W \text{ spacelike} \\ T_{T^*} = -\sinh\theta T + \cosh\theta B & ,W \text{ timelike} \end{cases} \tag{56}$$

or from equation (8) (34) and (43)

$$\begin{cases} T_{T^*} = \dfrac{1}{k_C}\left(\sinh\theta T - \cosh\theta B\right) - \dfrac{1}{k_N}N & ,W \text{ spacelike} \\ T_{T^*} = -\sinh\theta T + \cosh\theta B & ,W \text{ timelike,} \end{cases} \tag{57}$$

$$\begin{cases} D_{T_{T^*}}T_{T^*} = \left[\dfrac{\left(\frac{\sinh\theta}{k_C}\right)' - \left(\frac{\kappa}{k_N}\right)}{\sqrt{(\theta')^2+\|W\|^2}}\right]T + \left[\dfrac{-\left(\frac{1}{k_N}\right)' + \kappa\left(\frac{\sinh\theta}{k_C}\right) - \tau\left(\frac{\cosh\theta}{k_C}\right)}{\sqrt{(\theta')^2+\|W\|^2}}\right]N \\ \qquad + \left[\dfrac{-\left(\frac{\cosh\theta}{k_C}\right)' + \frac{\tau}{k_N}}{\sqrt{(\theta')^2+\|W\|^2}}\right]B \qquad ,W \text{ spacelike} \\ D_{T_{T^*}}T_{T^*} = -\cosh\theta T + \sinh\theta B - \dfrac{\|W\|}{\theta'}N \quad ,W \text{ timelike} \end{cases} \tag{58}$$

If we get norm of (58), we can write that

$$\begin{cases} k_{T^*} = \left\{ \left| \dfrac{-\left[\left(\frac{\sinh\theta}{k_C}\right)' - \left(\frac{\kappa}{k_N}\right)\right]^2 + \left[-\left(\frac{1}{k_N}\right)' + \kappa\left(\frac{\sinh\theta}{k_C}\right) - \tau\left(\frac{\cosh\theta}{k_C}\right)\right]^2}{(\theta')^2+\|W\|^2} \right. \right. \\ \qquad \left. \left. + \dfrac{\left[-\left(\frac{\cosh\theta}{k_C}\right)' + \frac{\tau}{k_N}\right]^2}{(\theta')^2+\|W\|^2} \right| \right\}^{\frac{1}{2}} \quad ,W \text{ spacelike} \\ k_{T^*} = \sqrt{\left|\left(\dfrac{\|W\|}{\theta'}\right)^2 - 1\right|} \qquad ,W \text{ timelike} \end{cases} \tag{59}$$

Similarly, let k_{N^*} be geodesic curvature principal normal indicator $\alpha^*_{N^*}(s) = N^*(s)$ in terms of $\mathbb{III}^3$, let s_{N^*} be arc parameter, and let T_{N^*} be unit tangent vector. Then, we can say;

$$\begin{cases} T_{N^*} = \cosh\theta T - \sinh\theta B & ,W \text{ spacelike} \\ T_{N^*} = \dfrac{\sinh\theta T - \cosh\theta B}{\sqrt{1+\left(\frac{\|W\|}{\theta'}\right)^2}} - \dfrac{N}{\sqrt{1+\left(\frac{\|W\|}{\theta'}\right)^2}} & ,W \text{ timelike} \end{cases} \tag{60}$$

from equation (8) (34) and (43)

$$\begin{cases} T_{N^*} = \cosh\theta T - \sinh\theta B & ,W \text{ spacelike} \\ T_{N^*} = \dfrac{1}{k_C}(\sinh\theta T - \cosh\theta B) - \dfrac{1}{k_N}N & ,W \text{ timelike,} \end{cases} \tag{61}$$

$$\begin{cases} D_{T_{N^*}}T_{N^*} = \sinh\theta T - \cosh\theta B + \frac{\|W\|}{\theta'}N & ,W \text{ spacelike} \\ D_{T_{N^*}}T_{N^*} = \left[\dfrac{\left(\frac{\sinh\theta}{k_C}\right)' - \left(\frac{\kappa}{k_N}\right)}{\sqrt{(\theta')^2+\|W\|^2}}\right]T + \left[\dfrac{-\left(\frac{1}{k_N}\right)' + \kappa\left(\frac{\sinh\theta}{k_C}\right) - \tau\left(\frac{\cosh\theta}{k_C}\right)}{\sqrt{(\theta')^2+\|W\|^2}}\right]N \\ \qquad + \left[\dfrac{-\left(\frac{\cosh\theta}{k_C}\right)' + \frac{\tau}{k_N}}{\sqrt{(\theta')^2+\|W\|^2}}\right]B \qquad ,W \text{ timelike} \end{cases} \tag{62}$$

If we get norm of (62), we can write that

$$\begin{cases} k_{N^*} = \sqrt{1+\left(\frac{\|W\|}{\theta'}\right)^2} & ,W \text{ spacelike} \\ k_{N^*} = \left\{\left| \dfrac{\left[\left(\frac{-\sinh\theta}{k_C}\right)' + \left(\frac{\kappa}{k_N}\right)\right]^2 + \left[-\left(\frac{1}{k_N}\right)' + \kappa\left(\frac{\sinh\theta}{k_C}\right) - \tau\left(\frac{\cosh\theta}{k_C}\right)\right]^2}{(\theta')^2+\|W\|^2} \right.\right. \\ \qquad \left.\left. + \dfrac{\left[\left(\frac{\cosh\theta}{k_C}\right)' - \frac{\tau}{k_N}\right]^2}{(\theta')^2+\|W\|^2} \right|\right\}^{\frac{1}{2}} \quad ,W \text{ timelike} \end{cases} \tag{63}$$

Let k_{B^*} be geodesic curvature binormal indicator $\alpha^*_{B^*}(s) = B^*(s)$ in terms of $\mathbb{IL}^3$, let s_{B^*} be arc parameter, and let T_{B^*}be unit tangent vector. Then, we can say;

$$T_{B^*} = \frac{\kappa}{\|W\|}T - \frac{\tau}{\|W\|}B \tag{64}$$

From equation (21) and (34) it can be written;

$$\begin{cases} T_{B^*} = \cosh\theta T - \sinh\theta B & ,W \text{ spacelike} \\ T_{B^*} = \sinh\theta T - \cosh\theta B & ,W \text{ timelike} \end{cases}$$

$$\begin{cases} D_{T_{B^*}} T_{B^*} = \dfrac{\theta'}{\|W\|}(\sinh\theta T - \cosh\theta B) + N & ,W \text{ spacelike} \\ D_{T_{B^*}} T_{B^*} = \dfrac{\theta'}{\|W\|}(\cosh\theta T - \sinh\theta B) - N & ,W \text{ timelike} \end{cases} \tag{65}$$

If we get norm of (66), we can write that

$$\begin{cases} k_{B^*} = \sqrt{1 + \left(\dfrac{\theta'}{\|W\|}\right)^2} & ,W \text{ spacelike} \\ k_{B^*} = \sqrt{\left|-1 + \left(\dfrac{\theta'}{\|W\|}\right)^2\right|} & ,W \text{ timelike} \end{cases} \tag{66}$$

Result 3.5: Let (α, α^*) be a timelike Mannheim curve pair. The geodesic curvatures of spherical indicator curves $(T^*), (N^*)$ and (B^*) of curve α^* in terms of $\mathbb{IL}^3$, are

$$\begin{cases} k_{T^*} = \left\{ \left| \begin{array}{l} -\dfrac{\left[\left(\frac{\sinh\theta}{k_C}\right)' - \left(\frac{\kappa}{k_N}\right)\right]^2 + \left[-\left(\frac{1}{k_N}\right)' + \kappa\left(\frac{\sinh\theta}{k_C}\right) - \tau\left(\frac{\cosh\theta}{k_C}\right)\right]^2}{(\theta')^2 + \|W\|^2} \\ +\dfrac{\left[-\left(\frac{\cosh\theta}{k_C}\right)' + \frac{\tau}{k_N}\right]^2}{(\theta')^2 + \|W\|^2} \end{array} \right| \right\}^{\frac{1}{2}} & ,W \text{ spacelike} \\ k_{T^*} = \sqrt{\left|\left(\dfrac{\|W\|}{\theta'}\right)^2 - 1\right|} & ,W \text{ timelike} \end{cases},$$

$$\begin{cases} k_{N^*} = \sqrt{1 + \left(\dfrac{\|W\|}{\theta'}\right)^2} & ,W \text{ spacelike} \\ k_{N^*} = \left\{ \left| \begin{array}{l} \dfrac{\left[\left(\frac{-\sinh\theta}{k_C}\right)' + \left(\frac{\kappa}{k_N}\right)\right]^2 + \left[-\left(\frac{1}{k_N}\right)' + \kappa\left(\frac{\sinh\theta}{k_C}\right) - \tau\left(\frac{\cosh\theta}{k_C}\right)\right]^2}{(\theta')^2 + \|W\|^2} \\ +\dfrac{\left[\left(\frac{\cosh\theta}{k_C}\right)' - \frac{\tau}{k_N}\right]^2}{(\theta')^2 + \|W\|^2} \end{array} \right| \right\}^{\frac{1}{2}} & ,W \text{ timelike} \end{cases},$$

$$\begin{cases} k_{B^*} = \sqrt{1 + \left(\dfrac{\theta'}{\|W\|}\right)^2} & ,W \text{ spacelike} \\ k_{B^*} = \sqrt{\left|-1 + \left(\dfrac{\theta'}{\|W\|}\right)^2\right|} & ,W \text{ timelike} \end{cases}$$

Let γ_{T^*} be $\alpha^* : I \to \mathbb{IL}^3$ timelike Mannheim partner curve $\alpha^*_{T^*}(s) = T^*(s)$ tangent indicator's geodesic curvature in S^2_1. Then; from Gauss equation, we can write;

$$D_{T_{T^*}} T_{T^*} = \bar{D}_{T_{T^*}} T_{T^*} + \varepsilon g(S(T_{T^*}), T_{T^*}) T^*$$

Where

$$\varepsilon = g(T^*, T^*) = -1,\ S(T_{T^*}) = -T_{T^*}$$

and

$$\begin{cases} g(S(T_{T^*}), T_{T^*}) = -\left(\dfrac{1}{k_C^2} + \dfrac{1}{k_N^2}\right) & ,W \text{ spacelike} \\ g(S(T_{T^*}), T_{T^*}) = 1 & ,W \text{ timelike.} \end{cases}$$

If those values are written in Gauss equation, (24) and (58)

$$\begin{cases} \bar{D}_{T_{T^*}} T_{T^*} = \left[\dfrac{\left(\frac{\sinh\theta}{k_C}\right)' - \left(\frac{\kappa}{k_N}\right)}{\sqrt{(\theta')^2 + \|W\|^2}} + \dfrac{\cosh\theta}{k_C^2} - \dfrac{\cosh\theta}{k_N^2}\right] T + \left[\dfrac{-\left(\frac{1}{k_N}\right)' + \kappa\left(\frac{\sinh\theta}{k_C}\right) - \tau\left(\frac{\cosh\theta}{k_C}\right)}{\sqrt{(\theta')^2 + \|W\|^2}}\right] N \\ \qquad + \left[\dfrac{-\left(\frac{\cosh\theta}{k_C}\right)' + \frac{\tau}{k_N}}{\sqrt{(\theta')^2 + \|W\|^2}} - \dfrac{\sinh\theta}{k_C^2} - \dfrac{\sinh\theta}{k_N^2}\right] B \quad ,W \text{ spacelike} \\ \bar{D}_{T_{T^*}} T_{T^*} = -\dfrac{\|W\|}{\theta'} \quad ,W \text{ timelike} \end{cases} \tag{67}$$

$$\begin{cases} \gamma_{T^*} = \left\{ \left[\dfrac{\left(\frac{\sinh\theta}{k_C}\right)' - \left(\frac{\kappa}{k_N}\right)}{\sqrt{(\theta')^2 + \|W\|^2}} + \dfrac{\cosh\theta}{k_C^2} - \dfrac{\cosh\theta}{k_N^2}\right]^2 + \left[\dfrac{-\left(\frac{1}{k_N}\right)' + \kappa\left(\frac{\sinh\theta}{k_C}\right) - \tau\left(\frac{\cosh\theta}{k_C}\right)}{\sqrt{(\theta')^2 + \|W\|^2}}\right]^2 \right. \\ \qquad \left. + \left[\dfrac{-\left(\frac{\cosh\theta}{k_C}\right)' + \frac{\tau}{k_N}}{\sqrt{(\theta')^2 + \|W\|^2}} - \dfrac{\sinh\theta}{k_C^2} - \dfrac{\sinh\theta}{k_N^2}\right]^2 \right\}^{\frac{1}{2}} \\ \gamma_{T^*} = \dfrac{\|W\|}{\theta'} \quad ,W \text{ timelike} \end{cases} \tag{68}$$

The curve $(\overline{T^*})$ is an integral curve of geodesic spray if and only if $\overline{D}_{T_{T^*}} T_{T^*} = 0$. From equation (68), we find $\kappa = 0, \tau = 0$. Therefore, the curve α is a straight line.

Result 3.6: α Mannheim curve does not have any partner curve because α Mannheim curve is a straight line.

Let γ_{N^*} be geodesic indicator in H_0^2 for $\alpha^*_{N^*}(s) = N^*(s)$ principal normal indicator. From Gauss equation, it can be written;

$$D_{T_{N^*}} T_{N^*} = \bar{D}_{T_{N^*}} T_{N^*} + \varepsilon g(S(T_{N^*}), T_{N*}) N^*$$

where

$$\varepsilon = g(N^*, N^*) = +1,\ S(T_{N^*}) = -T_{N^*}$$

ve

$$\begin{cases} \mathrm{g}(S(T_{N^*}), T_{N^*}) = 1 & ,W \text{ spacelike} \\ \mathrm{g}(S(T_{N^*}), T_{N^*}) = -\left(\dfrac{1}{k_C^2} + \dfrac{1}{k_N^2}\right) & ,W \text{ timelike.} \end{cases}$$

If those values are written in Gauss equation, and if equations (24) and (62) are considered, we can say;

$$\begin{cases} \bar{D}_{T_{N^*}} T_{N^*} = \dfrac{\|W\|}{\theta'} N \quad ,W \text{ spacelike} \\ \bar{D}_{T_{N^*}} T_{N^*} = \left[\dfrac{\left(\frac{\sinh\theta}{k_C}\right)' - \left(\frac{\kappa}{k_N}\right)}{\sqrt{(\theta')^2 + \|W\|^2}} + \dfrac{\sinh\theta}{k_C^2} + \dfrac{\sinh\theta}{k_N^2}\right] T + \left[\dfrac{-\left(\frac{1}{k_N}\right)' + \kappa\left(\frac{\sinh\theta}{k_C}\right) - \tau\left(\frac{\cosh\theta}{k_C}\right)}{\sqrt{(\theta')^2 + \|W\|^2}}\right] N \\ \qquad + \left[\dfrac{-\left(\frac{\cosh\theta}{k_C}\right)' + \frac{\tau}{k_N}}{\sqrt{(\theta')^2 + \|W\|^2}} - \dfrac{\cosh\theta}{k_C^2} - \dfrac{\cosh\theta}{k_N^2}\right] B \quad ,W \text{ timelike} \end{cases} \tag{69}$$

$$\begin{cases} \gamma_{N^*} = \frac{\|W\|}{\theta'} & ,W \text{ spacelike} \\ \gamma_{N^*} = \left\{ \left[\frac{\left(\frac{\sinh\theta}{k_C}\right)' - \left(\frac{\kappa}{k_N}\right)}{\sqrt{(\theta')^2+\|W\|^2}} + \frac{\sinh\theta}{k_C^2} + \frac{\sinh\theta}{k_N^2} \right]^2 + \left[\frac{-\left(\frac{1}{k_N}\right)' + \kappa\left(\frac{\sinh\theta}{k_C}\right) - \tau\left(\frac{\cosh\theta}{k_C}\right)}{\sqrt{(\theta')^2+\|W\|^2}} \right]^2 \right. \\ \left. + \left[\frac{-\left(\frac{\cosh\theta}{k_C}\right)' + \frac{\tau}{k_N}}{\sqrt{(\theta')^2+\|W\|^2}} - \frac{\cosh\theta}{k_C^2} - \frac{\cosh\theta}{k_N^2} \right]^2 \right\}^{\frac{1}{2}} & ,W \text{ timelike} \end{cases} \tag{70}$$

The curve $(\overline{N^*})$ is an integral curve of geodesic spray if and only if $\overline{D}_{T_{N^*}} T_{N^*} = 0$. If W is spacelike, then , we have $\kappa = 0, \tau = 0$.Therefore, the curve α is a straight line.

Result 3.7: When Darboux vector of Mannheim curve is timelike, this Mannheim curve is a straight line. Therefore , there is no Mannheim partner curve .

Let γ_{B^*} be geodesic curve in S_1^2 for $\alpha^*_{B^*}(s) = B^*(s)$ binormal indicator. From Gauss equation, it can be written;

$$D_{T_{B^*}} T_{B^*} = \bar{\bar{D}}_{T_{B^*}} T_{B^*} + \varepsilon g(S(T_{B^*}), T_{B*}) B^*$$

where

$$\varepsilon = g(B^*, B^*) = 1, \; S(T_{B^*}) = -T_{B^*}$$

ve

$$\begin{cases} g(S(T_{B^*}), T_{B^*}) = 1 & ,W \text{ spacelike} \\ g(S(T_{B^*}), T_{B^*}) = -1 & ,W \text{ timelike} \end{cases}$$

If these values are written in Gauss equation, then, $B^* = N$ and if equation (66) is considered, we can say ;

$$\begin{cases} \overline{\overline{D}}_{T_{B^*}} T_{B^*} = \frac{\theta'}{\|W\|}(\sinh\theta T - \cosh\theta B) & ,W \text{ spacelike} \\ \overline{\overline{D}}_{T_{B^*}} T_{B^*} = \frac{\theta'}{\|W\|}(\cosh\theta T - \sinh\theta B) & ,W \text{ timelike} \end{cases} \tag{71}$$

If we get norm of (71), we can write;

$$\gamma_{B^*} = \mp \frac{\theta'}{\|W\|} \tag{72}$$

The curve $(\overline{B^*})$ is an integral curve of geodesic spray if and only if $\bar{\bar{D}}_{T_{B^*}} T_{B^*} = 0$. In this case, from equation (71), we can write;

$$\begin{cases} \frac{-\theta' \sinh\theta}{\|W\|} = 0, \\ \\ \frac{\theta' \cosh\theta}{\|W\|} = 0 \end{cases}$$

where $\theta' = 0$. In this case, from equations (36) and (19) $\frac{\kappa}{\tau}$ = constant. This means α Mannheim curve is a helix.

Result 3.8: Let (α, α^*) be a timelike Mannheim curve pair. If α Mannheim curve is a helix, Mannheim partner curve of α is a straight line.

Result 3.9: Let (α, α^*) be a timelike Mannheim curve pair. The geodesic curvatures of spherical indicator curves (T^*),(N^*) and (B^*) of curve α^* in terms of S_1^2 or H_0^2 are

$$\begin{cases} \gamma_{T^*} = \left\{ \begin{array}{l} \left[\frac{\left(\frac{\sinh\theta}{k_C}\right)' - \left(\frac{\kappa}{k_N}\right)}{\sqrt{(\theta')^2 + \|W\|^2}} + \frac{\cosh\theta}{k_C^2} - \frac{\cosh\theta}{k_N^2} \right]^2 + \left[\frac{-\left(\frac{1}{k_N}\right)' + \kappa\left(\frac{\sinh\theta}{k_C}\right) - \tau\left(\frac{\cosh\theta}{k_C}\right)}{\sqrt{(\theta')^2 + \|W\|^2}} \right]^2 \\ + \left[\frac{-\left(\frac{\cosh\theta}{k_C}\right)' + \frac{\tau}{k_N}}{\sqrt{(\theta')^2 + \|W\|^2}} - \frac{\sinh\theta}{k_C^2} - \frac{\sinh\theta}{k_N^2} \right]^2 , W \text{ spacelike} \end{array} \right\}^{\frac{1}{2}} \\ \gamma_{T^*} = \frac{\|W\|}{\theta'} \quad , W \text{ timelike} \end{cases}$$

$$\begin{cases} \gamma_{N^*} = \frac{\|W\|}{\theta'} \quad , W \text{ spacelike} \\ \gamma_{N^*} = \left\{ \begin{array}{l} \left[\frac{\left(\frac{\sinh\theta}{k_C}\right)' - \left(\frac{\kappa}{k_N}\right)}{\sqrt{(\theta')^2 + \|W\|^2}} + \frac{\sinh\theta}{k_C^2} + \frac{\sinh\theta}{k_N^2} \right]^2 + \left[\frac{-\left(\frac{1}{k_N}\right)' + \kappa\left(\frac{\sinh\theta}{k_C}\right) - \tau\left(\frac{\cosh\theta}{k_C}\right)}{\sqrt{(\theta')^2 + \|W\|^2}} \right]^2 \\ + \left[\frac{-\left(\frac{\cosh\theta}{k_C}\right)' + \frac{\tau}{k_N}}{\sqrt{(\theta')^2 + \|W\|^2}} - \frac{\cosh\theta}{k_C^2} - \frac{\cosh\theta}{k_N^2} \right]^2 \quad , W \text{ timelike} \end{array} \right\}^{\frac{1}{2}} \end{cases}$$

$$\gamma_{B^*} = \mp \frac{\theta'}{\|W\|}$$

References

[1] Akutagawa, K., and Nishikawa S., The Gauss Map and Spacelike Surfaces with Prescribed Mean Curvature in Minkowski 3-space, Tohoko Math., J. 42, 67-82, 1990.

[2] Azak, A. Zeynep., Üç Boyutlu Lorentz uzayında Timelike Mannheim Eğri Çifti Üzerine, Sakarya Univ., Journal of Sci.II, 35-45, 2009.

[3] Bilici M., Çalışkan M. and Aydemir İ., The Natural Lift Curves and The Geodesic Sprays For The Spherical Indicatrices Of The Pair Of Evolute-Involute Curves, International Journal of App. Math., (11), 415-420, 2002.

[4] Burke J. F., "Bertrand Curves Associated with a Pair of Curves", Mathematics Magazine, 34(1), 60-62, 1960.

[5] Çalışkan M., Sivridağ A.İ. , Hacısalihoğlu H. H., Some Characterizations For The Natural Lift Curves and The Geodesic Sprays, Ankara Üniv., Fac. of Sci.,commun., (55), 235-242 , 1984.

[6] Ferrandez, A., Lucas, P., On surfaces in the 3-dimensional Lorentz - Minkowski space, Pasific J. of Math. 152(1), 1992.

[7] Görgülü, E., Özdamar, E.,"A Generalizations of the Bertrand Curves as General Inclined Curves in $\mathbb{E}^n$ ", Communications de la Fac. Sci. Uni. Ankara, Series A1, 53-60, 1986.

[8] Ergun E. and Çalışkan M., On the $\bar{M}$ - Integral Curves and $\bar{M}$ - Geodesic Sprays in Minkowski 3-Space, Int.J.Contemp. Math. Sci., 6(39), 1935-1939, 2011.

[9] Hacısalioğlu, H.H., Differential Geometry, İnönü Univ., Fac.of Arts and Sci. pub., (7), 1983.

[10] Liu, H. and Wang, F., Mannheim partner curves in 3-space, Journal of Geometry, 88(1-2), 120-126(7), 2008.

[11] O'neill, B., Semi Riemann Geometry, Academic Press, New York, London, 1983.

[12] Orbay K. and Kasap E., On Mannheim partner curves in $\mathbb{E}^3$, International Journal of Physical Sciences, 4 (28), 261-264, 2009.

[13] Ratcliffe, J. G., Foundations of Hyperbolic Manifolds, Springer-Verlag New York, Inc., New York, 736, 1994.

[14] Şenyurt, S., Çalışkan, Ö.F., The Natural Lift Curves and Geodesic Curvatures of the Spherical of the Timelike Bertrand Curve Couple International Electronic Journal of Geometry, vol.6,no.2, pp.88-99, 2013.

[15] Şenyurt S. and Bektaş Ö., Timelike-Spacelike Mannheim Partner Curves in $\mathbb{E}^3$, International Journal of The Physical Sciences, 7(1), 100-106, 2012.

[16] Şenyurt S., Natural Lifts and The Geodesic Sprays for The Spherical Indicatrices of the Mannheim Partner Curves in $\mathbb{E}^3$, International Journal of The Physical Sciences, 7(16), 2414-2421, 2012.

[17] Sivridağ A.İ., Çalışkan M., On The M-Integral Curves And M-Geodesic Sprays, Erciyes Univ., J. of Sci., 7(1-2), 1283-1287, 1991.

[18] Thorpe, J. A., Elementary Topics in Differential Geometry, New York, Heidelberg, Berlin: Springer-Verl., 1979.

[19] Turgut A.,3- Boyutlu Minkowski Uzayında Spacelike ve Timelike Regle Yüzeyler, Gazi Univ. Institute of Sci., Ph D thesis, 1995.

[20] Turgut, A., Esin, E., Involute- Evolute Curve Couples of Higher Order in $\mathbb{R}^n$ and Their Horizontal Lift in TIR^n, Commun. Fac.Sci. Univ. Ankara, Series A1, 41(3), 125-130, 1992.

[21] Uğurlu, H.H., On theGeometry of Timelike Surfaces, Commun. Fac. Sci. Ank. Series A1 (46), 211-223, 1997.

[22] Wang F., and Liu, H., Mannheim Partner Curves in 3-Space, Proceedings of the Eleventh International Workshop on Diff. Geom., 25-31, 2007.

[23] Woestijne, V.D.I., Minimal Surfaces of the 3-diemensional Minkowskispace. Proc. Congres "Geometrie differentielle et aplications" Avignon (30 May 1988), World Scientific Publishing. Singapore, 344-369.

DO HEAVY GAUGE BOSONS EXIST?

Kenneth Dalton
General Delivery
Bang Saphan Yai 77140
Prachuap Kiri Khan
Thailand
kxdalton@yahoo.com

Received October 14, 2014

Abstract

Recently, transverse and longitudinal solutions were found for the $W^{\pm}$ and Z^0 bosons. They satisfy the nonlinear cubic wave equation. Here, new solutions are given which correspond to heavy gauge bosons, with mass $m'_W = 114$ GeV and $m'_Z = 129$ GeV. A neutral particle has been found at CERN near 129 GeV. It remains to be seen whether charged particles will be discovered at 114 GeV.

Copyright © 2016 by Hadronic Press, Inc., Palm Harbor, FL 34684, USA

Previously, it was shown that the gauge bosons $W_\mu^\pm = (W_\mu^1 \mp W_\mu^2)/\sqrt{2}$ and the scalar field Φ are coupled, according to the equations [1]

$$\partial_\mu \partial^\mu W^\nu + \frac{1}{4} g^2 W^\nu \phi^2 = 0 \tag{1}$$

$$\partial_\mu \partial^\mu \phi - \frac{1}{4} g^2 W_\mu W^\mu \phi = 0 \tag{2}$$

where W_ν is either W_ν^1 or W_ν^2. These equations derive from the standard electroweak Lagrangian. The unitary gauge is chosen

$$\Phi = \begin{pmatrix} \phi^+ \\ \phi^0 \end{pmatrix} \longrightarrow \begin{pmatrix} 0 \\ \phi/\sqrt{2} \end{pmatrix} \tag{3}$$

where $\phi(x)$ is real. Traveling solutions exist which are polarized, $W^\mu(u) = \epsilon^\mu \phi(u)$, where $u = -k_\mu x^\mu$ and ϵ^μ is a real polarization vector. Such vectors are space-like, $\epsilon_\mu \epsilon^\mu = -1$, so that both (1) and (2) will be satisfied if

$$\partial_\mu \partial^\mu \phi(u) + \frac{1}{4} g^2 \phi^3(u) = k_W^2 \frac{d^2\phi}{du^2} + \frac{1}{4} g^2 \phi^3(u) = 0 \tag{4}$$

This cubic wave equation is solved by the elliptic function $\mathrm{cn}(u, \frac{1}{2})$

$$\phi(u) = \frac{2k_W}{g} \mathrm{cn}(-k_\mu x^\mu) \tag{5}$$

The amplitude of this traveling wave is not arbitrary, but is fixed by the value of $2k_W/g$. The coupling between Z^0 and Φ is described by similar equations

$$\partial_\mu \partial^\mu Z^\nu + \frac{1}{4}(g^2 + g'^2)\, Z^\nu \phi^2 = 0 \tag{6}$$

$$\partial_\mu \partial^\mu \phi - \frac{1}{4}(g^2 + g'^2)\, Z_\mu Z^\mu \phi = 0 \tag{7}$$

Once again, the solutions are polarized, $Z^\mu(u) = \epsilon^\mu\, \phi(u)$, where

$$\phi(u) = \frac{2k_Z}{\sqrt{g^2 + g'^2}} \mathrm{cn}(-k_\mu x^\mu) \tag{8}$$

There is another solution to the cubic wave equation. It takes the form of the elliptic function $\mathrm{dn}(u, m)$, with derivatives [2]

$$\frac{d\,\mathrm{dn}(u,m)}{du} = -m\,\mathrm{sn}(u,m)\mathrm{cn}(u,m) \tag{9}$$

$$\frac{d^2\mathrm{dn}(u,m)}{du^2} = -m\,\mathrm{dn}(u,m)\{1-2\,\mathrm{sn}^2(u,m)\} \tag{10}$$

Substitute $\phi(u) = a\,\mathrm{dn}(u,m)$ into (4) to find that the equation is satisfied, if the parameter $m = 2$ and $a = 2\sqrt{2}\,k_W/g$

$$\phi(u) = \frac{2\sqrt{2}\,k_W}{g}\,\mathrm{dn}(u,2) \tag{11}$$

The period of an elliptic function is well-defined, if $0 < m < 1$. The function $\mathrm{dn}(u,2)$ may be converted by means of the reciprocal formula [2]

$$\mathrm{dn}(u,2) = \mathrm{cn}(v,\frac{1}{2}) \tag{12}$$

where $v = \sqrt{2}\,u$. It follows that

$$\phi(v) = \frac{2\sqrt{2}\,k_W}{g}\,\mathrm{cn}(-\sqrt{2}\,k_\mu x^\mu) \tag{13}$$

with $W^\mu(v) = \epsilon^\mu\phi(v)$. The period of this solution is identical to that of (5), i.e., since $m = \frac{1}{2}$, the quarter-period is $K \doteq 1.85$. However, the argument and amplitude are both greater than those in (5) by the factor $\sqrt{2}$. Since k_W is directly proportional to the mass m_W, the new solution represents a charged vector boson with mass $m'_W = \sqrt{2}\,m_W$. Similarly, the Z^0 equations (6) and (7) admit the new solution

$$\phi(v) = \frac{2\sqrt{2}\,k_Z}{\sqrt{g^2+g'^2}}\,\mathrm{cn}(-\sqrt{2}\,k_\mu x^\mu) \tag{14}$$

with $Z^\mu(v) = \epsilon^\mu\,\phi(v)$. This represents a neutral vector boson of mass $m'_Z = \sqrt{2}\,m_Z$. Substitute the known values $m_W = 80.4$ GeV and $m_Z = 91.2$ GeV to find $m'_W = 114$ GeV and $m'_Z = 129$ GeV. A neutral boson has been found at CERN near 129 GeV, while Fermilab is reporting activity in the range 115-135 GeV. It remains to be seen whether charged bosons will be discovered at 114 GeV.

References

[1] K. Dalton, "On the $W^{\pm}$ and Z^0 Masses", submitted to The Hadronic Journal.

[2] M. Abramowitz and I. Stegun, *Handbook of Mathematical Functions*, (Dover, New York, 1965) p. 569. Also, http://www.dlmf.nist.gov/22

A STUDY OF THE FUNDAMENTAL ORIGIN OF THE DIMENSION OF THE BOHR RADIUS OF THE HYDROGEN ATOM AS DETERMINED BY THE QUANTIZED DYNAMIC ELETRIC FIELD SURROUNDING A VORTEX MODEL OF THE ELECTRON

Ernst L. Wall
Odyssey Systems
19 Crosby Dr.
Bedford, MA 01730 USA
ernst.l.wall@gmail.com

Received March 10, 2016

Abstract

In this study, we utilize a novel classical vortex electron model whose interaction with the nucleus of the hydrogen atom provides a value of $a_0 = 21.809394$ Compton wavelengths for the first Bohr radius, which is within 52 ppm of the actual value. The vortex electron model's point charge revolves at light speed in an orbital circumference that is a Compton wavelength, so that it generates electrical field impulses that spiral outward in waves having a spacing of a Compton wavelength resulting in a species of quantized waves. We call these waves Compton wavelets. To support the validity of this model of the electron, when the vortex electron's point charge is modeled as a point charge revolving at the speed of light in a Compton wavelength orbit, its magnetic moment is found to be the Bohr magneton, identically. Also, the mass-energy of the electron is provided, identically, by this model. Further, an analysis of the interaction of the Compton wavelets from two electrons provides the fundamental basis for the electron's de Broglie waves between two moving electrons with additional behavior that could be described as forms of pilot waves. This origin of the de Broglie waves from a classical model further justifies the use of a classical electron model to analyze what is generally seen as a quantum mechanical phenomena in the Bohr atom. In addition, we also

Copyright © 2016 by Hadronic Press, Inc., Palm Harbor, FL 34684, USA

relate the finite sized orbital radius (the reduced Compton wavelength) of the vortex electron to the first Bohr radius of the hydrogen atom directly by means of the inverse fine structure constant. We utilize the inverse fine structure constant to relate the mass energy of the electron itself to its potential energy in the Bohr atom's radius. The resultant inverse fine structure constant derived from this is also accurate to within 52 ppm of the known value. Then the nucleus of the hydrogen atom is close enough to the electron, these wavelets reflect off of the nucleus and synchronously impinge on the electron. This train of wavelets moving from the electron to the nucleus and back to the electron with a fixed phase relationship with the electron prevents it from moving any closer to the nucleus. We consider two mechanisms for holding the electron in place when the wavelets impinge on the electron: One is a simple synchronous impact between the wavelet and the charge. The other is suppression of the electron's ability to radiate when the reflected wavelets synchronously overlay the electron and neutralizes its ability to radiate. When this vortex electron is accelerated, the wavelets in front of it are compressed and the wavelets behind it are decompressed, both at an increasing rate. The result is an increasing differential electric field across the electron in the direction of travel, this increasing field serving to generate a photon as the electron is accelerated towards the nucleus. This would provide a possible mechanism for maintaining the electron at the first Bohr radius if the reflected wavelet synchronously overlays the electron and neutralizes its ability to radiate its energy away. A number of impact patterns were tried, but this methodology provided an accuracy of 52 ppm, the greatest accuracy of all possibilities tried. Because of the dimensions and times involved, as well as the need to synchronize the electron's charge angle with the phase of the reflected wavelets, we define here a natural set of units for dealing with these problems. This set of units is based the Compton wavelength, the rotational time of the electron, and the mass of the electron. We call this set of units "Electron Units", or "EUs", where the basic units of length, time, and mass are called the Compton, the rotation, and the em for the electron mass. These units are also much more human readable and meaningful for this kind of study than are the CGS dimensions for atomic dimensions. We also define the electrodyne and the electroerg as units of force and work, respectively. Finally, we make a brief comparison of this model of the electron with that of the standard model in Appendix A.

1 Introduction

The Bohr model of the hydrogen atom was supplanted by quantum mechanics some 85 years ago. Since that time, it has been primarily taught in modern physics courses as an historical artifact. But at the same time, however, it has served as an introduction to the basic concepts of atomic physics.

In the Bohr model as we currently know it, the lengths of the Bohr radii are determined by the fact that the angular momentum of the electron is quantized in integral multiples of $\hbar$. The first Bohr radius, of course, has a single multiple of $\hbar$.

Here, we wish to provide a novel but fundamental foundation that should, in time, provide a much more fundamental mechanism to explain the fundamental origin of the orbital de Broglie waves in the hydrogen atom, as well as the wave equation in terms of what we call "Compton wavelets" that are emitted by a revolving vortex electron model.

Normally, the Bohr model assumes the electron to be a point sized charge. However, here we utilize a theoretical model of the electron whose point charge revolves at the speed of light in a Compton wavelength orbit, giving the electron a finite size in its stable atomic state.

In this finite sized electron model, as the tiny charge revolves in the light speed orbit with its Compton wavelength circumference, it produces the Bohr magneton, identically, for the electron's magnetic field. In addition, it produces the known expression for the mass-energy of the electron identically [1, 2, 3] with the mass-energy spread across the extent of the electron. We will show this derivation, below.

As we will demonstrate later in this work, the mass energy is contained in the field over the entire volume of electron and not within the charge itself, so that the charge itself has no mass [3, 4]. Hence, having only charge but no mass, the charge is not precluded from revolving at the speed of light.

More important, this revolving charge, rather than producing a static electric field, produces an impulse field that spirals outward in electric field waves that have a spacing between the waves of a Compton wavelengths [5, 6, 7]. Because they spiraled outward, we initially called this a "water sprinkler" model when it was first introduced as a theoretical construct in the late 1990s. However, in the last few years the term "vortex electron" seems to have become more commonplace based on recent experimental evidence of spiraling fields associated with electrons [8, 9, 10] . While a vortex is normally thought of as

spiraling inward, we have adopted the term vortex because most workers in the field are familiar with that term but not water sprinkler model.

In addition, we used the Compton wavelets in that earlier work to derive a fundamental mechanism that gave rise to de Broglie waves for the case of linear electron-electron interactions [5, 6, 7]. This is as opposed to an electric field around the electron that is composed of a simple, static electric gradient.

But in using this methodology here, we extend the usage of an existing fundamental model for the de Broglie waves from the case of electron-electron interactions to the case of the Bohr atom's electron-nucleus interaction [11, 12, 13, 14] . Using this version of the model, we were able to calculate the first Bohr radius and the Bohr atom's inverse fine structure constant to within 52 ppm of experiment by utilizing the Compton wavelets.

In order to try to obtain a fundamental foundation for the understanding of the root basis of why quantization arises in atoms and how it relates to the model we use here, we wish to use this finite sized electron model along with its Compton wavelets to lay a foundation that will ultimately achieve this understanding. More specifically, we wish to provide a foundation for understanding fundamental origins of spherical de Broglie waves and the causes of quantization, not only in the basic Bohr atom, but for quantization in general.

In the Bohr atom, these dynamic Compton wavelets, that are generated by the electron, travel to the nucleus and are reflected back to it by the nucleus, there being a train of 43 wavelets between the emission point on the electron and the impact point on the electron, plus a 0.75 Compton from a partial rotation of the electron. Finally, when these reflected wavelets impact the electron, they serve to limit how close the electron can approach the nucleus. That is, the minimum approach distance of the electron from the nucleus is the first Bohr radius. In effect, this train of wavelets forms a standing wave pattern.

In order to provide a basis here for this electron model, we will review the dynamic behavior of this finite sized electron and show how it produces the Bohr magneton and also the mass energy of the electron, identically. These parameters that it produces provide a prior indication of the model's validity that is independent of its application here [1, 2, 3].

Further, we will show how the electron's de Broglie waves arise from these Compton wavelets. Also, the interaction of the wavelets from two electrons have a behavior that can best be described as a form of pilot wave [15, 16].

As a secondary issue, we will expand on several Bohr atom inverse fine structure relations. While some of these relations have been well known since

the early days of quantum mechanics, they are usually viewed as being abstract numbers. However, their utilization here will be different. What is different is that we will relate the finite sized vortex electron's radius to the length of the first Bohr radius by means of the fine structure constant. This, then, will provide a completely different context for the behavior of the physical parameter by providing them with a tangible physical rationale as well as provide a further indication that the electron, as a whole, is not a point particle, but that it has a finite size.

A specific case that we will develop here will utilize the square of the inverse fine structure constant to demonstrate that the mass energy of the finite sized electron itself is directly related to its potential energy in the first Bohr radius.

Finally, we will describe some scenarios where the emission of the wavelets occur at different cardinal points of the charge on the electron's internal orbit, reflect off the nucleus, and then the wavelets return to impact the charge at different points on the orbit. We utilize round trip trains of both 43 and 44 basic wavelets here in order to determine the best fit. Ultimately, however, a train of 43 wavelets provides the best results. Each of these scenarios will then provide its own Bohr radius, most of which are not very accurate. One of them, however, will provide an accuracy 40 times more accurate than the best of the others, namely, an accuracy of 52 ppm for the first Bohr radius.

The specific model we utilize here requires that the wavelet emission by the charge occurs parallel to the orbital velocity vector in a cyclotron radiation-like manner. The returning wavelet will impact the charge when it is on the back side of the electron's orbit with respect to the nucleus. That is, its velocity vector is parallel to the charge's radial vector at impact. However, when corrected for the finite size of the electron with respect to the Bohr radius, its accuracy will be reduced down to 52 ppm. The resulting relationship between the Bohr radius and its circumference will provide the inverse fine structure, and its accuracy will also be 52 ppm.

While the model's accuracy in providing a mechanism for maintaining the length of the first Bohr radius and its inverse fine structure constant is most important, we make a further claim. Namely, we claim that the very accuracy of this model in providing these parameters is evidence that indicates that, within a high likelihood, the electric field surrounding the electron is not a continuous static field. Instead, it is a dynamic, spiraling field that gives rise to the electron's de Broglie waves, the fundamental basis for quantum mechanics.

We make a brief comparison of this model with that of the standard particle model in the appendices.

2 A classical approach to modeling the vortex electron

While the intention of this work is to explore the electron's wavelet behavior in the first orbit of the Bohr hydrogen atom, the behavior of the electron in that orbit is dependent on its own dynamic characteristics. Hence, in the next several sections we will collect together various parameters and their relevant relationships from disparate sources so as to provide a coherent picture of the finite sized vortex electron in one location.

Our first step for this particular study, as well as for future development, is to summarize a previously described model of the electron. That model consists of a tiny charged particle that revolves in a light speed orbit having a Compton wavelength circumference [1, 2, 3]. Hence, its frequency of rotation is given by

$$f_e = \frac{c}{\lambda_C} = \frac{mc^2}{h}, \tag{1}$$

where λ_c is the Compton wavelength and m is the mass of the electron. Note that the tiny charged particle itself has a radius of the order of 10^{-17} cm, or less, based on high energy scattering experiments [17].

To expand on this, if an observer were standing near the circular orbit of the revolving particle, the current that he would see would be given by the number of charges per second passing by him, or

$$I = nq = f_e q = \left(\frac{c}{\lambda_C}\right)\left(\frac{e}{c}\right) = \frac{e}{\lambda_C}, \tag{2}$$

where we use the frequency from Equation 1, above, and the CGS unit of charge, q = e/c. The magnetic moment of an orbiting charge is then found to be

$$\mu = AI = \pi\left(\frac{\lambda_C}{2\pi}\right)^2\left(\frac{e}{\lambda_C}\right) = \frac{e\lambda_C}{4\pi} = \frac{eh}{4\pi mc} = \frac{e\hbar}{2mc}, \tag{3}$$

which is the Bohr magneton identically.

Having derived the Bohr magneton for the electron using this electron structure, we now treat the electron's charge as if it were a photon trapped in a circular orbit and apply the Einstein photoelectric Equation 1. This gives us the energy of the electron's charged particle, which is

$$E_e = hf_e = h\frac{c}{\lambda_C} = h\frac{mc^2}{h} = mc^2. \qquad (4)$$

Note that this is well known to be the energy of a Compton wavelength photon. However, we claim here that this equation is explicitly the mass energy of the electron itself. This is due to its consisting of the revolving point charge that is moving at the speed of light, the mass energy of the electron being contained within its overall field of the electron, not in its charge [3, 4]. We will show this in more detail later. Hence, the charge itself does not appear to be precluded from moving at the speed of light.

Further, in view of Eqs. 1 – 4, a relatively large structure with a light speed charge revolving at its periphery is required in order to produce the known values of the magnetic moment and mass energy. Compare the 10^{-17} cm charged particle size with the radius of the vortex electron, $r_e = \lambda_C / 2\pi = 3.8615926800E\text{-}11$ cm [18]. I.e., the electron's radius is about a million times larger than that of the charge. Based on this, it is totally illogical to expect a 10^{-17} cm sized particle to contain the electron mass or to produce its magnetic moment.

Furthermore, as we will show later, the mass is not likely to contained in the classical radius of the electron.

To summarize the significance of Equations 1 – 4, we state that we are justified in assigning a relatively large, finite size to the electron. Specifically, based on Eq. 4, the revolving charge behaves as if it were a trapped photon in that when its rotational frequency is multiplied by Planck's constant, it provides the mass-energy of the electron. But having noted this, we are unable to propose any reasonable mechanism that confines the charge and its energy to its orbit at this time. We can only state that these equations provide numerical values for their parameters that are consistent with experiment and then utilize them and see where it leads.

At this point, we should comment that this model is, in no way, an ad hoc model. Instead, it was an unexpected outcome that was derived from a negative mass tachyon model, a negative mass tachyon that was hypothesized after

having abandoned the imaginary mass tachyon was meaningless [2, 3, 19]. Specifically, this imaginary mass entity was abandoned because it is without any apparent real physical meaning and, furthermore, there is no experimental evidence whatsoever of its existence, either direct or indirect, except for one possible case.

The imaginary mass tachyon was proposed by Bilaniuk, Deshpande, and Sudarshan over 50 years ago [19]. In all of that time, it has produced nothing that was even indirectly observable. However, their originality is to be highly commended and it is also to be stated that these authors have earned a rightful place in the history of physics by proposing a new concept that provided the study of an entirely new domain of physics.

In that particular case, Recami and Mignani showed that an imaginary mass model would manifest itself as a negative mass to a subluminal observer [20]. This was used as a reference to justify the negative mass model that had been hypothesized for the original publication of this model [2, 3].

In contrast to the imaginary mass particle, the negative mass tachyon model has a physical meaning in that it is, in effect, an antigravity particle. But more important, it provided indirect evidence for its own existence when it provided the Bohr magneton for the electron. That model provided the orbital dimensions of the revolving charge electron by utilizing the cutoff energy of the $\mu \rightarrow e$ decay curve as the tachyon's binding energy to the charge. It should be noted that it also provided the magnetic moment for the muon. However, the inclusion of the muon model here, outside of a brief mention, was not necessary, so we only quote the results the electron model provided in the form of Equations 1 – 4 [1, 2, 3].

In a sense, this electron model could be described as a Bohr-like electron model in its simplicity except that, as previously stated, there is no obvious central force holding it together.

For some other examples of the usage of the term "vortex electron", we note that there is experimental evidence for the existence of what is called a vortex electron, or electron vortex. Uchida and Tonomura have described an experiment that involves the generation of electron beams carrying angular momentum[8], and VeerBeck and Schattschneider provide a model describing the production of electron "vortex" beams that consist of spiraling wavefronts [9]. While Schattschneider and Verbeeck have proposed a quantum mechanical vortex model [10] where the entire electron carries angular momentum around the center of a beam, they utilize dimensions of the order of a micron, whereas

we speak of dimensions of the order or the reduced Compton wavelength, or 3.8615926800E-11 cm. These are typically generated by utilizing laser beams to create the angular momentum.

But having pointed out this work, we wish only to state that what we have developed here is a totally different concept that describes the electron itself as generating a vortex around its center, whereas the above phenomena involves the entire electron revolving in a relatively large orbit around the axis of an electron beam.

What effect the present model has on these beams, if any, is unclear at this time, and it is beyond the scope of this work to discuss it further.

In summary, the electric field of the electron is not a continuous static field emanating from a tiny, fixed, 10^{-17} cm point charge, but it is a spiraling, dynamic field that ultimately is the likely cause of quantization, as we will illustrate.

When this particular model that we use here was first proposed, it was referred to as a "water sprinkler" model because the field spirals outward in the same manner as a water sprinkler [5, 6, 7]. A vortex, on the other hand, is generally thought of as a spinning, inwardly moving field such as the case of water pouring down the drain of a sink or a tornado. Perhaps it would not be inappropriate to refer to this model as being a "negative vortex".

In any case, because of a growing usage of the vortex terminology in the case of electrons, that terminology has been adopted here. However, we distinguish between the two concepts by referring to the present fundamental electron model as a vortex electron of the first kind, and the above model as a vortex electron of the second kind.

As we will illustrate with the de Broglie wave model below, if a microscopic, negatively charged observer could stand near the electron's circular orbit, he would experience a momentary force pushing him away from the electron each time the charge passes by him. That force is caused by the electric field emitted by the passing charge. More specifically, the electron's electric field is a dynamic impulse field that arises from the revolving point charge and spirals outward at the speed of light and has a spacing between waves peaks equal to the Compton wavelength.

In the original model, the electric field was a longitudinal field directed away from the electron's charge, i.e., in the direction of the charges radius vector. This is as opposed to a transverse oscillating field like that of a photon, so there is no a priori reason to expect radiation to be emitted as would be the case if the field were a transverse field.

3 The generation of the vortex electron field and the origin of the Compton wavelets

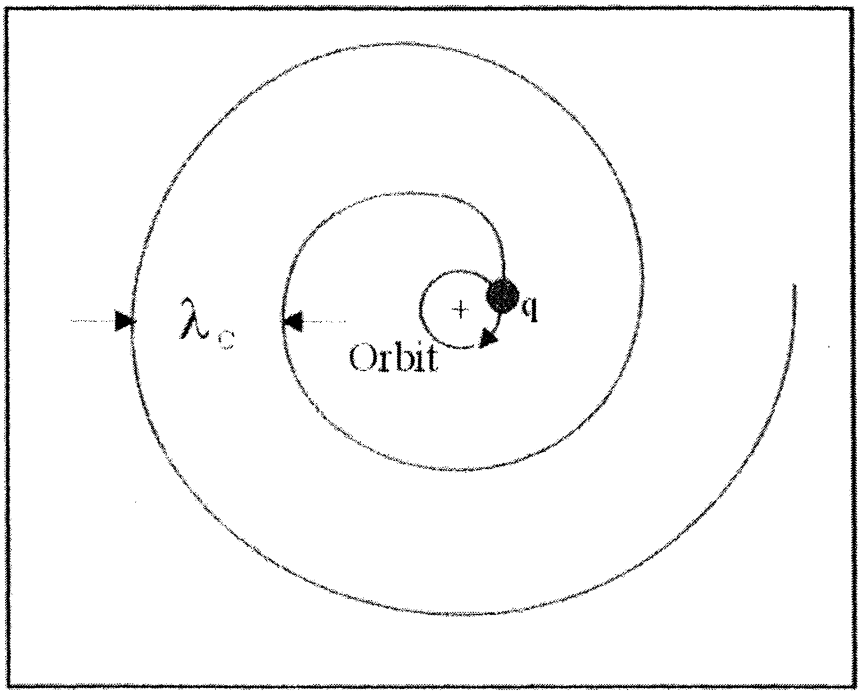

Figure 1. This is the vortex electron. The charge q revolves in the Compton wavelength orbit at the speed of light. As a result, an observer near the orbit would experience an impulse generated by the passing charge every time it passes. This impulse then would then spiral outward in wavelets having a spacing between them of one Compton wavelength so as to form a species of quantized waves. Hence, when first described in the late 1990s, there was no precedent for it, so it was initially called a "water sprinkler" model [5, 6, 7].

We will refer to these spiraling light speed wavelets, emitted by the tiny revolving charge in its light speed Compton wavelength orbit, as Compton wavelets. Their radial spacing with respect to a line from electron center is, therefore, equal to the Compton wavelength.

We note that this also implies that the spiraling, dynamic field of an electron fills all space out to infinity. Otherwise, the electrostatic extent of the electron's

field would be limited. However, it is beyond the scope of this work to consider this any further outside of a near-field analysis within the Bohr atom.

While it is likely that the experimental data described above can be described by expanding the model we use here, our purpose here is purely intended to explore the origins of the quantized dimension of the first Bohr radius and the resultant fine structure constant determined from it [11, 12, 13, 14]. Hence, we will make no further comparisons between this work and the above experimental work.

In any case, however, the model we describe here is purely meant as a logical extension of the model described in Equations 1 – 4 and is based on that alone.

4 Criteria for the electron-wavelet interaction and a pilot wave model

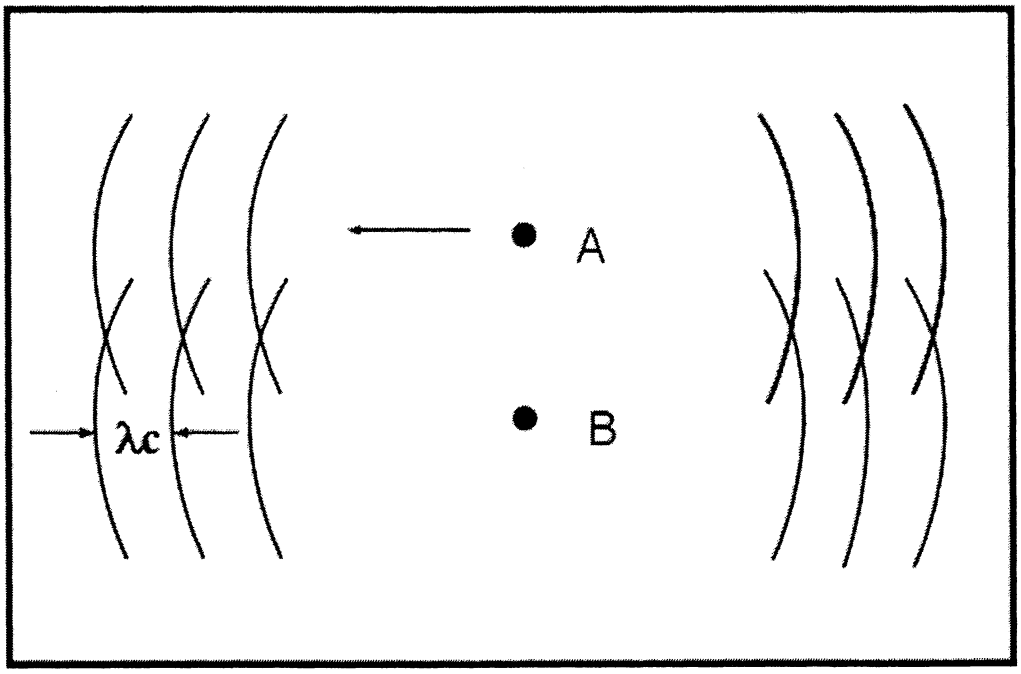

Figure 1a. These are the Compton wavelets emitted by two electrons, where electron B is stationary and electron A is moving. As a result, the two wavelet sets move in and out of phase.

In general, if there are two nearby electrons, the impact of the wavelets from each of them will impact on the charge in the other. However, on this alone we know nothing about the phase of the electron as it interacts and if the phase has any importance in the interaction.

But to examine this in more detail, consider the case of two nearby electrons, A and B, which are stationary. In that case, the wavelets from the two electrons will move outward at the velocity of light with a constant phase relationship with one another in that region which is much greater than the spacing between them.

Then, if one of them, say B, is stationary but A moves slowly with velocity v past particle B, then a nearby observer will see the relative phase of the wavelets change. I.e., they will be going in and out of phase.

In one unit of time t, the electron will move a distance d, and the relative phases of the wavelets will be changing continuously.

When the relative phase of the wavelets is 0 (or 2π), then a double wavelet will occur. The number of these doublets, or phase crossings that will occur in some time of unit is

$$n = \frac{d}{\lambda_C} = \frac{vt}{\lambda_C} = \frac{mcvt}{h}. \tag{5}$$

Using the definition of the Compton wavelength, $\lambda_C = \frac{h}{mc}$, we have for the frequency of crossing, which we define as f_D, is

$$f_D = \frac{n}{t} = \frac{mcv}{h}. \tag{6}$$

Because the wavelets are light speed entities, we may solve Equation 6 for a wavelength between the crossing points as

$$\lambda_D = \frac{c}{f_D} = \frac{h}{p}. \tag{7}$$

Thus we have that the phase crossings (the doublets) of the wavelets are propagated outward with spacings between them of λ_D, which is obviously the de Broglie wavelength by definition [15].

However, it is to be emphasized that this model of a de Broglie wave has a physical meaning only when an electron's charge interacts with a wavelet with a fixed relative phase relationship. A wavelet-wavelet interaction has no physical meaning insofar as interactions are concerned.

Moreover, when it is not a wavelet that is crossing another wavelet, but is the edge of an electron at the point where the charge is located, then that implies that for the de Broglie wavelength to have a physical meaning, the electron itself must interact with the wavelet with its charge hitting the wavelet at some fixed phase relationship between the charge and the wavelet. Further, the relative phases of the wavelet and the charge angle must have some latitude, otherwise, the above equations would hold only for very specific, very precise velocities. Ether that would have to be the case, or the width of the wavelet would have to have some relatively large, finite width.

That is to say, the charge on the edge of the electron is, in effect, the first Compton wavelet and it is this interaction of the electron's charge with the other electron's wavelets that cause an interaction. Specifically, the interaction causes repulsion only as certain specific relative phases between the wavelet from one electron and charge angle of the impacting electron.

However, it must also be added that this wavelet is not necessarily a phenomena that is limited to the plane of the electron's orbit. It is described elsewhere as a field that surrounds the charge in two dimensions perpendicularly to the plane of the orbit. I.e., it is like a disk in the vicinity of the charge that revolves with the charge [6, 7] and with its plane perpendicular to that of the electron's plane. (See Appendix B.)

Another concept that we introduce here is that, based on Equations 5-7, the de Broglie wavelength is a subset of the Compton wavelengths. For instance, in the case of the electron, the Compton wavelets are much smaller than the de Broglie waves normally associated with them.

To provide a brief graphical illustration of the wavelet interactions, Figure 2 provides the interaction of possible sinusoidal wavelets from two electrons that are moving directly away from each other, the phase distance being measured in Comptons. At the peaks of the envelopes, the wavelets are in phase which indicates that either two wavelets would be crossing, either that, or an electron itself will be impacting a wavelet, depending on the point in space. The peak to peak distance of the envelope is one de Broglie wavelength, but the spatial distant will depend how long it takes the electron to move that distance. Each of the oscillations in the envelope represent a single rotation of the electron.

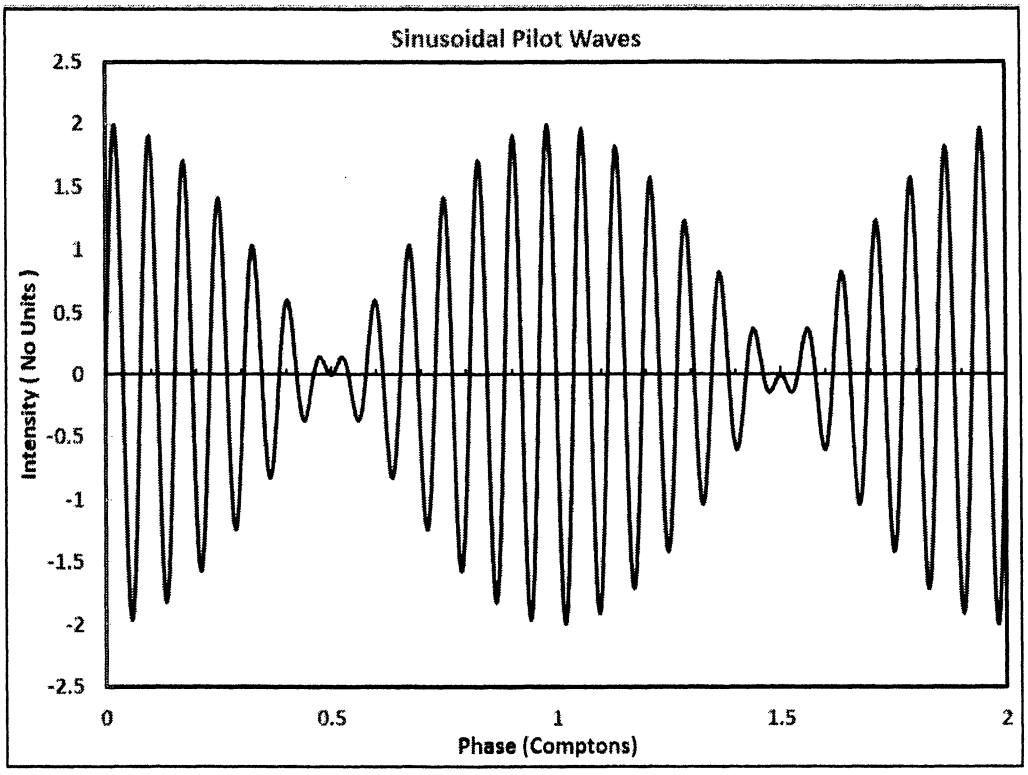

Figure 2. These are obtained by combining sinusoidal Compton wavelets from electrons A and B while they are slowly moving away from one another.

Having noted that the peak spacing of the envelope is one Compton, we point out that the spacing of the oscillations within the envelope is dependent on the relative electron velocity, so this would require an extreme relativistic particle to produce the spacings as shown here. It is shown this way for illustrative purposes.

In reality at the low energies we use here, the envelopes containing the oscillations would contain a much, much denser set of oscillations representing many more rotations of the electron for the case of a low energy electron interaction.

This wavelet interaction is reminiscent of the pilot waves studied by de Broglie, except that a single frequency is used rather than dual frequencies as

discussed by Eisberg for a single particle, and the interference comes from the changing particle spacing, or relative phase change [15]. A good analogy for this particular phenomena is that the relative phases change in such a manner that we obtain an interference pattern similar to that of a Doppler radar.

On the other hand, it is unlike the Fourier analysis over a frequency continuum as provided by Bohm, which provides a wave packet that is localize to a single region of space around some frequency ω_0 [16].

Here, we choose to use the term "pilot wave" for this phenomena after de Broglie. In any case, we make the claim that these wavelets, when they interact, could be considered to be a rudimentary form of pilot waves that arise from a dual particle interaction as opposed to being a single particle phenomena. But their inclusion here is incidental to the real issue, which is the basis we use for de Broglie waves that arise from the Compton wavelets.

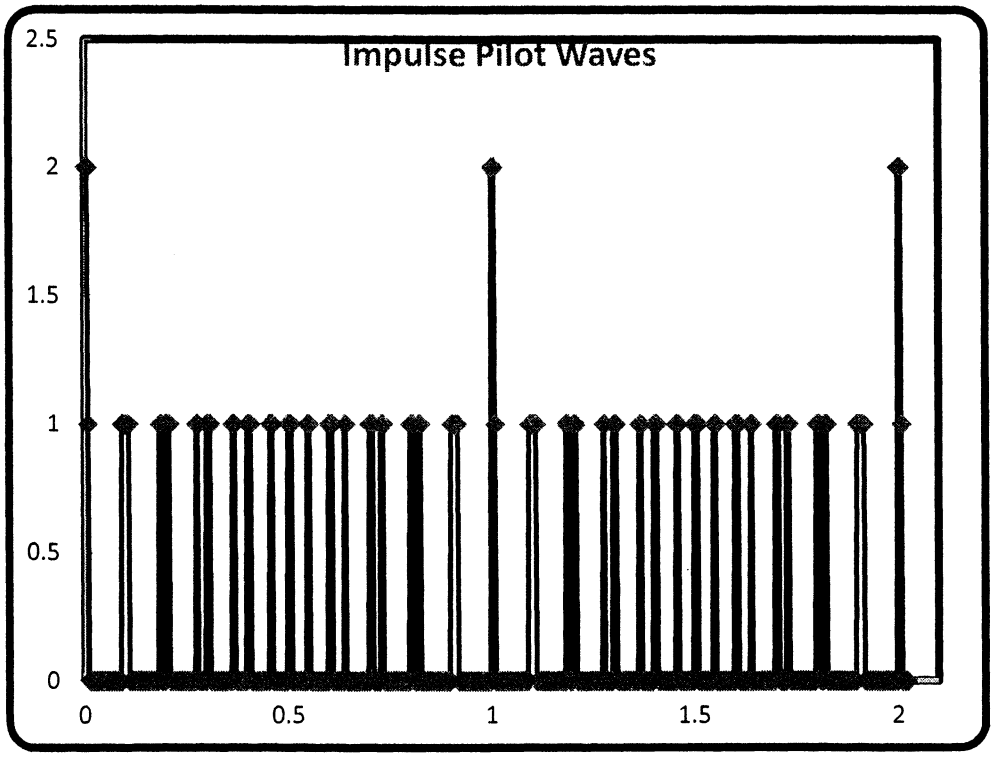

Figure 3. Impulse pilot waves obtained by adding a 5 degree wide impulse for electrons A and B and slowly moving them away from one another.

Figure 3 is similar to Figure 2, but rather than sinusoidal wavelets, we use square, 30 degree width pulse wavelets. When a wavelet crosses another wavelet, or when the electron impacts a wavelet, you get a peak as shown there. That is, it is one de Broglie wavelength from peak to peak. Like the case of Figure 2, this would be an extreme velocity case, and is for illustrative purposes only.

Also, Figure 3 illustrates the point that for an interaction to take place, the relative phases of the electron and wavelet must be within some finite range and the wavelet must have some finite width at the interaction point. Otherwise, a very precise velocity would be required in order to achieve an interaction.

But having considered all of this, a good argument can be made that the above equations provide a means of utilizing wavelets to provide a fundamental basis for quantum mechanics. However, these are linear equations, and we need to develop a rational for transforming them into a spherical form that will be consistent with a standard quantum mechanical treatment of the atom, namely, the Schrodinger equation.

5 Definitions of Electron Units, the natural units of measurement for the vortex electron model

The radius of the vortex electron that we will model here is equal to the reduced Compton wavelength, which is 3.8615926800E-11 cm [18]. The circumference of its orbit is, then, 2.4263102389 E-10 cm, which is a Compton wavelength.

While a computer can handle these numbers as well as any other number, they are somewhat clumsy for a human being to visualize. Therefore, it is convenient to define a few units of measurement that make the interpretation of the computer data we obtain here a little more palatable and obvious to a human observer.

The first unit of distance we will define here is the unit of length, or the Compton, which is equal to the Compton wavelength and which is also the circumference of the vortex electron. Also, as previously stated, the wavelets it generates extend a Compton wavelength from peak to peak.

This means that the radius of the electron in Comptons is simply

$$r_e = 1/2\pi \text{ Comptons} = 0.15915494309 \text{ Comptons}, \quad (8)$$

which is the reduced Compton wavelength. We wish to point out here that neither this nor the Compton wavelength have anything directly to do with the classical electron radius, which is

$$r_{classical} = 2.8179403267\text{E-}13 \text{ cm} = 0.001161409732 \text{ Comptons}. \quad (9)$$

[18]. However, as an aside here, we note in passing that the ratio of the radius of the vortex electron to the classical electron radius is

$$\frac{r_e}{r_{classical}} = 137.035999074, \quad (10)$$

which is equal to the known value for the inverse fine structure constant, 137.035999074 [18]. We have no explanation for this relationship at this time, but we will briefly return to it again in Appendix E.

To put these in perspective with the Bohr model, note that the first Bohr radius of the hydrogen atom is 5.2917721092E−9 cm in length. This is 21.809956634 Comptons, which is the distance from the center of the nucleus to the center of the electron. That is to say, the first Bohr radius has the dimensions of

$$a_0 = 21.809956634 \text{ Comptons}. \quad (11)$$

But we note that if we simply multiply Eq. 11 by 2π, we obtain

$$2\pi\, a_0 = 137.03599907 \text{ Comptons} = C_{Bohr} \text{ Comptons}. \quad (12)$$

This, of course, is the fine structure constant expressed in Comptons, and it is also the circumference of the first Bohr orbit.

Normally, of course, the fine structure constant would not have any units, but in this case it does. But more important, it provides another relationship between the Bohr radius and the inverse fine structure constant.

But to move on to the units of time and velocity, the rotational frequency of the electron is

$$f_e = 1.23558996E+20 \text{ Hz}, \quad (13)$$

which is calculated from the speed of light (2.99792458E10 cm/s [18]) and the Compton wavelength. Thus, it has a rotational period of

$$t_e = 8.09329979E-21 \text{ seconds}. \quad (14)$$

Because of this short time, the unit of time we define here is the amount of time it takes an electron's charge to make one revolution and thus, to generate a single Compton wavelet. Hence, we will simply designate our unit of time as a rotation, or we may abbreviate it as a "rote".

The unit of velocity that we will define for a moving electron is, therefore, Comptons per rotation, or as we may abbreviate, Cmptn per rote.

The electron's charge moves one Compton per rotation and it moves at the speed of light. Therefore, one Compton per rotation is, by definition, the speed of light. Or, to take it a step further, the unit velocity in this system of units is the speed of light.

The units of acceleration would be, then, Comptons/rotation^2 .

Finally, were we to need a unit of force here, we would need a unit of mass. For this, we would logically choose the electron's mass.

Using this, the fundamental unit of force would be defined as the force necessary accelerate the electron mass at a rate of one Compton/ rotation^2. We propose to call this unit of force one electrodyne.

The unit of work we will define as one electroerg. It occurs when a unit of force is exerted over a distance of one Compton.

But to utilize these units for more general computational purposes, we would need to define units of electron charge for force calculations and current, and also Planch's constant would need to be converted to these Electron Units. Generating an entire table of units, however, is beyond the scope of the present work.

Thus, we have defined a natural set of units specifically for dealing with electrons in an atom. We will simply call these "Electron Units" at this time, for lack of a better term. These are much more human readable for these dimensions that are CGS units, and they are natural for the electron because they use electron parameters.

We note that Angstroms are also more human readable at these dimensions than are standard CGS units, but they are not natural units specifically for the electron.

But having defined or described all of these Electron Units, for possible future usage, we do not find it necessary to use all of them here. We only use primarily Comptons and rotations here.

6 Some relationships between the Bohr atom's radius and the finite sized vortex electron's radius

Because we are revisiting the Bohr atom from the perspective of the finite sized orbiting charge model of the electron, it is useful to look at some old and well known abstract equations that can be derived from the Bohr model and its dimensions and to compare them with this finite size electron's dimensions and energy [1, 2, 3, 4, 21, 22]. That is, we will provide a physical meaning to these abstract relations.

The first is the radius of the first Bohr orbit (the ground state) which is given by two different expressions, combined here as

$$a_0 = \frac{\hbar^2}{me^2} = \frac{\lambda_c}{2\pi\alpha} \ , \tag{15}$$

where λ_c is the Compton wavelength in cm. But based on equations 1 – 4, $\frac{\lambda_c}{2\pi}$, the reduced Compton wavelength, is the radius of the revolving charge model of the electron. That is to say, we can write Eq. 15 as

$$a_0 = \frac{r_e}{\alpha} = 137.035999074\ r_e \ , \tag{16}$$

where r_e is the radius of the vortex electron. But we have previously shown in Eqs. 11 and 12 that we can write the inverse fine structure constant as $2\pi\ a_0$ when a_0 is expressed in Comptons. Using this, we note that we can write Eq. 16 in Comptons as

$$a_0 = 2\pi\ 21.809956634\ r_e = 21.809956634\ \lambda_c. \tag{17}$$

because $2\pi\, r_e$ is, by definition, one Compton. That is to say, we can express a_0 as 21.809956634 Compton wavelengths, or

$$a_0 = 21.809956634 \text{ Comptons.} \tag{18}$$

This is somewhat redundant and is a triviality, but we have previously stated that we will be expressing units of length here as Comptons, so this is illustrative of the usage of that point.

It is important to note that, Eq. 18 is defined as the distance between the center of the nucleus and the center of the electron. I.e., in all calculations below, we let the reflections take place at the surface of the nucleus while the reference point of the electron is its center.

But multiplying both sides of Eq. 15 by $2\,\pi$, we have that

$$C_{Bohr} = C_e / \alpha = \lambda_C / \alpha\,. \tag{19}$$

where C_e is the circumference of the vortex electron. Hence, the circumference of the Bohr atom's electron's is directly related to the electron's circumference by the fine structure constant.

But to expand on Equation 10 a little more, we compare Equations 10 and 16, so that we note in passing that

$$\frac{a_0}{r_e} = \frac{r_e}{r_{classical}}. \tag{20}$$

By analogy, that is as if the electron's orbit were a little Bohr orbit with its very tiny spinning charge orbiting the center of the electron.

This and Equation 10 are the spoilers in the possibility of explaining the fine structure constant in terms of the Bohr orbit as determined here using Compton wavelets. Therefore, it is beyond the scope of this present work to comment any further on it at this time.

We also note at this point that the classical electron radius is derived by assuming that the mass-energy of the electron is contained in a sphere having that radius. However, Eqs. 1 – 4 indicate an overall field of action that has a radius that $1/\alpha$ larger that the classical electron radius.

We will have more to say about this in the next section on angular momentum as well as ikn Appendix E

7 A model of the electron's angular momentum

It is also interesting to note that if the electron's mass were to be contained in its Compton orbit, the orbital momentum of vortex electron's trapped photon would be given by p = E/c, where E is the energy of the trapped Compton photon. Multiplying this by the reduced Compton wavelength, which is the radius of the electron, we have for the angular momentum [23]

$$S = \frac{h\upsilon_C}{c}\frac{\lambda_C}{2\pi} = \frac{h}{c}\frac{c}{\lambda_C}\frac{\lambda_C}{2\pi} = \hbar \tag{21}$$

This is obviously in error by a factor of 2.

In classical mechanics, if the angular momentum of a revolving ball or revolving hoop is known, then taking that same mass and spreading it out uniformly over a flat disk that revolves on an axis in its center, then the angular momentum will be divided by half [24].

Similarly, if the electron's mass is simplistically spread out uniformly over the electron's orbit as if it were a disk, then that angular momentum would be half of the value given by 21, or [23]

$$S = \hbar/2 \tag{22}$$

This is the known expression for the electron's spin momentum [25, 26, 27].

This is consistent with the claim that the mass energy of the electron is spread out uniformly within its volume, and is not contained in its charge. Obviously, any error in this model, i.e., any non-uniformity in the disk, would introduce an error into any measurement that is dependent on the angular momentum that could easily be falsely mistaken for an error in some other factor in the measurement.

There might be objections to the above, however, on the basis of the classical radius of the electron being derived on the assumption of the charge's mass energy being contained within the classical radius itself.

However, we claim here that the mass of the electron is actually spread out uniformly over the Compton wavelength orbit as indicated by the angular momentum given by Eq. 22, so that there is a contradiction between the current model and the classical electron radius model.

Ultimately, we maintain that the known angular momentum of the electron indicates that, while the classical electron radius is an extremely interesting artifact, the known behavior of the electron indicates that the mass is spread out over the Compton area, not over the classical electron radius.

We will discuss more on this later in Appendix E.

8 Some relations between the mass energy of the electron and its potential energy in its Bohr orbit

Within the context of this model, we can take the above a few steps further before discussing the wavelet interactions within the atom.

The velocity of the first Bohr orbit's electron is [21]

$$v_B = \frac{e^2}{\hbar} . \tag{23}$$

But the fine structure constant is defined as [22]

$$\alpha = \frac{e^2}{\hbar c} , \tag{24}$$

Hence, multiplying 24 by c, we find that the velocity of the first Bohr orbit may be written as

$$v_B = \alpha c = 2.1876913E{+}08 \text{ cm/sec} . \tag{25}$$

As we have previously stated in Section 6, the velocity of light is, by definition, one Compton per rotation, so we may write 25 as

$$v_B = \alpha = 7.29735265E{-}03 \text{ Comptons/rotation} . \tag{26}$$

Further, we note that we can scale the electron's rotational frequency to that of the Bohr atom's electron's rotational frequency as follows:

$$f_B = \frac{v_B}{2\pi a_0} = \frac{\alpha c}{2\pi a_0} = \frac{\alpha c}{2\pi} \frac{1}{a_0} = \frac{\alpha c}{2\pi} \frac{2\pi\alpha}{\lambda_c} = f_e \alpha^2 \tag{27}$$

where f_B is the rotational frequency of the Bohr atom's electron, αc is the velocity of the electron in its Bohr orbit, and where we used Equation 1 as the definition for f_e. Hence we have

$$\frac{f_e}{f_B} = \frac{1}{\alpha^2} = 18778.865042\ . \tag{28}$$

That is to say, for every revolution of the electron around the nucleus, the electron itself will revolve 18778.865042 times, or the period of the Bohr orbit is 18778.865042 rotations. Further, if we use our Electron Units, the period of the Bohr orbit is

$$T_B = 18778.865042 \text{ rotations.} \tag{29}$$

Note that this is not an integral value, so it does not represent quantization of any kind. I.e., it is 7.19 ppm away from being an integral value. It would also preclude the wavelets from taking part in circumferential periodicity, even if they could curve around the circumference of the first Bohr orbit.

Using the electron's mass energy as calculated by the Einstein photo electric equation in Equation 4, we scale its internal rotational energy to its orbital rotational energy in the Bohr atom using equation 28. That is, we divide the electron mass in eV by the numerical value in Equation 28 and we get

$$E_B = E_e\alpha^2 = \frac{E_e}{18778.865042} = 27.21138508 \text{ eV.} \tag{30}$$

Hence, the revolving Bohr electron's potential energy is determined by the Einstein photo electric equation just as the revolving charge of the electron provides it own mass energy.

The potential energy of the electron in the Bohr atom's ground state is

$$V_B = \frac{e^2}{a_0} = 27.21138498. \tag{31}$$

The difference between Equations 30 and 31 is 10^{-7}, i.e., 10 in the last two significant figures, which is within the measurement error of the electron's

charge, e [18]. That is, Equation 30 and Equation 31 effectively have the same value.

The Rydberg constant gives the ground state energy of the electron as [18]

$$R_\infty = \frac{m_e c \alpha^2}{2h} = 13.60569253 \text{ eV}. \tag{32}$$

But, half of Equation 30 is the same that of Equation 32. I.e.,

$$E_B / 2 = 13.60569249 \text{ eV}, \tag{33}$$

the numerical value of which is within the value 4 in the last significant digit of Equation 32, which is acceptable for claiming that 32 and 33 are equal.

We are justified in using half of Equation 30 to compare the electron's mass energy with that of the orbiting electron in the Bohr atom because of the virial theorem. However, in case of the electron itself, there is no known central force holding the electron together, so the virile theorem does not apply there and the electron's mass energy is not divided by 2.

Thus, we relate the finite sized electron's radius, velocity, and circumference to the same parameters for the Bohr orbit by means of the fine structure constant. Further, their rotational frequencies and, hence, energies are related via the square of the fine structure constant.

At the same time, we have previously stated that the electron behaves as if it were a bound state photon, and is related to a similar behavior of the revolving Bohr electron. It too, is bound, but it is bound by an electrostatic potential and it is not a light speed entity.

Or, from another point of view, the rotational energy of the Bohr electron is not an arbitrary value, but it has a definite relationship with that of the electron via the fine structure constant.

Because of the classical approach to modeling the vortex electron that we use here, we do not in any way use quantum mechanics or its concepts at this stage of its development. Hence, there is no intent to make any investigation of any wave mechanics other that of the behavior of the Compton wavelets.

9 Wavelength corrections for the Compton wavelets

The fact that the electron is in a potential well means its energy is decreased. As a result, its frequency is lowered by the ratio of the electron's energy to that of the electron mass, or by a factor of 0.99945567944/0.510998910E6 = 2.662567807E-5.

$$r = 1 - \frac{E_B}{m_e} = 0.999973374. \quad (34)$$

Hence, the wavelength of the wavelets will be increased by 1.00002662638.

This reduction in energy will increase the wavelet's lengths by the inverse of this value which is a factor of 1.000026626.

The reduced mass factor is given by

$$\mu = \frac{1}{1+\frac{m_e}{M_p}} = 0.99945567944. \quad (35)$$

Hence, the inverse of this is the wavelength correction factor, or 1.000544617006.

The total of these corrections to the wavelength of the wavelets will be the product of these, or the overall correction factor is

$$f = 1.00057125788. \quad (36)$$

Also, we must consider the size of the proton because that could be a contributing factor to the results we obtain here. Its radius, based on a revolving charge model similar to the vortex electron used here, is [28]

$$r_p = 5.8736077E\text{-}14 \text{ cm} = 0.0015210324 \text{ Comptons}. \quad (37)$$

This is the point on the nucleus from which the wavelets reflect, so it is added to the calculated value of the Bohr radius.

We make no claims regarding *t*hese correction factors beyond these for this particular model.

10 The scope of the wavelet study

We limit the scope of this part of the study to a discussion of the effects of the finite sized vortex electron, above, and models of several possible emission-impact scenarios that determine the length of the Bohr radius and, hence, the inverse fine structure constant.

Due to the complexity involved, it is beyond the scope of this current work to attempt to make numerical estimates of the electrical strength of the wavelets or the magnitude of the possible impact of the individual wavelets on the electron. Also, we will not make any attempt to model the interaction of the wavelets with the nucleus.

There is no intent here to consider any aspect of the fine structure constant outside of the one associated with Bohr orbit's dimensions as described here.

The correction factors utilized will be limited to two. The first two are the reduction in energy of the electron because it is in a potential well, and the reduced mass correction.

Finally, no quantum mechanical methods will be utilized here as they are not needed. Only a classical approach will be utilized. In spite of this, we will achieve an accuracy of 52 ppm for the Bohr radius and the resultant inverse fine structure constant. Further, any attempt to address any quantum mechanical issues adequately could prove lengthy and could be separate work in itself. Hence, it is beyond the scope of this work to address any quantum mechanical issues here other than the mention of de Broglie waves and how they arise from the Compton wavelets that we describe here.

11 A search for the mechanism that holds the Bohr electron at a minimum fixed distance from the nucleus

In the following sections, we will utilize what amounts to standing wave trains of n of the vortex electron's Compton wavelets that reflect off of the nucleus of the Bohr hydrogen atom and return to impact the electron, thus holding the electron at a minimum distance from the nucleus at a distance equal to the Bohr radius. This, of course, will also determine the value of the inverse fine structure constant as used here and as described in Eq. 16.

The value for n is an empirical integral value as chosen below.

We define our basic phenomenological model in Figure 4 for a specific scenario.

At cardinal point B in Figure 4, the charge is at 90 degrees, cardinal point C is 180 degrees, and cardinal point D is 270 degrees. The distance from the center of the electron to the nuclear center as we use it there is the first Bohr radius.

In this particular symmetric scenario, the wavelet is emitted at point C and returns to impact at point C, there being n wavelets between the emission and the impact, and this includes the impacting wavelet. We use both n = 43 and n = 44 for comparison with their values for the Bohr radius being shown in Tables I and II, below.

In addition to the scenario shown below, we will study how these wavelets interact with the electron after they are reflected off the nucleus for a number of different scenarios with the emission taking place at points A, B, and C, and with impacts taking place at A, B, and C. We do not use point D because the charge is moving away from the nucleus so it seems highly unlikely there would be emission or effective interaction at that point.

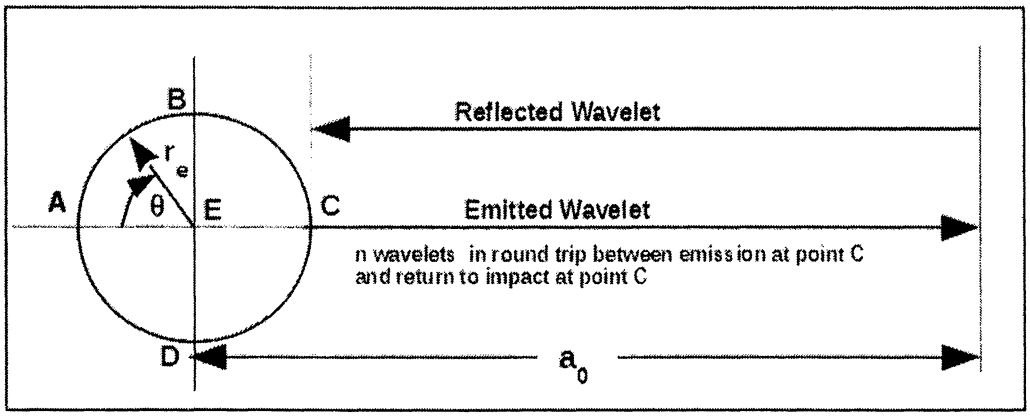

Figure 4. Here, we have a scenario where the electron's charge rotates in a clockwise direction in the circular orbit centered on point E and with a radius r_e The phase angle θ is at 0 degrees with respect to the line joining the electron center with that of the nuclear center when the charge is at cardinal point A.

12 Phase Synchronicity

Phase synchronicity is one of the criteria that we will be utilizing in the interaction of the electron with the Compton wavelets that are reflected back from the Bohr atom's nucleus.

Specifically, the Compton wavelets generated by the electron and reflected back to it by the nucleus must return in such a manner that they always interact with its charge by colliding with it at some fixed phase angle so as to prevent it from approaching the nucleus any closer than the first Bohr radius, i.e., so that Eqs. 17 and 18 are satisfied within a reasonable error.

In general, we will consider two distinct types of emission:

1. The first is where the emission of the wavelet, a longitudinal impulse as opposed to a transverse field, is perpendicular to the orbital velocity vector at point A and point C. For example, this would be an emission either at point A, or point C in Figure 4, above.

2. The second is where the emission takes place parallel to the charge's velocity vector. I.e., the second case is where the wavelet is emitted in a manner similar to that of cyclotron radiation from point B towards the nucleus. However, this emission is a longitudinal electric field as opposed to a transverse electric field (photons) that would be emitted in an actual cyclotron.

We do not consider a case of emission towards the nucleus taking place between points C and A because the charge is moving away from the nucleus, nor do we consider collisions when the charge is between these point in this particular study.

In both of these cases, the emitted wavelets will sweep around in a circle like a search light beam that travels in a straight line to cross the nucleus where it will be reflected back.

For emissions at points A and C, we consider emission and impact only when the phase angle is at precisely at 0 degrees or180 degrees for the perpendicular case. While it may be that there might be emission or impact at some fixed angle, ψ, away from these cardinal points, we do not consider them here.

For emission at point B, we consider the simple case of emission at 90 degrees.

In both of these manners of emission, however, as the wavelet sweeps outward, it travels at a finite velocity so that a stationary observer looking down of the revolving electron will see these wavelets spiraling outward like the stream from a rapidly revolving water sprinkler.

More specifically here, we require that:

1. Wavelets that are emitted towards the nucleus must always be emitted from some fixed phase angle of the electron for every rotation.

2. Each returning wavelet always interacts with the charge at some fixed phase angle of the electron.

3. The emission phase angle may or may not be same as the interaction angle of the returning wavelet, but *the phase relationship of the emission and interaction is always fixed.* We will refer to this as phase synchronicity or, simply, synchronicity.

13 Some specific scenarios that utilize phase synchronicity

As stated above, here we consider several combinations of three possible emission points and three possible impact points as described in Section 10. The results from these scenarios are tabulated in Tables I and II for comparison for both n = 43 and n = 44.

In the symmetric scenario described in Figure 4, we consider the case of a wavelet emitted at point C towards the nucleus. It travels towards the nucleus and is then reflected back and it impacts on point C after n revolutions since its emission. There are, as a result of the n rotations, n wavelets between the outgoing and returning path that goes from point C to the nucleus, and then the return trip back to point C. The Bohr radius can be calculated from the model by the equation

$$a_0 = f * \left(r_e + \frac{n}{2}\right). \tag{38}$$

This is, obviously, based on the geometry of Figure 4. This, and all of the scenarios below are tabulated in Tables I and II for comparison not only with n = 43, but n = 44.

Here, f is the correction factor (Eq. 36) for the increased radius of the electron due to its energy increase in the potential well and center of mass correction.

Another scenario, a non-symmetric scenario, would be could occur if a wavelet were emitted cyclotron radiation fashion from cardinal point B. It can return to impact at point B, or even impact at points A or C.

In the case of a wavelet emitted at point B and impacting back at point B, the +equation is trivial and is

$$a_0 = f * n/2 \, . \tag{39}$$

We do not bother with a figure for this one.

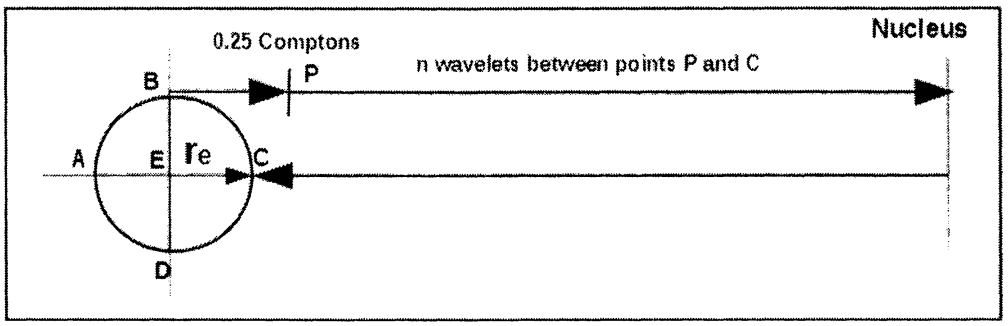

Figure 5. A non-symmetric scenario where a wavelet is emitted at cardinal point B and a wavelet in the return train will impact at cardinal point C when the charge arrives there.

In Figure 5, at the time the charge has rotated 90 degrees from point B to point C, the last wavelet emitted has moved to point P, and one of the n wavelets in the train is impacting at point C. During that 90 degree rotation period, the last wavelet emitted at B will travel 0.25 Comptons. There are some n full wavelets in the outgoing and incoming wavelet train between the point P and the point C.

In order to calculate a_0 for the scenario of Figure 5, we need to add up the entire round trip wavelet path from point B to the nucleus and back to the center of the electron, and then divide that path length by 2. That is, we have

$$a_0 = f * (0.25 + n + r_e)/2. \tag{40}$$

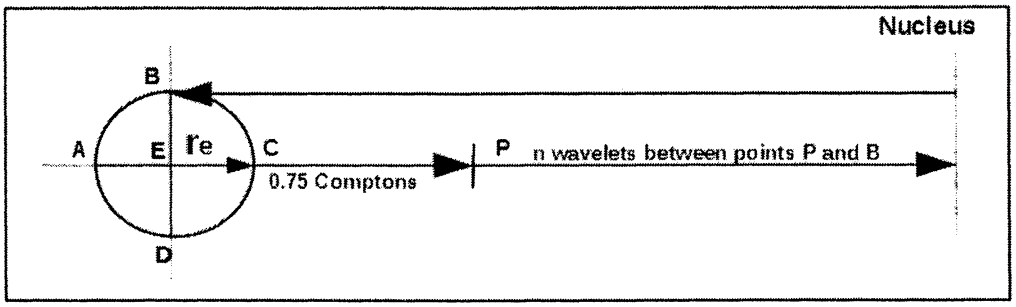

Figure 6. This is the complement of Figure 4.

In Figure 6, above, we show the case where a wavelet is emitted when the charge is at point C and the next impact occurs when the charge has rotated to point B. There, a wavelet is emitted at C and the next wavelet in the train impacts the electron when the charge has rotated to point B so that during that time, the wavelet emitted at point C travels 0.75 Comptons to point P. There are n wavelets between point P and point B.

In the case where the wavelet is emitted at B and impacts at A, there are n wavelets between point P and point B, so that the total distance of the components in the path from C to B, plus r_e, must be added and divided by 2. Hence, we have that the Bohr radius is

$$a_0 = f * (r_e + 0.75 + n)/2 \, . \tag{41}$$

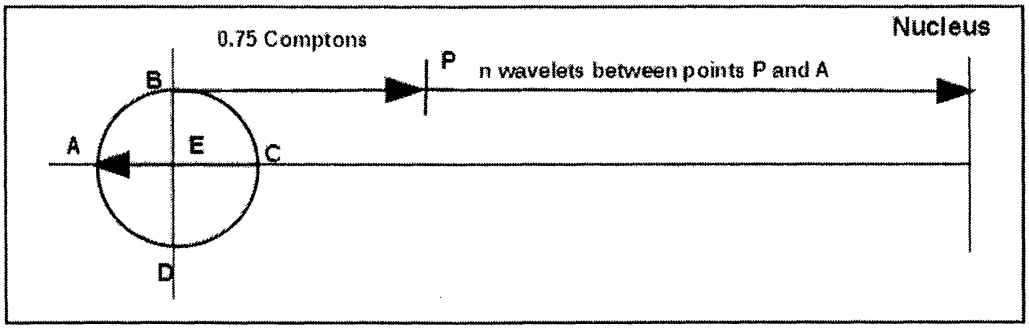

Figure 7. Here we have emission at point B and a non-symmetric impact at point A.

In Figure 7, the wavelet is emitted cyclotron fashion at point B and moves toward point P during the 270 degree rotation of the charge to point A, so the charge moves 0.75 Comptons in order to arrive at point P. Between point P and point A, there are n previously emitted wavelets. When the charge reaches point A, one of those n previously emitted wavelets will impact the charge.

There, the 0.75 Compton wavelet plus the n wavelets move the wavelet train to point A and provide the Bohr radius as

$$a_0 = f * (0.75 + n - r_e)/2. \tag{42}$$

Here, we subtract r_e from the entire wavelet train to obtain the Bohr radius.

Note that Figure 7 and Eq. 42 describe the scenario that gives the best fit to the known Bohr radius.

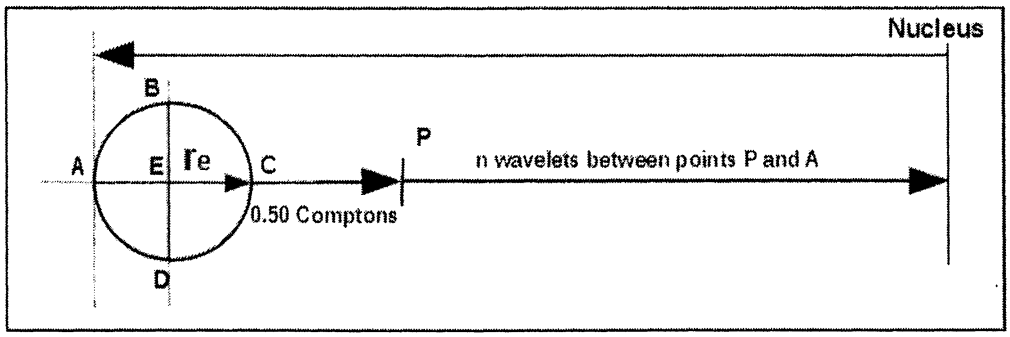

Figure 8. The wavelet is emitted at point C and returns to point A.

In Figure 8, the charge's round trip from C to A is 0.50 Comptons, so that that is the amount the wavelet moves from C to P before a wavelet impinges on point A.

For the scenario of Figure 8, the Bohr radius is given by

$$a_0 = f * [(2r_e + 0.50 + n)/2 - r_e]\,. \tag{43}$$

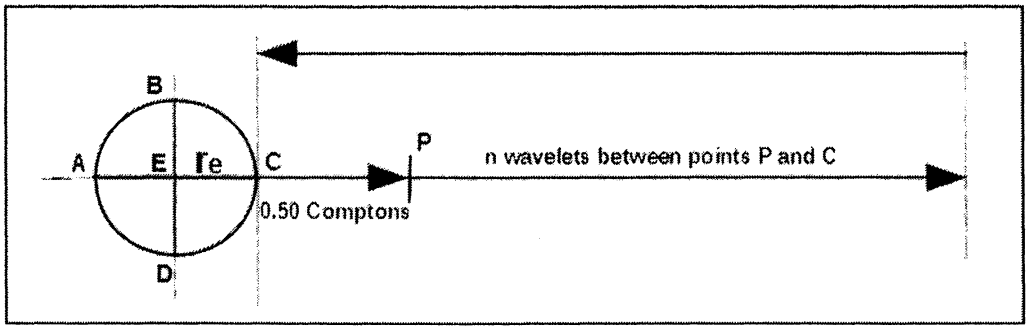

Figure 9. This is the complement of the scenario of Figure 8. A wavelet is emitted at point A and returns from the nucleus to impact the electron at point C.

The Bohr radius for the scenario of Figure 9 is given by

$$a_0 = f * [(0.50 + n + 2r_e)/2 - r_e]. \quad (44)$$

.

Table I. This provides a summary of the equations for all of the above scenarios.

Emission Point	Impact Point	Bohr Radius Equation
A	A	f(n/2 - r_e)
A	B	f((0.25 + n + 2r_e)/2 -r_e)
A	C	f((0.50 + n + 2r_e)/2 -r_e)
B	A	f(0.75 + n - r_e) / 2)
B	B	f(n/2)
B	C	f((0.25 + n + r_e) / 2)
C	A	f((2r_e + 0.50 + n) / 2 - r_e)
C	B	f((0.75 + r_e + n) / 2)
C	C	f(r_e + n / 2)

In Table II and Table III, below, we have collected the data from all of the possible scenarios for emissions and impacts on cardinal points A, B, and C.

This includes several scenarios not shown above. This table includes the equations and the cases where n is both 43 and 43 wavelets. We also show the fractional error for each scenario and for both 43 and 44 complete wavelets for these scenarios.

Table II. The Bohr radius equations, the Bohr radii, and the errors for a number of emission-impact scenarios with two possible values of n for emission from and impacts on cardinal points A, B, and C. Not all of these were diagramed, above, however. Note that we multiply the formulas shown below by f from Eq. 36. Then, we add the nuclear reflection point, r_p from Eq. 37, to the radial value. (It is not explicitly shown because of room). Here we use six decimal values so that we have three significant figures in that value with the least error, scenario B-A.

Emission Point	Impact Point	a_0 (43) (Cmptns)	a_0 (44) (Cmptns)	Delta(43) (Cmptns)	Delta(44) (Cmptns)
A	A	21.354557	21.854843	-0.455399	0.044886
A	B	21.638874	22.138579	-0.171082	0.328622
A	C	21.763946	22.262710	-0.046011	0.452754
B	A	21.809394	22.309099	-0.000562	0.499142
B	B	21.513803	22.014089	-0.296154	0.204132
B	C	21.717916	22.218202	-0.092040	0.408245
C	A	21.763946	22.264232	-0.046011	0.454275
C	B	21.968640	22.468345	0.158684	0.658388
C	C	21.673049	22.173335	-0.136908	0.363378

Table III. The fractional error is shown for all scenarios for both the 43 wavelets and 44 wavelet cases for the scenarios of Table I. In addition, we show the calculated value of the inverse fine structure constant based on the 43 wavelet case since that appears to be the most accurate. Note that the fractional error for the B-A scenario is 26 ppm without corrections. Emission from point B is cyclotron-like emission.

Emission Point	Impact Point	a_0 (43) (Fraction)	a_0 (44) (Fraction)	1/alpha (Comptons)
A	A	-0.020880	0.002058	134.174640
A	B	-0.007844	0.015068	135.961058
A	C	-0.002110	0.020759	136.746905
B	A	-0.000026	0.022886	137.032466
B	B	-0.013579	0.009360	135.175211
B	C	-0.004220	0.018718	136.457693
C	A	-0.002110	0.020829	136.746905
C	B	0.007276	0.030188	138.033038
C	C	-0.006277	0.016661	136.175783

14 The effects of finite wavelet widths

In addition to the lateral angular error, we must consider the possibility that the wavelet's width could have an effect on the error. That is to say, if the wavelet has a finite width and the charge interacts with the edge of the wavelet rather than the infinitely thin wavelet that we have used for the calculations, then then the delta values of Table II would be half of this wavelet width for the 43 wavelet case of Table II. Using the edge of this wavelet would produce exactly the actual Bohr radius with no error.

In Table IV we calculate what the width of the wavelet would have to be for the 43 wavelet case in order to obtain complete agreement with the experimental value of the Bohr radius. I.e., for the A-C case, it would have to be 0.092021 Comptons wide in order for its edge to impact the electron's charge at cardinal point C when it's wavelet center is at 21.763946 Comptons from the nucleus.

As a result of the widening of the wavelet, at some distance away from the electron the wavelet would become so wide that adjacent wavelets would merge, thus causing the de Broglie wavelength to become confused so that the de Broglie model of Section 5, above, would begin to collapse.

Table IV This shows the width of the wavelet that would be required for the edge of the wavelet to impact the charge while maintaining the known value of the Bohr radius. It is shown for each scenario including the C-B scenario where the calculated Bohr radius is larger than the known value. However, we note that is numerical value is within 5 ppt of the inverse fine structure constant. While it is most likely that this is nothing more than a coincidence, it is left here for further examination in some other future work on the off chance that it may have some meaning.

Emis-sion Point	Impact Point	a_0 (43) (Comptons)	Wavelet Width (Comptons)	Slope	Merge Point (Comptons)
A	A	21.354557	0.910799	0.021169	47.238273
A	B	21.638874	0.342164	0.007907	126.473472
A	C	21.763946	0.092021	0.002114	472.985733
B	A	21.809394	0.001125	0.000026	38927.281056
B	B	21.513803	0.592307	0.013767	72.638945
B	C	21.717916	0.184081	0.004254	235.085773
C	A	21.763946	0.092021	0.002114	472.985733
C	B	21.968640	-0.317367	-0.007334	-136.355326
C	C	21.673049	0.273815	0.006364	157.129824

In order to find this merge point, we calculate a slope referenced to the first Bohr radius. Because the charge diameter is extremely small compared with the electron radius, we start out with a wavelet width of zero at the emission point, and it becomes wider from there as it moves away from the electron. The slope is shown in Table IV.

Using this slope, we calculate this merge point for each scenario, and it too is shown in Table IV.

15 Binding Energy and Relativistic Corrections

Because the error is so small, it is useful to see if a relativistic correction is useful.

In equation 4, we note that if we multiply the Compton wavelength by the Lorenz contraction, we have

$$E_e = \frac{hc}{\left(\sqrt{1-\frac{v^2}{c^2}}\right)\lambda_C} = \frac{mc^2}{\sqrt{1-\frac{v^2}{c^2}}}. \tag{45}$$

That is to say, the radius of the electron appears to have a uniform contraction as the velocity increases. And while it would be expected to contract only in the direction of travel, we speculate that because of the nature of its light speed particle, it contracts uniformly, not elliptically. In any case, this is consistent with experiment, so we claim that the radius and Compton wavelength both contract in the same proportion when the electron is accelerated.

Using the relativist correction to the Bohr electrons radius and its Compton wavelets would be given by

$$rc = \sqrt{1-\left(\frac{\alpha c}{c}\right)^2} = 0.999973374\,. \tag{46}$$

This amounts to a fractional correction of 2.6626E-05, or 27 ppm. When this is applied to the Bohr radius of scenario B-A, its length becomes

$$R_0 = 21.8088133 \text{ Comptons.} \tag{47}$$

which is in now error with experiment by 52 ppm.

16 Electron-wavelet Synchronization

Here, we wish look for some possible means by which the electron holds itself at some 43 wavelets round trip from the nucleus as opposed to 42, 44, or some other integral number of compete wavelets.

At the same time, wish to look some means of providing an integral number of Compton wavelets that will be consistent with Eqs. 5 – 7.

In the simplest case, the round trip time for a Compton wavelet to travel from the center of the electron and then echo off of the nucleus is

$$t_r = \frac{2a_0}{c} \tag{48}$$

Using αc for the velocity of the electron in the first Bohr orbit, the distance the electron moves in that length of time is

$$d_e = \alpha c \frac{2a_0}{c} = 2\alpha a_0 = 2\alpha \frac{\lambda_c}{2\pi\alpha} = \frac{\lambda_c}{\pi} \tag{49}$$

This, however, is just the diameter or the electron. I.e., the electron emits a wavelet towards the nucleus and travels one diameter in the period of time it takes for the wavelet to return and interact with it.

The number of electron revolutions in that time are

$$n_e = t_r f_e = \frac{1}{\pi\alpha} = 43.619913 \tag{50}$$

However, each revolution creates a wavelet, so that expressing the round trip time using the B-A scenario's radius, so that

$$n_e \text{ [B-A]} = 43.6176266 \tag{51}$$

This is in error with respect to Eq. 50 by -52.4 ppm.

This, however, does not explain quantization nor does it necessarily imply that there are an integral number of rotations of the electron in its entire trip around the nucleus, so that using this methodology for deriving a de Broglie wavelength for the circumference is problematic.

Based on the finite size of the electron and the definition of a de Broglie wave as given above, we would expect that either an integral number of electron diameters would be required as the electron transits a single orbital circumference, or an integral number of rotations of the electron would be required. We will explore these possibilities first with the standard definitions normally associated with the single electron atom, then with the reduced mass, and finally, determine a Bohr radius that will provide us with these required spatial and rotational periodicities.

Using this, the circumference of the first Bohr orbit is

$$C_0 = 2\pi a_0 = \frac{\lambda_c}{\alpha}. \tag{52}$$

The diameter of the electron, whose circumference as defined above is λ_C, has a diameter given by

$$D_e = \frac{\lambda_c}{\pi}. \tag{53}$$

Hence, the number of electron diameters in the circumference of the first Bohr orbit is

$$n = \frac{C_0}{D_e} = \frac{\pi}{\alpha} = 430.246810445298 \tag{54}$$

This is some 574 ppm from being an integral number.

Dividing 360 degrees by the value in Eq. 54 gives us

$$\theta = 0.8637290 \text{ degrees.} \tag{55}$$

for the angle subtended by an electron at the nucleus. (This is an incidental number with no particular significance at this time.)

Using the Rydberg constant of Eq. 31, we calculate the wavelength of the maximum Lyman photon as

$$\lambda_{\text{Lyman}} = 9.112669970\text{E-}06 \text{ cm.} \tag{56}$$

In Comptons, this is

$$\lambda_{\text{Lyman}} = 37557.72787644 \text{ Comptons.} \tag{57}$$

Clearly, this is much larger that the size of the Bohr atom. But it is also interesting to note that if we divide Eq. 57 by 2, we get

$$\lambda_{\text{Lyman}}/2 = 18778.863938 \text{ Comptons.} \tag{58}$$

Numerically, this is within 58 ppb of the value in Eq. 28, but is in units of length, not a ratio of frequencies as is Eq. 28.

If we divide Eq. 56 by the Bohr radius, we have

$$x = \lambda_{Lyman} / r_0 = 1722.045052. \quad (59)$$

Hence, the photon's length is much bigger than the Bohr radius.

The photon's time period in seconds is

$$\tau_{Lyman} = 3.039659513E\text{-}16 \text{ sec.}, \quad (60)$$

Its time period in rotations is

$$\tau_{Lyman} = 3.755772790E+04 \text{ rotations.} \quad (61)$$

But dividing 61 by 2, we have again

$$\tau_{Lyman} / 2 = 18778.86395 \text{ rotations.} \quad (62)$$

That is to say, the half period of the photon is equal to a single rotation of the Bohr electron. Just what the significance of this is, if any, is not clear at this time other than an incoming electron will start to spiral into the nucleus because of the emission of radiation.

We will have more to say about this in Appendix A where we describe a simulation for a hypothetical electron approaching the nucleus, but being constrained to move in a straight line without radiating. In that case, it moves from a radial distance outward of 15 Bohr radii to the first Bohr radius in 1760 rotations, which is extremely small as compared to Eq. 61 or 62.

17 The B-A scenario and a possible vortex electron radiation model

The B-A model had 52 ppm accuracy after its lateral emission correction. That is to say, the wavelet was emitted at the 90 degree point, reflected and impacted the electron at the 0 degree rotation point. This is somewhat counter intuitive, but nonetheless the accuracy of this scenario as opposed to the others cannot be ignored. Therefore, we must provide a reasonably rational explanation.

The first and most obvious explanation is that the wavelet impacts the charge from inside the electron as it travels past its center and to the periphery.

However, we speculate that another possibility is that at this particular radius and phase, the reflected wavelet suppresses the ability of the electron to radiate. But in order to explain this, we must explain why the vortex electron radiates in the first place. So, to begin, see Figure 11.

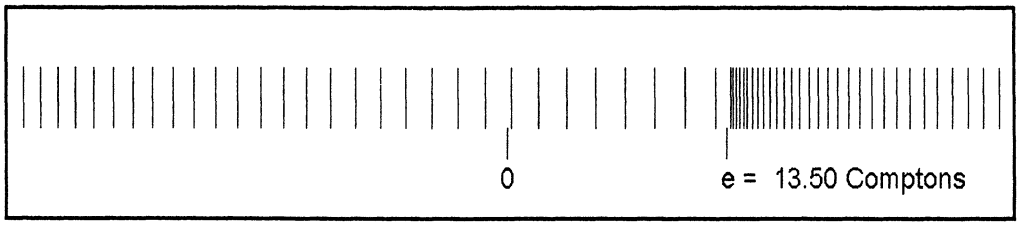

Figure 11. The Compton wavelets along the path of an electron that is being accelerating rapidly and linearly towards the right from a velocity of zero up to 0.9c in 30 rotations, where c is the speed of light. It starts from where the electron center is at point 0 up to the point e, where e is the center of the electron an instant of time before emission in the direction of travel. These accelerations and wavelet counts were chosen for illustrative purposes.

We note in Figure 11 that as the electron is accelerated towards the right, the Compton wavelets in front of it are compressed and those behind it are decompressed. We define the compressed waves in front of the electron as the frontal wavelets and the decompressed wavelets in back of the electron as rearward wavelets.

As a result of the compression-decompression, there is a differential field across the finite extent of the electron (and beyond) in its direction of travel, this differential field increasing as the electron accelerates. This increasing electric field then generates an electromagnetic wave, or photon.

It is also to be noted, as an aside, that it is a longitudinal electric field in that it is moving in the direction of its electric field vector. Nonetheless, it is a changing electric field, so it would be expected to radiate. We make no further comment on this phenomena at this time.

We also note that, as the electron approaches relativistic velocities, its radius contracts causing its frequency to increase and its Compton wavelets to become even more compressed. We do not show that in Figure 11, however.

For convenience in this particular case, we limit this model to the case where the motion is parallel to the electron's plane of rotation. This does not exclude other possibilities, however. (See the case of 2D emission around the circumference of the orbit in Appendix C.)

The most likely mechanism that prevents the electron from approaching the nucleus that we propose here is that when the electron reaches this particular radius, i.e., the first Bohr radius, then the reflected compressed frontal wave overlays the rearward, decompressed wavelets emitted by the electron increases the field strength on the back side of the electron. At this particular radius, the field strength of the reflected wavelets sufficiently neutralizes the radiative field across the electron so as to prevent it from radiating its energy away and approaching the nucleus any further.

More specifically, as the electron revolves at the first Bohr radius, it is constantly being accelerated towards the radius so that the wavelets are slightly compressed on the nuclear side of the electron and decompressed on the outward side. The reflected wavelets have the same ratio of compression/decompression, but are in the opposite direction, and hence, combine with the backside wavelets to increase the backside radiation so as to cancel the radial field across the electron.

Obviously, this is still speculative until such time as adequate simulation and analysis is available to provide some numerical validity to the model. It does not preclude the possibility that a wavelet-charge impact is the actual mechanism. In any case, however, this scenario gives a more accurate agreement with experiment than do the other scenarios.

18 Discussion of data

In Table II, the scenario with the smallest fractional error is that where the wavelets are emitted cyclotron fashion at point B and impact back at point A (the B-A scenario), and whose calculated value of the first Bohr radius is 52 ppm smaller than the known value. In fact, the contrast in its error and those of the other scenarios is so considerable that it is clearly the most viable option in the entire set of scenarios. However, this value does not rigidly validate the model described here, but it is strongly suggestive that the model is valid.

It should be noted that at point A, the wavelet is being emitted perpendicularly to the Bohr radius, so it is parallel to the wavelet being reflected from the nucleus.

What we cannot say here, however, is what the mechanism is that holds the electron at this minimum orbit. We cannot say if it is due to impact by the reflected wavelets on the charge, or if it is due to the suppression of radiation by the reflected wavelets.

We suspect that it is the latter because the outward force of the reflected wavelets are likely relatively small in strength compared to the attraction of the nucleus, so that as the electron approaches the nucleus, the reflected wavelet field becomes strong enough to cancel the differential electric field across the electron.

Obviously, this warrants considerably more investigation.

However, the accepted value of the Bohr radius is known to 11 significant figures, so obviously more development is needed in order to improve the accuracy unless, of course, the above model of a finite width wavelet should be valid correction factor.

At the same time however, we have discussed the possibility that the effects of the finite width of the reflected wavelet could mean that the methodology is exact. However, we only state that this is a possibility at this time, and the methodology must have considerably more investigation before any conclusions are made.

Another factor that we must consider is the size of the nucleus. Its diameter is approximately 0.003 Comptons. It will be noted that all of the wavelet widths, above, are much greater than the diameter of the nucleus except for the B-A scenario wavelet. Hence, for the wider wavelets, only a small part of their field is reflected back to the charge and would be less likely to have enough impact to hold the electron back from the nucleus.

But for the B-A scenario, the wavelet width, as it sweeps searchlight-like across the nucleus, is one third the size of the nucleus, or even less. This would imply that a large amount of the wavelet's field is reflected back from the nucleus to the electron and that the field would then drop off in intensity with an inverse square law. This is unlike the case of the other scenarios where the width of the beam is considerably wider than the nucleus. This case would entail a considerable loss of the impinging field, which, on top of the inverse square law, would mean that the reflected wavelet impact on the charge would be very small.

The wavelets for the A-C and C-A scenarios, the next best accuracies, have a finite width that is greater than the size of the charge, so it appears to spread out slightly as a function distance from the emitting electron, thus decreasing its intensity. However, we do not know what its rate of decrease perpendicular to the charge's orbit is. We will, for the time being, simply say that its overall intensity drops of as $1/r^x$, where r is the distance from the nucleus and x is some finite value greater than zero, but less than 2.

Hence, as the as the electron moves closer towards the nucleus, the reflected energy impacting it will be increased with a combination of an inverse square low and a $1/r^x$ law, or a resultant $1/r^{(2+x)}$ law. That is, its repulsive intensity will increase more rapidly than will the attractive force of the nucleus on the electron, the latter being an inverse square law. As a result, a point will be reached at which the attractive and repulsive forces are in balance.

Here, we will only make a qualitative statement about the amount of wavelet reflected back to the electron's charge. It is beyond the scope of this paper to study the impacting phenomena in any detail.

As previously stated, we must consider the possibility that the electron is not held at a minimum orbit by impact force, but might, instead, be held in place by the suppression of radiation by the neutralization of the electron's radiating field by the reflected wavelet field.

Also, another thing we are not able to do at this time is to relate the data obtained here to the fact that the Bohr atom's angular momentum is quantized in units of $\hbar$. Whatever the mechanism is, however, it is an indirect mechanism in that the likelihood of emitted wavelets curving around the orbit would seem to be rather small.

Another point to be made is that whatever model is ultimately proven the valid model, it has to be valid for the electron's spin up or down orientation with respect to the rotational vector of the Bohr electron.

Finally, it was a surprise is that the emission and impact points are different for the most accurate scenario, the B-A scenario. A more likely scenario, a priori, would have seemed to have been the case of emission from point C and impact at point C, but that scenario proved to be far less accurate than the B-A scenario.

19 Other possible sources of error

There are multiple factors that could contribute to the errors of some of the other scenarios in Table II. These include possible effects on the length of the

Compton wavelength due to its penetration into a deeper and deeper potential well as it approaches the nucleus. This also includes a possible compression of the negative wavelets as they descend into the positive potential, or on the other hand, a possible widening due to the decreased energy. We cannot say at this point without further information and analysis.

Further, at this stage of development, we cannot exclude the possibility that a severe correction to the wavelet train length would not cause another mode from Table I to prove to be more accurate. However, we have no reason to explore this possibility here.

We do not know any details about the wavelet's reflection mechanism off the nucleus or other interactions with the nucleus that may occur.

It is also beyond the scope of this work to estimate the field strength of the reflected wavelets as they impinge on the electron.

20 Some unresolved issues

In this wavelet model of the first Bohr radius, its dimension is based on the balance point between the nucleus' attractive force and the interactions of the reflected wavelets. How this, in turn, results in the Bohr condition that specifies that the electron's angular momentum must be quantized in integral values of $\hbar$, is not specifically accounted for here.

The radius of the electron itself and its orbital radius in the Bohr atom are related by the inverse fine structure constant. Exactly how this relates to the balance point between the nucleus' attractive force and the impact of the reflected wavelets is still unclear.

The physical meaning of the inverse fine structure constant relationship between the radius of the vortex electron and the classical electron radius is not understood.

In fact, insofar Eqs. 10 and 20 that contain the classical electron radius are the spoilers that make it difficult to relate the first Bohr radius to anything else by some coincidental geometric relationship between the Bohr orbitals radius and the electron's radius.

The utilization of Compton wavelets as a basis for de Broglie waves as described in Eqs. 5, 6, and 7 would appear to be functional only for straight line interactions. That is to say, Compton wavelet interactions pose no particular issues for the straight line transit from the electron, to the nucleus, and then back to the electron as we have discussed here.

In order for the linear de Broglie waves we describe here to produce integral numbers of de Broglie waves in the circular Bohr orbits, we would need to provide a mechanism that would cause the Compton wavelets to propagate in a circular orbit. That would require wavelets to be attracted by the nucleus, which would seem to be unlikely. That is unlikely because the wavelets are electric fields, not charges that would normally be expected to be the agents that interact with the fields.

Further, while the de Broglie wavelengths (Eqs. 5 – 7) appear to originate in the interaction of the Compton wavelets, the question that must be asked is, how do we get from these straight line entities we described here to the Schrodinger equation, which is a spherical wave equation?

Of course, there is also the Dirac equation. How do we relate this model to the Dirac equation in which the Bohr magneton arises from a relativistic matrix methodology?

All we are able to do at the moment is to note that Messiah provides the amplitude and time period for the Dirac Zitterbewegung frequency [29].

The amplitude, in CGS units, is given by

$$A = \frac{\hbar}{2mc}, \tag{63}$$

which is half the radius of the vortex electron. This is consistent with the projection of the radius of the revolving vortex electron onto a linear axis, and this would produce a sine wave over time. However, how we could reconcile the anomalous factor of 2 with the current model is not clear.

The CGS period is given as

$$T = \frac{\hbar}{2mc^2}, \tag{64}$$

which is the same as the reciprocal of Equation 1, except that it is divided by 4π. I.e., it is the rotational period of the vortex electron divided by 4π, which is to say that the Zitterbewegung frequency is 4π greater than the rotational frequency of the vortex electron. Again, as in the case of the amplitude anomaly, we are not currently able to reconcile the anomalous 4π factor with the vortex model.

Beyond this, either the Schrodinger equation or the Dirac equation would require an extremely extensive study by themselves, so any further comment on them beyond the above are outside the scope of this present study.

We should also consider what happens to the mix of wavelets emitted by the moving electron. Perhaps it is not farfetched to compare it with a moving aircraft emitting side scanning radar signals, or synthetic aperture radar. On top of that, there is the interference pattern added by the frequency shifted reflection and scattering from the nucleus.

For the single electron atom, there is likely little effect outside of the reflected, frequency shifted wavelets impinging on the electron as already discussed. But in the case of a multiple electron atom, the effect might become much more interesting.

While a simulation of these phenomena could be possible and certainly interesting, it could be rather laborious and extensive.

Finally, there remains the question of the internals of the electron. Specifically, what maintains the electron's charge in its light speed orbit in the absence of a central field? We claim that, in spite of the lack of a known mechanism for holding the electron together, we present enough evidence here, in the form of a whole picture, to establish a reasonable validity of the vortex model. Nonetheless, we also recognize that, at some point, we need to understand the mechanism that holds the electron's charge in its light speed orbit.

These are questions for which we propose no answers at this time. In fact, each issue discussed above could well be the subject of a complete study in itself.

21 Summary and conclusion

In this study, we have devised a novel method for describing a possible fundamental mechanism that maintains the Bohr electron in the hydrogen atom at its known minimum orbit, namely, at the first Bohr radius, a_0.

Specifically, we utilized a standing Compton wavelet methodology for maintaining the Bohr atom's electron at a_0.. This calculated value is within 52 ppm of the experimental value, and the resultant inverse fine structure constant is also accurate to within 52 ppm of the known value.

In order to obtain these values, we utilized a previously developed, finite sized vortex electron model. That model was based on a tiny charge that revolved in a light speed Compton wavelength orbit. The validity of that

revolving charge model was indicated by the fact that it provided the Bohr magneton and the electron's mass energy, identically.

We also noted that in order for the electron to have an angular momentum as given by Eq. 22, the mass energy must be spread uniformly across the area of the Compton orbit.

A simple logical extension of this revolving charge model gave rise to a dynamic field of waves surrounding the electron with these waves having a Compton wavelength spacing between them. We called these waves Compton wavelets. That was as opposed to a simple, continuous and static gradient field that would arise from a simple static point charge.

These Compton wavelets gave rise to de Broglie waves when those emitted by two moving electrons cross.

In order to utilize that vortex model in the Bohr hydrogen atom, we studied different scenarios with different trains of the revolving vortex electron's Compton wavelets that were emitted in the direction of the nucleus. Different cardinal emission points on the electron and different cardinal impact points on the electron were used. These wavelets, after emission, would then reflect off of the nucleus of the Bohr atom and then return to the electron in such a manner as to synchronously interact with it. A train of some 43 wavelets in total are in transit between the electron and the nucleus, and then back between the nucleus and the electron.

At the same time, it was found that during the time it takes for the emitted wavelets to go to the nucleus and return to impact the electron, the electron has moved one diameter. In this time period, of course, it has rotated and been impacted by the wavelets some 43 times. The significance of this one diameter movement in this time period is not obvious at this time.

In developing this model, we also showed that several parameters of the Bohr atom can be related to those of the length of the finite sized vortex electron's radius by the inverse fine structure.

At the same time, we note that in view of Eq. 19, the fact that the circumference of the Bohr orbit is related to the electron's internal charge's orbital circumference (the Compton wavelength) by the fine structure constant can only be described as mysterious. In fact, we had hoped that this would give a clue as to the origin of the fine structure constant, but this did not turn out to be the case.

In turn, the vortex electron's radius is related to the classical electron radius by the fine structure constant.

While many of these relations have been well known since the early days of quantum mechanics, they are usually viewed as being abstract numbers. While these relations were not necessary for determining the Bohr radius, their utilization with a finite sized electron provides a different concept of their behavior by providing them with a physical rationale.

We also showed how the mass-energy of the electron was related to the potential energy of the first Bohr orbit. These were related via the square of the fine structure constant in Eq. 30.

Another fine structure constant we calculated here is shown in Eq. 12. I.e., it can be obtained from the first Bohr radius simply by multiplying by it 2π, which is also the circumference of the electron's orbital circumference. However, this is on condition that the first Bohr radius is expressed in units of Comptons, so that in this case it is no longer dimensionless. Hence, it is a triviality once the Bohr radius is determined.

But Equations 10 and 20 are the real spoilers that demonstrate that we will not be able to explain the origin of the fine structure constant simply on the basis of the Compton wavelet's interaction with the Bohr atom's electron. That is to say, the numerical relationship between the revolving electron's radius and the classical electron radius take the fine structure constant one level beyond the Bohr atom.

Hence, just why it works out with these numbers in the manner that it does requires further investigation into the physical aspects of the model. Therefore, In spite of the interesting numerical relationships we have addressed, there are still some unresolved issues with the fine structure constant that must be addressed at some future time.

But to move onto the primary objective of this work, we have investigated a possible mechanism that maintains the Bohr electron at its fixed minimum radius. This was obtained when we described a fixed phase for a Compton wavelet emission point with respect to the angle between the electron's charge and that of the Bohr radius. This wavelet then traveled to the nucleus and was reflected back to the electron. Then, the reflected Compton wavelets impacted at a different but fixed phase angle of the vortex electron's charge on impact. Although the emission and impact points are different, their relative phases are fixed so that they have a synchronous relationship.

Specifically, in the case of the bound electron we studied here, we obtained the most accurate fit to the known value of the Bohr radius when the wavelet was emitted in a cyclotron like manner. After emission, it reflected back from

the nucleus and then it interacted with the electron when the charge is on the backside of the electron. That is, it impacted at an internal perpendicular point on the orbit, specifically at point A, as the wavelet was about to pass from the interior of the electron through the orbit, and then out of the electron's orbit. A total of 9 different combinations of emission points and impact points were tried and compared, but this particular combination's fit to experiment was some 40 times better than the best of the others.

Regardless of whether or not the emission and impact points are the same, there is still a fixed phase relationship between them. Hence, synchronicity is not violated.

As to how this particular impact at point A could have an effect, it is possible that it is a simple impact of a wavelet on a charge as the wavelet passes from the interior of the electron to the exterior. However, because the reflected energy off the tiny nucleus would seem to be rather small, we suspect another mechanism may be in play.

Specifically, we have shown how an accelerating electron possibly radiates during accelerating by creating an increasing differential electric field across its velocity vector, and when the denser reflected field overlays the less dense field on the backside of the electron, increases the field on the backside of the electron so that it neutralizes the electron's ability to radiate its energy away and, thus, it is not be able to further approach the nucleus.

While we considered the possibility that the reflected wavelet might not be holding the electron in place by impact on the electron point A, we speculate that suppression of the electric field is the more likely.

In this process, the electron moved one electron diameter along the Bohr orbit between the emission of a particular wavelet and the impact of that particular wavelet on the electron. However, it is not clear at this time what the significance of this is, if any.

But just as important as determining the length of the Bohr radius, the very methodology used to determine it has provided a plausible demonstration that the electric field around an electron is not a simple static gradient arising from a simple point charge, but it is, instead, a dynamic, spiraling field similar to that which gives rise to the electron's de Broglie waves in the electron-electron interaction. These wavelets, in turn, likely provide the fundamental basis for quantum mechanics.

Insofar as the nature of the mechanism that determines the Bohr orbit's radial dimension is concerned in terms of the number of integral numbers of wavelets,

we state that in the case of the B-A scenario, this distance likely has the particular value that it has because it is the balance point at which the narrow beam of reflected wavelets.

The nucleus will likely scatter the reflected wavelet, diminishing even more than the inverse square law. Hence, the wavelet strength going towards the nucleus is reduced by $1/r^2$, and the reflected wavelength will be reduced even more. For this, we will guess that it comes back to the nucleus diminished by some $1/r^{(2+x)}$ where $0 < x < 2$, so that a critical point is reached where a balance point is reached such that the first Bohr radius is reached.

But in having said this, we must also recall our earlier statement that in the round trip to the nucleus and back, the electron moves one diameter along the Bohr orbit.

The Bohr radius model of the electron-wavelet interaction, however, be different from the electron-electron interaction that arises from the previously mentioned model of the vortex electron's de Broglie waves (Eqs. 5 – 7). Wavelets emitted directly by two nearby electrons would likely experience much stronger fields that that resulting from the reflection off of a tiny nucleus, so we must consider the possibility that emission and impact points might be different from case within the Bohr atom.

To be more specific, in the case of free electrons interacting with other free electrons, it initially seemed intuitively logical that the wavelet would be emitted perpendicularly to the direction of the orbital velocity. That is, the emission should be parallel to the charge's orbital radius. Then, when the electron interacted with the wavelet, that interaction would have been expected to occur when the charge's radius was antiparallel to the oncoming wavelet. In the terminology used above, it would have been emission from and then impact on the electron at point C. I.e., the effective impact would occur only when the wavelet impacted the electron head on and perpendicularly at the electron's orbit.

That is to say, we do not assume that the mechanism of electron-electron de Broglie interactions via wavelets need be precisely the same as the interactions between the reflected wavelets of the Bohr model. That is, there could be more than one mode of wavelet-electron emission and interactions.

In the development of this model, we found it useful and, indeed, necessary to defined some convenient and natural units of measurement for this study that were related to the finite sized electron. This was done in order to provide a clearer physical picture of this model. These units were Comptons for length,

rotations for units of time (a rotation being the rotational time of the vortex electron), and Comptons/rotation for velocity, and the mass of the electron, em, for the fundamental mass. We defined a unit of force as that force required to accelerate the electron mass by one Compton/rotation^2. That force we defined as an electrodyne. The unit of work we will define as one electroerg. It occurs when a unit of force is exerted over a distance of one Compton. This system of units we referred to as "Electron Units".

Further, we currently know nothing about the interaction of the wavelets with the nucleus during the reflection process. There may be time delays that might occur in the reflection that would cause additional errors or corrections. It is even conceivable that they could be so severe as to invalidate the B-A scenario with 43 wavelets and cause another scenario with a different number of wavelets to have and increased plausibility. However, we judge that the chances of this latter condition are quite remote.

Nonetheless, in spite of these difficulties, we believe that this methodology provides a method for ultimately explaining the specific origin of the de Broglie wavelength of the first Bohr orbit.

We have specified several specific unresolved issues with this model, each of which could be the subject of a long study in itself.

Also, it is beyond the scope of this study to utilize any aspect of quantum mechanics outside of the mention of de Broglie waves. We do state, however, that quantum mechanics is ultimately based on the utilization of the de Broglie wavelength. We claim to have shown has it has its fundamental origin in the phase relationships of Compton wavelets. However, we utilize the wavelets in a totally different manner from quantum mechanics in this particular model. Here, we utilize rudimentary Compton wavelet mechanics directly and we define that basic methodology here.

It is also important to note at this point that quantum mechanics has proven to be extraordinarily successful and accurate in its description of atomic physics. But since quantum mechanics is based on the existence of de Broglie waves, which we have shown to be external to the electron, we strongly question whether it is the optimal method to use in the study of the internals of the electron and even, perhaps in the external near field of the electron. That is to say, the near field region of a particle and its internals would be a subquantum mechanical zone. But having said this, outside of the simple classical approach we have used here and in other places [28, 30 – 31] , we cannot offer any other approaches than the classical approach we use here.

As to a specific point, we are not able, as yet, to provide a specific cause of the quantized angular momentum of the Bohr atom based on the model above. Nor are we able to directly relate the de Broglie wavelength around the curvature of the electron's orbit. The latter would require an integral number of Compton wavelets in the orbital circumference, but according to Eqs. 12 and 19, the number of Compton wavelengths in the Bohr atom is not an integral number. In order to relate the current work with those parameters, we will need a better expression for the inverse power falloff of intensity of the emitted wavelets, among other things. We will not speculate on a solution to this problem at this time.

However, with further development, it is hoped that this model will provide a rationale for the quantization of angular momentum and the integral number of electron de Broglie waves in the Bohr orbits. This may require, however, an extension of the linear de Broglie model to a spherical model. That is to say, for this model to be fully useful, it must at some point relate to the Schrodinger equation and the Dirac equation.

As to the fine structure constant, we make no claims about the applicability of this model to any other aspect of the inverse fine structure constant beyond that which is described here. For example, the relationship between the vortex electron's radius and the classical electron radius as described by Eq. 10 is not explained here.

In making any of sthe above claims, we do not claim that the validity of this model is a rigorously proven fact. It does, however, provide a probable cause of the first Bohr orbit's stability.

We make no claims about the application of this methodology to the other Bohr orbits at this time.

Appendix A. Some brief comments on the standard particle model as compared with the model we present here

It might well be asked what, if any, relationship there is to the standard model and what we have presented here.

Here, it is clear that we have dealt primarily with atomic physics only, i.e., that we dealt with the structure of atoms, not particle physics as such. The maximum kinetic energy of the electron in the Bohr atom that we use here is that of the electron in its ground state energy as it revolves around the nucleus in a stead state. This energy is only is 13.6 eV. That is to say, there are no high

energy collisions of any kind that produce interaction products that we will be dealing with here.

From the standpoint of the standard model, the electron is one of 12 leptons, or spin ½ particles[31]. We primarily deal here with the electron and its steady state interaction as it orbits the proton in the Bohr atom. However, we make a very brief mention of the muon, another lepton, in Appendix E.

Moreover, there is an essential difference in the model of the electron that we describe here and that of the standard model. The standard model considers the electron to be a fundamental point particle along with quarks and the other leptons, and it is not composed of any constituent parts [32]. That is, the standard model electron is not considered to have a structure, although it is accepted that it has an inherent magnetic moment equal to the Bohr magneton. Specifically, this is based on the Dirac equation. While the Dirac equation is indeed remarkable, it's electron carries this inherent magnetic moment with no phenomenological explanation as to its fundamental origin [33].

At the same time, however, high precision measurements of the magnetic moment of the electron indicate that it is in error with the Bohr magneton, the error being referred to as an anomaly having the value a = 0.00011596521884(43) [32]. The calculated value of this anomaly via quantum electrodynamics is accurate to 10 decimal places [34].

That is to say, the standard model does not provide a cause for its magnetic moment, but it calculates its anomaly, of approximately one part per thousand, with an accuracy of 10 decimal places.

But here, we show *why* the electron has a magnetic moment. I.e., we utilize a previously developed vortex model of the electron whose revolving charge generates the magnetic moment as well as the mass-energy of the electron. This revolving charge vortex model also generates the outwardly spiraling waves that interact with other electrons and give rise to de Broglie waves. It, in effect, has a structure, which the standard model electron does not.

Moreover, we do not concern ourselves with the magnetic moment anomaly, as it is rather small, of the order of one part per thousand, and that has no effect on our model. Further, we do not deal with magnetic interactions here. We just use the magnetic moment to demonstrate the validity of the methodology.

Finally, a major difference in the two models is simplicity. This model produces an accurate, intuitively obvious picture of the electron and why it produces a magnetic moment. Further, it produces a picture of how de Broglie waves are formed from the Compton wavelets the electron generates.

But even an elementary treatment of the Dirac model is long and complicated [34, 35], and when it is finished, there is no explanations as to what the basic mechanism is that produced the magnetic moment. All it provides is the algebraic expression for the Bohr magneton as obtained from the Dirac equation.

Appendix B. A three dimensional field wavelet field around the electron

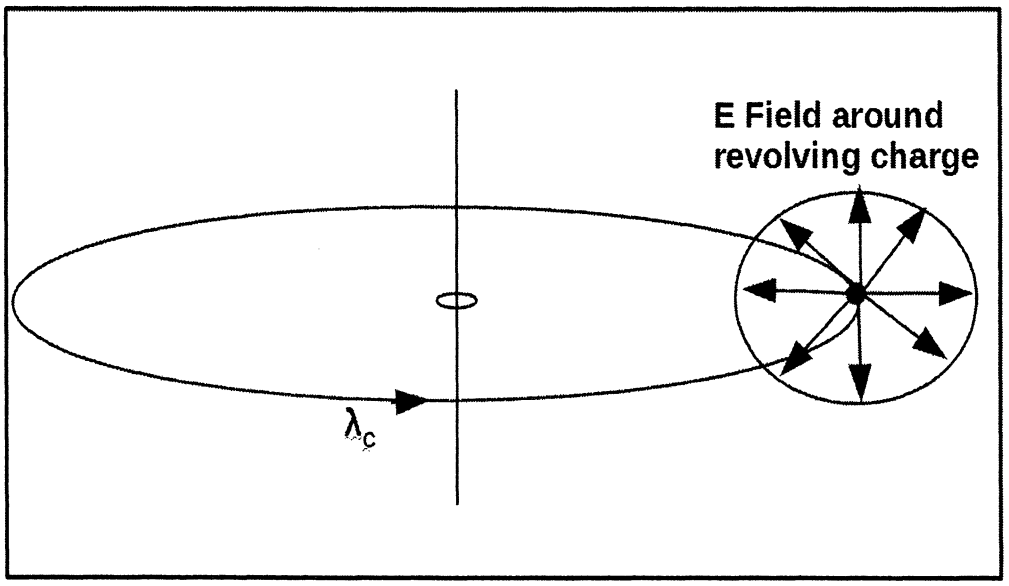

Figure B-1. Here, the Compton wavelet here is being released in a circular plane (i.e., 2D circular pattern) around the charge, the circular plane being parallel to the radius of the electron and perpendicular to the plane of the orbit. This would result in a spherical Compton wavelet, as seen from a distance, that expands outward around the center of the electron as well as radially outward. As seen from above, it would spiral upwards along the axis of rotation while spiraling outward along the plane of the rotating charge in the manner describe in the text above.

While the scenario that gave the most accurate result utilized an impulse that was emitted cyclotron fashion, we also considered the possibility that an observer standing near the orbit would experience an impulse every time the charge passed. That would provide that the impulse would be emitted 360

degrees around the charge in a plane so that, in effect, the wavelets would not just spiral outward in a plane, but in 3 dimensions around the electron. This is shown in Figure B-1, above.

If the impulses are emitted perpendicular to the orbit, we would expect the far field around the electron to be spherical. Otherwise, its acceleration in an electric field would be dependent on its orientation with respect to a magnetic field. For example, if the electrons spin orientation had an effect, it would show up in electron beam apparatus that utilized magnetic focusing, and this has not been observed.

Hence, even though the cyclotron mode of wavelet emission seemed to give the best results, it does not exclude the above 2D mode. In fact, we must consider the possible that both modes are possible.

Clearly, more study is needed here.

Appendix C. Possible interactions of the Compton wavelets with finite structures

Because the vortex electron interacts with other electrons by means of Compton wavelets, we wish to briefly touch on how it might interact with finite structures such as crystals and slits in solid structures [5, 6, 7].

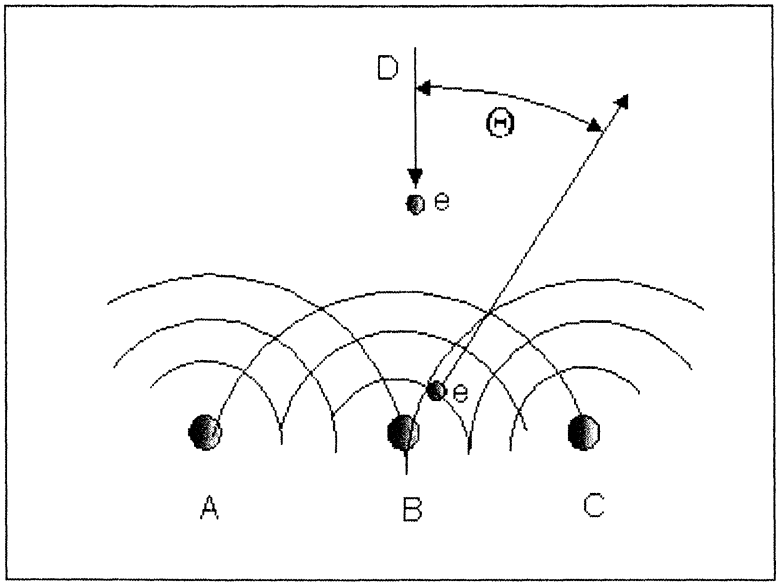

Figure C-1. The case of the Davison-Germer experiment where a diffraction pattern was observed, validating de Broglie's particle-wave hypothesis. Here, an electron is approaching a crystal surface relatively slowly. The Compton wavelets reflect off the atoms in a relatively coherent manner, forming diffraction pattern that interacts with the electron. In the direction of the arrow, the combined wavelets are combined, making them more intense so that an impact with the electron will tend to deflect it that direction. At the angles between them, the relative phases of the wavelets are changing so that it will reduce the probability of scattering at those angles.

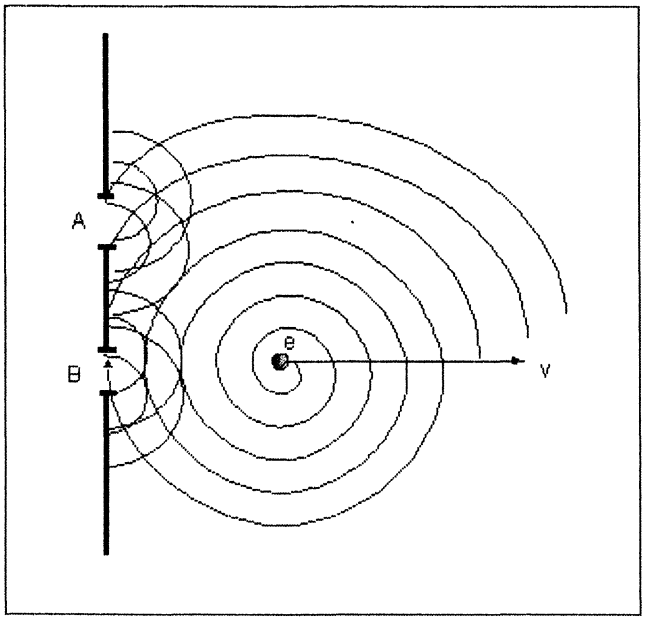

Figure C-2. An electron going through a, ideal slit. The wavelets emitted by the electron after it transits one of the holes reflect off the corners of the slits, forming a diffraction pattern that interact with the slowly moving electron.

In both Figures C-1 and C-2, we picture ideal cases for illustrative purposes.

In C-1, the atoms would be spherical objects much larger than the spacing of the Compton wavelets, but the mean reflected de Broglie pattern, while weak, scattered, and non exact, should provide a crude and diffuse angular diffraction pattern as was observed by Davison and Germer.

In C-2, the distances between slits would be far greater that the Compton wavelets. However, an electron passing through a tiny single slit would, in theory, interact with the wavelets reflected from the edges of the slits and be more likely to produce a pattern that could be explained by this model.

We make no claims that these are proven concepts insofar as the Compton wavelets are concerned. They are presented as unproven models that would best investigated by means of computer simulations. These simulations would likely be extensive and would be required to take into account the distance between atoms, the finite size of the atoms in the crystal, the uniformity of the electron cloud around the atoms, as well as their thermal vibrations.

Appendix D. A sine-cosine Compton wavelet model

The model below provides a picture of two possible regular wave shapes, one sinusoidal and one cosine wave generated by a revolving light speed charge. These were used in some of our original studies of the Bohr orbit [12]. However, in the above study, we chose to ignore these detailed shapes of the wavelets and to concentrate on the lengths of the wavelets as emitted at the 4 cardinal points for better clarity. But having noted that we do not specifically use this in the above work, we include it here to illustrate the mapping of a wavelet onto the x axis when that wavelet is emitted by a particle in a circular orbit whose orbital velocity is the same as that of the wave that propagates along some axis away from the center of the orbit. That is to say, not only are the geometric shapes are interesting. they might be useful in future studies of Compton wavelet phenomena.

In Figure D-1, as the electron rotates, we consider specific portions of its electric field that propagate along the left axis. A is the zero degree reference point on the electron's circumference, B is the 90 degree point, C is the 180 degree point, and D is the 270 degree point.

The points indicated by letters on the x axis correspond to the points of the wave released from the same letters on the orbital circumference at the instant of a full 360 degree rotation.

In order to calculate the wave shapes resulting from Figure D-1, we define a variable, xEmissionPoint, as the projection of a point on the orbit onto the x axis as when the charge is at some angle, theta. I.e., we have

```
xEmissionPoint =
   radius*( 1 + cos( theta*M_PI / 180 ) ) Comptons.          (D-1)
```

Because the wavelets are propagating to left at the speed of light as they are being emitted, the emitted wavelet points on the X axis includes the revolving emission point's x axis position and the linear leftward propagation distance from that point as a function of charge angle, theta for a 540 degree rotation. I.e., the scenario starts when the charge is at point A, or 0 degrees. The scenario proceeds with the charge returning to point A and then to point C, where the scenario ends.

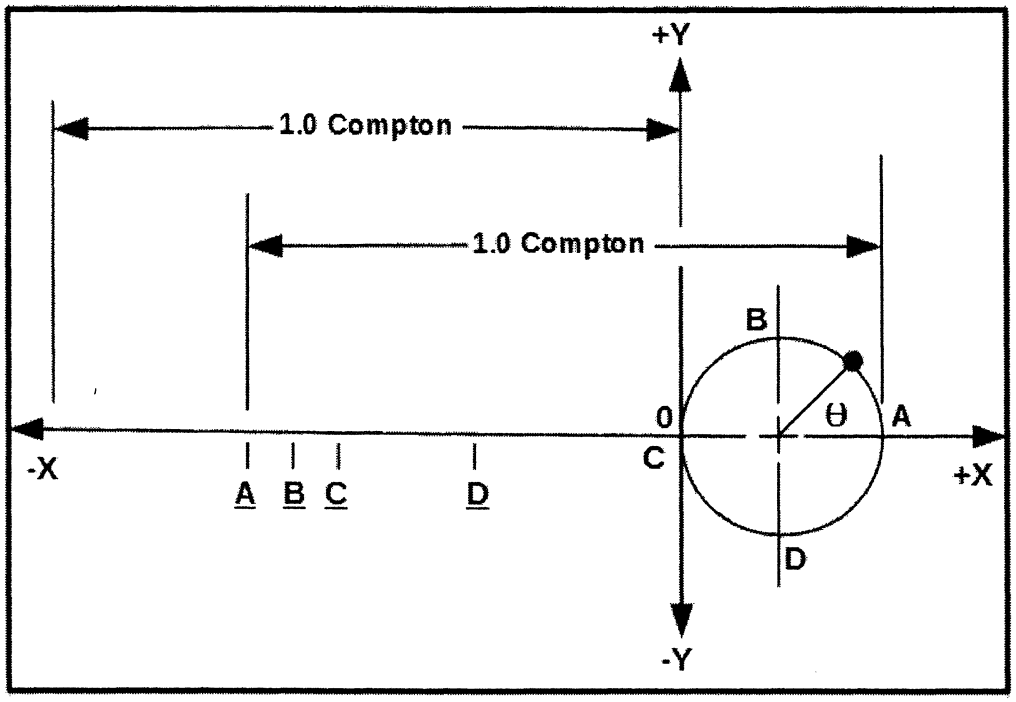

Figure D-1. This shows an electron's counter clockwise rotating light speed charge and points on the axis corresponding to points on the electron circumference. Note that the coordinate origin is at left edge of electron. The nucleus is to the far left.

plotPt = xEmissionPoint - ((540 - theta) / 360) Comptons. (D-2)

plotPt is a variable that provides the x positions of the emitted wavelets at a given angle theta. The intensity is provided for both the sine and cosine of each wavelet at the time it was emitted. The sine, cosine, and x plot points were calculated as a function of the angle theta using a C++ program, and the data was captured in a CSV file for ease of plotting using Excel.

As can be seen, the wave shapes are extremely distorted because of the variation in speed along the x axis by the charge as it emits sinusoidal and cosine wavelets and they are then mapped onto the x axis.

The cosine wavelet, which is based on the position and essentially the velocity along the x axis, has a sudden change in sign at point B. However, the

direction of the charge is not changing drastically at that point. What is changing and that is relevant to the cyclotron modeo is the angle of emission directly towards the nucleus for the cyclotron mode of emission as in the B-A scenario.

Also, the sharp peak in the sinusoidal intensity is not to be ignored as another possible emission mode.

This obviously describes the intensities of emission at point B and does not describe a possible emission from points A or C.

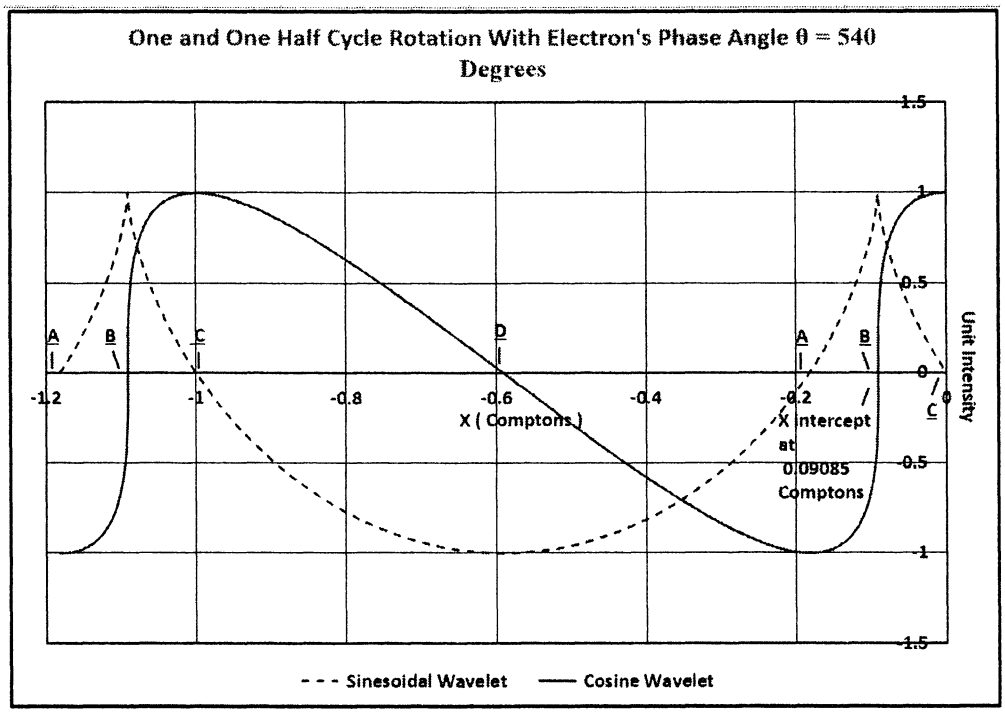

Figure D-2. These are the field intensities of two possible wavelet scenarios, one in which the Intensity is proportional to the sine of theta, and one that is proportional to the cosine of theta. The letters along the x axis are the cardinal points on the charge orbit corresponding to that particular plot point. Obviously, the mapping of the linear points along the circumference of the charge's orbit onto the x axis is highly distorted. The distance between the two points B are one Compton.

Appendix E. Energy Density and the classical electron dimension as a possible stability boundary for particles

Here, we wish to make a few comments on the possibility that the classical electron radius might be a dimensional marker for the size of the container of the electron's mass energy.

In the original negative mass tachyon derivation of Eqs. 1 – 4, it was found that the equations used here also held for the muon, but with the muon having a much small orbital radius. The electron's radius in this model used here is 386.15933 fm and the muon's radius is 1.8675947 fm. Here we use CGS units rather than Electron Units because of the small sizes. The classical electron radius is 2.8179403267 fm, slightly larger than that of the muon.

But to take it a step further, it was found that the equation, $M = 4076/n^2$, provides a set of energy levels whose first order transitions provide the Psi meson masses to within 4.7 % [3, 28, 30, 31]. . Also, the second order transitions provide the masses of the eta through a_0 to within 2.3% except for the $\Omega(783)$, which is in error by 9.5 %.

But in order to achieve these accuracies, the pion's charge, even though it is generally considered to be a spin 0 particle, was required to revolve in a very tiny orbit with a corresponding tiny magnetic field. This pion orbit had a radius 0.18503077 fm in order to produce those meson energies. I.e., its orbital radius is approximately 1/10 that the muon.

The pion and muon are both unstable and have much higher energy densities than the electron. The pion generally decays into a muon, and the muon then decays into an electron, with neutrinos being emitted in both cases. In all of these, it is the same charge, but it revolves in different sized orbits. That is to say, particles with small orbits have high energy densities and are unstable, and the relatively large electron represents the stable state with its mass-energy spread over its much larger orbit.

Hence, it is unlikely that an entity with the electron's mass-energy packed into a volume having a radius slightly greater than that of the muon would be stable. I.e., while the classical electron radius is extremely interesting, we claim here that it does not actually contain the energy of the electron.

But having said this, we speculate that because the muon's radius is smaller than the classical electron radius, it and smaller particles are unstable. That is to say, we further speculate that the classical radius is a dividing line between

stability and instability. Beyond that, its meaning is unclear at this time, especially since it is related to the electron's radius by the fine structure constant.

What we cannot say is why the classical electron radius is related to the actual electron radius by the fine structure constant, and in turn, the radius of the electron is related to the first Bohr radius by the fine structure constant.

Finally, in view of the above, the muons and pions are much smaller than electrons. Hence, we argue that a Compton wavelet treatment, as opposed to a de Broglie wavelength methodology, offers much in the cases of smaller particles and even nuclei. That is because these smaller particles, just as in the case of the electron, produce wavelets that would be smaller than their de Broglie waves.

Appendix F. The Bohr atom's electron ideal capture trajectory and a comparison of Electron Units and CGS units

In order to further illustrate the human readable advantage of the Electron Units over CGS units for the detailed calculations of electron dynamics in the Bohr atom, we consider here the case of an electron being attracted from an infinite distance to a proton held fixed at some point. Further, for illustrative purposes we assume the electron does not radiate, so it can therefore go directly toward the nucleus in a straight line like a body falling towards a planet in its gravitational field.

The acceleration at a given radius is

$$a = \frac{F}{m_e} = \frac{Q^2}{m_e}\frac{1}{r^2} = \frac{dv}{dt}\ , \tag{F-1}$$

The energy of an electron approaching a hydrogen nucleus is given by

$$E = \frac{mv^2}{2} = \frac{q^2}{r}\ . \tag{F-2}$$

From this, we can calculate the radial velocity as

$$v = q\sqrt{\frac{2}{mr}} = q\sqrt{\frac{2}{m}}\sqrt{\frac{1}{r}} \tag{F-3}$$

It is then convenient to calculate the position by numerically integrating the velocity over t, which is sufficiently accurate for our purposes here, which is to illustrate the usage of the Electron Units.

The point to be made is that, first, the Electron Units are more human friendly at these dimensions than are the CGS units. Second, when we are trying to synchronize the rotating electron with wavelets reflected from a nucleus, they are even more meaningful than CGS units.

In the following, we show the output of a Java program written to simulate the above equations. We started our calculations at an arbitrary distance from the nucleus of $25r_0$, where r_0 is the first Bohr radius and it equals 545.2 Comptons. At this point, the velocity that had been reached as the particle had accelerated from an infinite distance to that point is 0.2064 Comptons/rotation. Also, and the acceleration, which is dependent only on the distance from the nucleus, is 3.91E-5 Comptons/rotation^2.

It should be noted that the distanced used here is much smaller than the 37557.72787644 Compton length of the shortest Lyman photon.

Also, in the time required to travel this distance to r_0, the electron will undergo some 175 thousand rotations. This is rather large in comparison to the 37.5 thousand rotations required for a single cycle of the Lyman photon as given in Eq. 61, above, so there is plenty of time here to generate the photon. However, Eq. 62 says that half of the photon period is the same period as the Bohr orbit period as given by Eq. 29. This implies that the electron spirals downward towards the nucleus until it reaches the first Bohr radius, at which point it stops moving inward. By that time, it has completed the generation of the photon. However, it is not clear if it needs to generate the entire photon, of just the first half cycle which will, then, collapse and generate the other half cycle, beginning the photon's life. Nor, is it clear when it starts to generate the photon. I.e., is there a critical acceleration it needs to reach in order to begin to generate the photon.

Note that at the end of this appendix we provide some conversion factors for converting between CGS and EUs and vice versa.

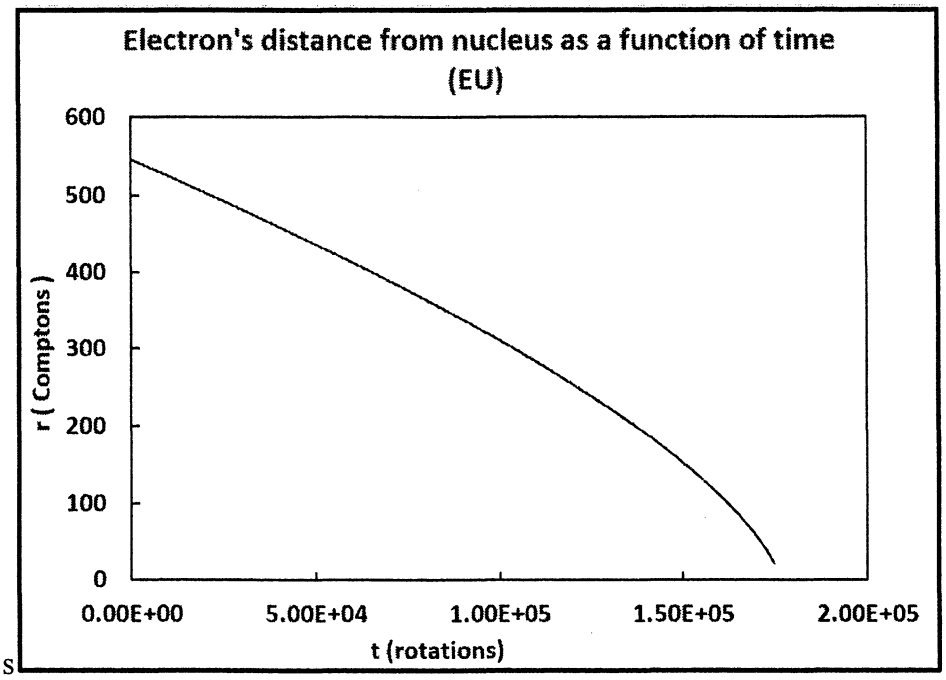

S

Figure F-1. Here, we show the accelerating electrons distance from the nucleus as a function of time in rotations. The distance is relatively large and friendly compared to what they would be in CGS units. The times are larger, but finite relatively small and human friendly as compared with that of CGS units. They also provide for easy synchronization of the phases of the electron and wavelets.

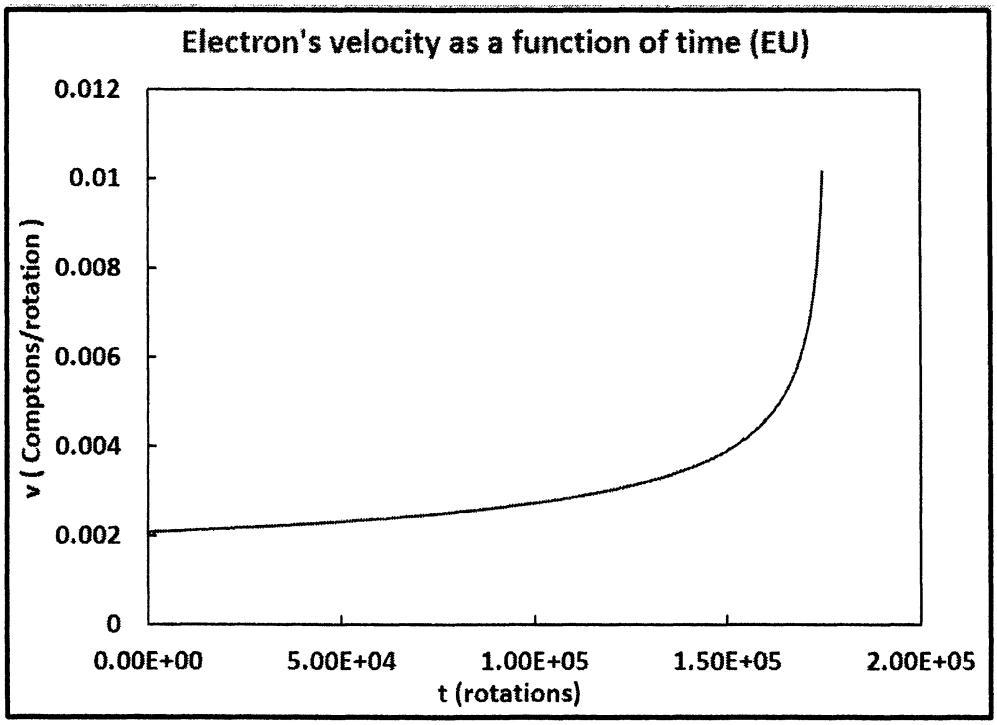

Figure F-2. The velocity of the accelerating electron as a function of time expressed in Comptons/rotation. The time values, as in Figure a-1, are finite but relatively small and human friendly. The velocity is also relatively finite and human friendly.

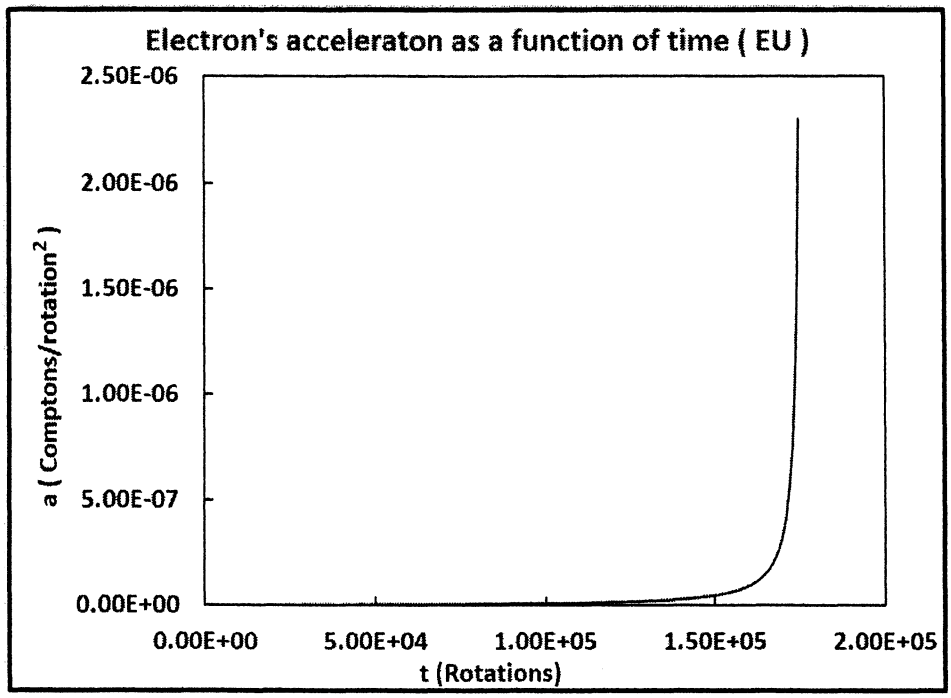

Figure F-3. The acceleration in Comptons/rotation^2 as a function of time expressed in rotations. However, because the acceleration is an inverse square law, much of the early data is too small to plot when expressed in linear units. However, the times, as in in the previous figures, are larger than the CGS units and more human friendly, however.

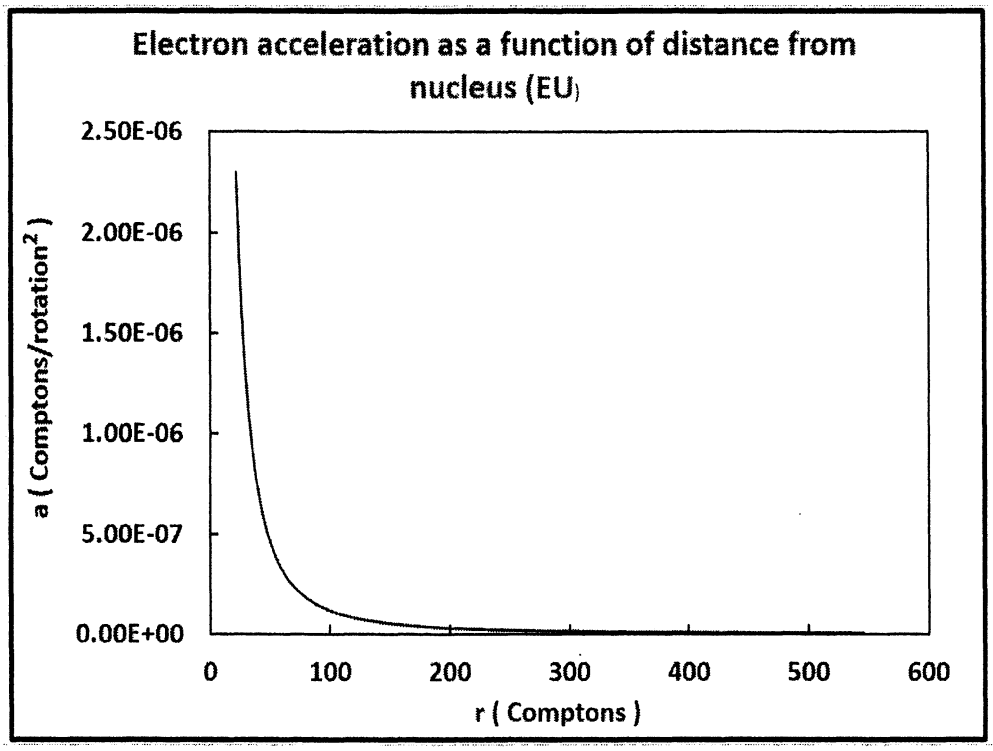

Figure F-4. Acceleration as a function of radial distance from the nucleus in Electron Units. Again, they are human readable insofar as numbers are concerned in comparison with CGS units.

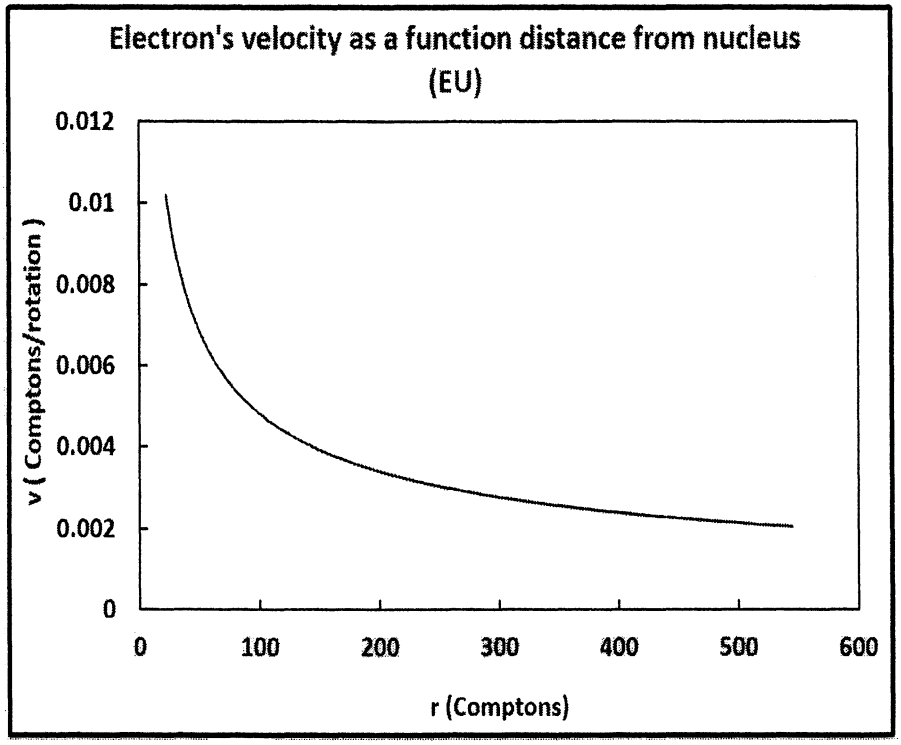

Figure F-5. Velocity as function of radial distance from the nucleus expressed in human readable units.

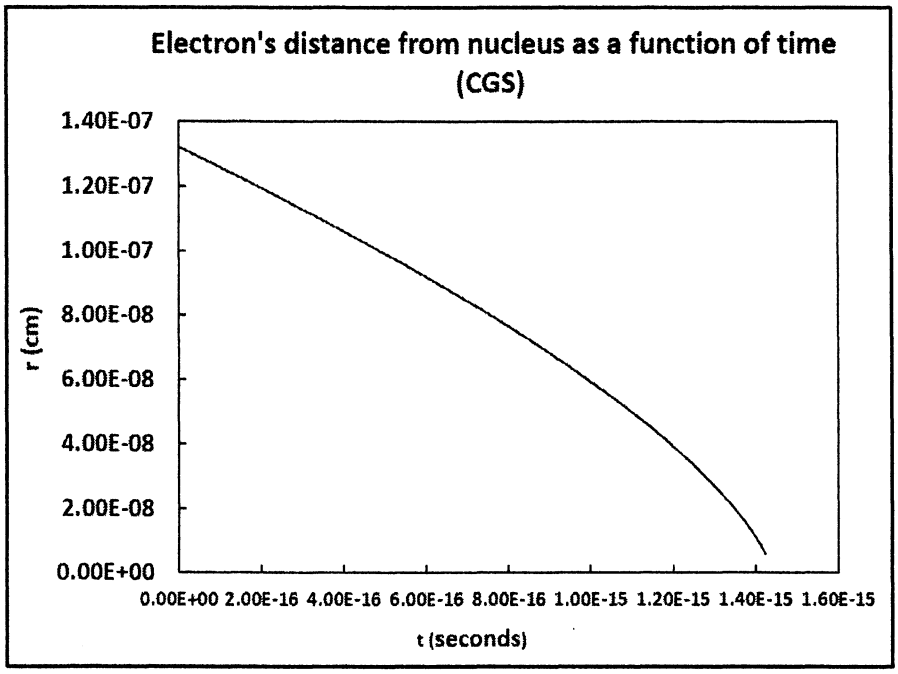

Figure F-6. This is the same data as that in Figure A-1, but in CGS units. While the numbers are accurate and useful in computer calculations, they do not provide a human readable value, nor do they provide for easy synchronization of the wavelet and electron phases.

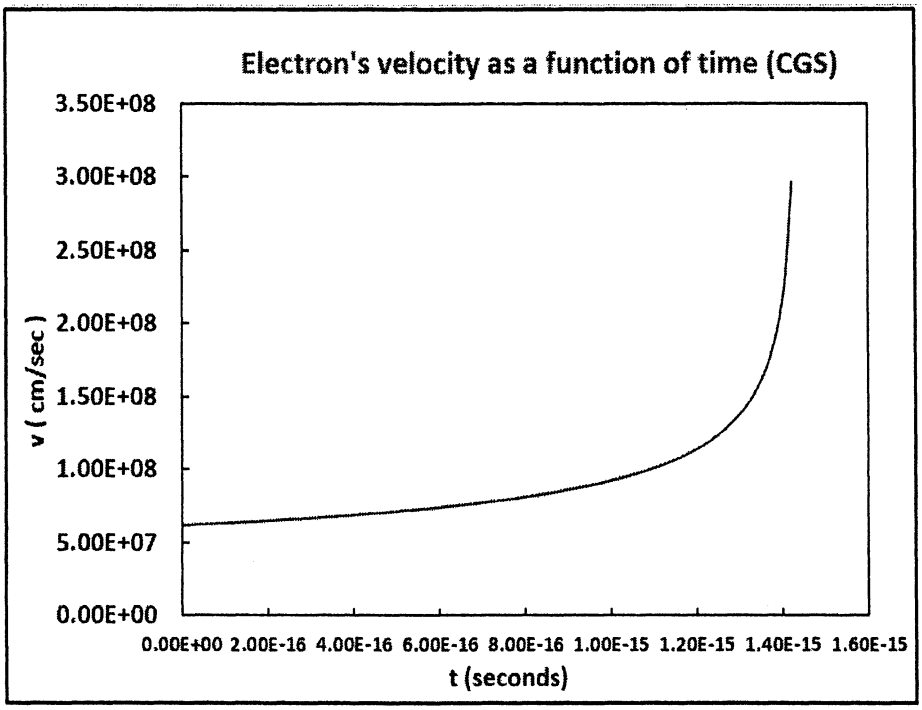

Figure F-7. Velocity as a function of time in CGS units. While it is useful for computation with a computer, a hand calculator, or even an old slide rule, the time is totally abstract to the human mind.

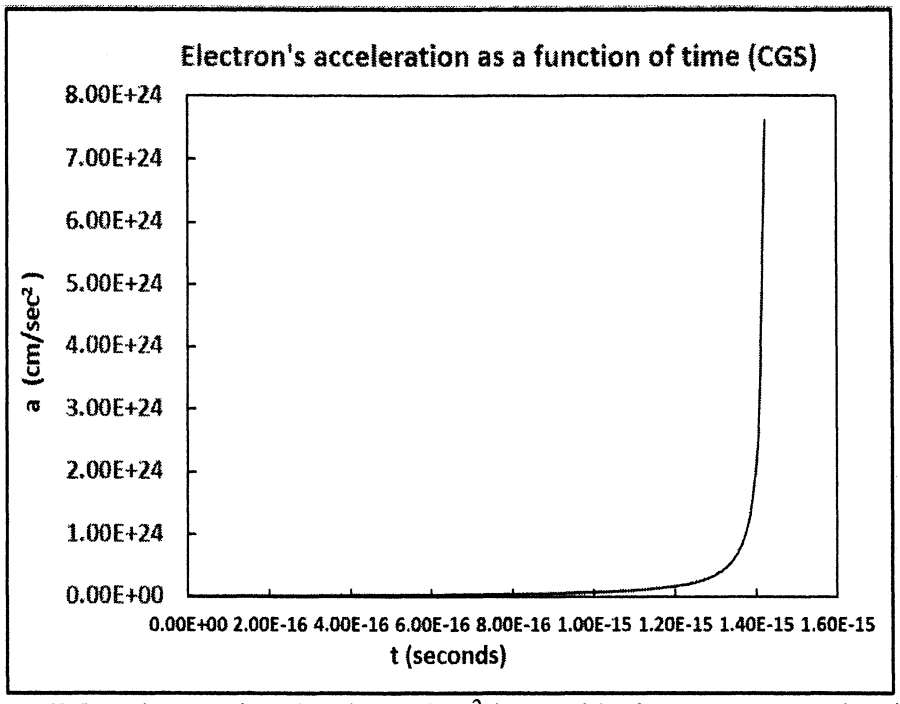

Figure F-8. The acceleration in cm/sec^2 is useable for a computer, but it is so large as to be incomprehensible in a human sense. Clearly the Electron Units proposed here are much more human readable and human comprehendible.

Table F-1. Conversion factors for Electron Units to CGS units

Parameters	EU to CGS factor	CGS units
Length	2.4263102389 E-10	cms
Time	8.09329979E-21	secs
Mass	9.10938291E−28	gms
Velocity	2.99792458E+10	cms/sec
Acceleration	3.70420553E+30	cms/sec^2
Force	3.3743026550E+03	dynes
Work	8.1871050810E-07	ergs

Table F-2. Conversion factors for CGS units to Electron Units.

Parameters	CGS to EU factor	EU units
Length	4.1214844828E+09	Comptons
Time	1.2355899645E+20	rotations
Mass	1.0977692011E+27	electron masses
Velocity	3.3356409520E-11	Comptons/Rotation
Acceleration	2.6996342182E-31	Comptons/Rotation^2
Force	2.9635752991E-04	electrodynes
Work	2.9635752991E-04	electroergs

References

1. Ernst L. Wall. "The Role of Tachyons in Electron Spin and Muon Spin", Bulletin of the American Physical Society **30**, p. 729 (1985)

2. Ernst L. Wall. "Indirect Evidence for the Existence of Tachyons; A Unified Approach to the $\pi \rightarrow \mu \rightarrow e$ Conversion Problem", Hadronic Journal **8**, p. 311 (1985).

3. Ernst L. Wall. **The Physics of Tachyons**, 234 pp., Hadronic Press, (1995).

4. Ernst L. Wall. "Unresolved Problems of the Tachyonic Models of the Electron and the Muon", Hadronic Journal **9**, p. 263 (1987).

5. Ernst L. Wall. "Origin of de Broglie Waves in a Tachyonic Electron Model", Bulletin of the American Physical Society **44**, p. 35 (1999).

6. Ernst L. Wall. "Electrodynamics of Revolving Light Speed Particles and A Fundamental Basis for de Broglie Waves", Hadronic Journal Supplement **14**, p. 79 (1999).

7. Ernst L. Wall. "The Fundamental Electrodynamic Origin of Electron de Broglie Waves", Hadronic Journal Supplement **15**, p. 123 (2000).

8. M. Uchida & A. Tonomura. "Generation of electron beams carrying orbital angular momentum", Nature **464**, pp. 737 – 9, (2010).

9. J. Verbeeck & P. Schattschneider. "Production and application of electron vortex beams.", Nature **467**, pp.301-4 (2010)

10. P. Schattschneider and J. Verbeeck. "Theory of free electron vortices", Ultramicroscopy **111**, pp. 1461-1468 (2011)

11. Ernst L. Wall. "Revisiting the Bohr Atom 100 Years Later", Bulletin of the American Physical Society, **58**, D1.00007 (2013).

12. Ernst L. Wall. "The Origin of the fine structure constant", Bulletin of the American Physical Society, **59**, E2.00005 (2014).

13. Ernst L. Wall. "The Vortex Electron and the Origin of the Bohr Radius and its Fine Structure Constant, and Pilot Waves", Bulletin of the American Physical Society **60**, New B5.00026 (2015)

14. Ernst L. Wall. "Maintaining the First Bohr Orbit Radius by Photon Suppression", Bulletin on the American Physical Society, 2015 Fall New England Section, **NEF15-2015-000044**.

15. Robert M. Eisberg. **Fundamentals of Modern Physics**, pp 139 - 146, (John Wiley & Sons, 1961)

16. David Bohm. **Quantum Theory**, pp. 59 – 80, (Prentice-Hall, Inc., 1951)

17. J. Beringer, et al. (Particle Data Group), Phys. Rev. **D 86, 010001**, p. 444 (2012).

18. J. Beringer, et al. op. cit., p. 107 (2012).

19. O. M. P. Bilaniuk. V. K. Deshpande, and G. Sudarshan, "Meta" Relativity, Amer. J. of Physics **30**, 1962, pp. 718-23.

20. E. Recami and R. Mignani. Rivista Nuovo Cimento **4**, 209 (1974)

21. Robert M. Eisberg, op. cit., pp. 110 – 124, (John Wiley & Sons, 1961)

22. E. U. Condon. **Handbook of Physics,** pp. 7-24 – 7-26 (McGraw-Hill, 1967).

23. Ernst L. Wall. "Origins of the Electron's Angular Momentum", Bulletin of the American Physical Society **58**, D1.00007 (2013)

24. Keith R. Symon. **Mechanics**, pp 223, 224 (Addison-Wesley, 1960)

25. Gerhard Herzberg. **Atomic Spectra and Atomic Structure**, p. 93, (Dover Publications, 1944)

26. Otto Klemperer. **Electron Physics: The Physics of the Free Electron**, p. 206,
(Butterworth Group, 1972)

27. Leonard Schiff. **Quantum Mechanics**, p. 146 (McGraw Hill, 1955)

28. Ernst L. Wall. "On Tachyons and Hadrons", Hadronic Journal **9**, p. 239 (1986)

29. Albert Messiah. **Quantum Mechanics Vol. II**, p. 951 (1961)

30. Ernst L. Wall. "Charm, Other Resonances, and the Tachyonic Particle Model", Bulletin of the American Physical Society **33**, p. 1076 (1988).

31. Ernst L. Wall. "On Pion Resonances and Mesons, Time Cancellation, and Neutral Particles", Hadronic Journal **12**, p. 309 (1989).

32. Mark Thompson. **Modern Particle Physics**, p. 1 – 4, (Cambridge University Press, 2013).

33. W. N. Cottingham, and D. A. Greenwood. **An Introduction to the Standard Model of Particle Physics**, p. 87, (Cambridge University Press, 2007)

34. W. N. Cottingham, and D. A. Greenwood. **op. cit. p 89.**

35. Christopher G. Tully. **Elementary Particle Physics in a Nutshell**, pp. 9 – 63, (Princeton University Press, 2011)

36. Mark Thompson, op. cit. pp. 80 - 110.